THE UNIVERSITY OF MANITOBA

CHARACTERIZATION AND MEASUREMENT OF THE SPATIAL
DISTRIBUTION
OF ELECTROMAGNETIC FIELDS PRODUCED BY FOCUSSING
ELEMENTS.

by

© CHRISTOPHER HADDOCK

A THESIS
SUBMITTED TO THE FACULTY OF GRADUATE STUDIES AND
RESEARCH IN PARTIAL FULFILMENT OF THE REQUIREMENTS
FOR THE DEGREE OF DOCTOR OF PHILOSOPHY

IN

PHYSICS

DEPARTMENT OF PHYSICS

WINNIPEG, MANITOBA

FALL, 1988

Canadä

CHARACTERIZATION AND MEASURMENT OF THE SPATIAL DISTRIBUTION

OF ELECTROMAGNETIC FIELDS PRODUCED BY FOCUSSING ELEMENTS

BY

CHRISTOPHER HADDOCK

A thesis submitted to the Faculty of Graduate Studies of
the University of Manitoba in partial fulfillment of the requirements
of the degree of

DOCTOR OF PHILOSOPHY

©   **1989**

THE UNIVERSITY OF MANITOBA

RELEASE FORM

NAME OF AUTHOR: Christopher Haddock

TITLE OF THESIS: Characterization and Measurement of the Spatial

Distribution of Electromagnetic Fields produced by

Focussing Elements.

DEGREE: DOCTOR OF PHILOSOPHY

YEAR THIS DEGREE GRANTED: 1988

Permission is hereby granted to THE UNIVERSITY OF MANITOBA LIBRARY to reproduce single copies of this thesis and to lend or sell such copies for private, scholarly or scientific research purposes only.

The author reserves other publication rights, and neither the thesis nor extensive abstracts from it may be printed or otherwise reproduced without the author's written permission.

(Signed) ....

PERMANENT ADDRESS:

TRIUMF

4004 Wesbrook Mall

Vancouver, B.C.

CANADA, V6T 2A3

DATED: 26ᵗʰ Nov 1988 ....

©

Dedication

To my mother, Mrs. J. A. Miles and to the memory of my father, Mr. F. A. V. Miles, for their constant support throughout my studies.

Abstract

During the late 1970's in the wake of fossil fuel price increases, renewed interest in the generation of renewable forms of energy was aroused. In order to study new methods of converting solar energy in particular to more useful forms, a solar concentrator facility was built on the roof of the Physics building at the University of Manitoba. The first of its kind in Canada, and the only one outside the so-called "sunbelt" states, the purpose of the facility is to concentrate the intensity of beams of sunlight by a factor of several thousand using a system of reflecting and focussing mirrors and to use this technique in the direct generation of electricity.

The facility was constructed with financial and material aid from the University and from Manitoba Hydro. After construction was complete the intensity variation of the concentrated sunlight at the focus of the system was measured with a radiometric instrument capable of measuring very high intensities. The results of the mapping were compared with a theoretical model which used the optical figuring parameters of the system as input. The results showed that the concentrated intensity as a function of position can be accurately predicted given the incident intensity and a representative value of the clearness of the sky for that day. The comparison between predicted and measured focal plane intensities has not been not performed before, it will be extremely useful in determining the focal plane intensity profile during an experiment and hence the performance of converters placed there.

An experiment was proposed to study the conversion of solar energy to electricity directly using a solar sustained cesium plasma. The aim of the experiment was to determine the efficiency with which electrical energy could be extracted from a plasma, sustained by concentrated sunlight, as it passed through a magnetohydrodynamic channel. Un-

fortunately interest in solar energy conversion was beginning to wane as at this time the price of oil began to fall. The reviewing process was halted when the department for solar energy programs of NRC was closed. Alternative funding for the experiment could not be obtained at that time.

Almost at the same time an applied Physics "Technology Transfer" grant was awarded to the Department of Physics to transfer the technology of magnet construction and mapping magnetic fields to a local Winnipeg company. The basic physical principles used for measuring magnetic fields have changed little since the 1970's. However advances have been made in the areas of instrumentation and logging of analogue data. The challenge of designing and assessing a compact state of the art system became part II of this Ph.D thesis.

At the start of the technology transfer process it was decided that a modern analogue to digital converter (ADC), an integral part of a high accuracy digital multimeter, could perform data collection quickly and accurately so that recording of pulse information could take place in real time. Thus electronic integrators, which can be inherently unstable and represent the weak link in this type of apparatus are no longer required in the measurement process. Furthermore, advances in microcomputer technology, both hardware and software, made it possible to produce a completely automated field mapping system, including data analysis and logging, for approximately 1/5th the price of other competitive contemporary systems. At the same time this strategy eliminated the long lead time required for developing an appropriate software package. The system designed and built in the Department of Physics has since been delivered to K & S Tool and Die Ltd. where it has been used to characterize magnets built by the company. The system is described in part II of this thesis.

Acknowledgements

There have been few people in the department of Physics, university of Manitoba who have not helped me in one way or another during the course of this work. I would like to acknowledge all them all personally, at the risk of forgetting to mention someone's contribution.

With regard to the solar energy work I must thank Javid Ashraff, Craig Benson, John Martens and Margaret Mesa, who, as Summer students helped me build the solar concentrator facility starting from a bare roof top. I must particularly thank John Martens for helping me perform the initial focal plane intensity mappings in -20° C weather and Craig Benson for his assistance in measuring the concentrating mirror distortions in +40° C weather.

The solar energy and magnetic field mapping equipment could not have been built without the assistance of the mechanical and electronics shops of the department of Physics. I would like to thank all the staff, particularly John Lancaster of the mechanical shop and Richard Hamel of the electronics shop for their contribution.

Financial assistance from Mobil Oil corporation during the solar energy part of the work is gratefully acknowledged.

For their assistance in matters relating to computers I would like to acknowledge Gary Dyck, Werner Ens and Cliff Lander for their advice and help.

I am indebted to Dr. Gary Smith for overall supervision of the magnet measurement part of the thesis, his help and patience in the analysis of the data from the measurement probes is appreciated.

Finally I would like to thank my supervisor Dr. J.S.C. McKee for giving me the opportunity to work on these projects and for his guidance through the course of them.

Contents

Chapter 1

Introduction

The efficiency with which solar energy can be converted into more useful forms is one of the most important parameters concerning its utilization as a viable alternate source of energy. In order to study a new and potentially highly efficient methods of converting solar energy directly to electricity a facility was constructed at the University of Manitoba.

The facility was designed to produce highly concentrated beams of sunlight and to deliver this intensity to a solar energy converter placed in the focal plane of the system. The proposed converter would consist of a cesium plasma, sustained by solar energy. Electrical energy would be extracted directly from the plasma as it passed through a magnetohydrodynamic channel.

Solar energy conversion has been investigated in several waves of interest for over a hundred years. In order to place the proposed converter in technological perspective a brief history of solar energy conversion is given in chapter 2.

As the earth revolves around its axis during the course of the day and around the sun during the course of the year the amount of sunlight available on the

surface of the earth will vary due to the relative orientations of the sun and the receiving surface. This amount of sunlight will be reduced by the absorbtion of a fraction of the incident sunlight by the atmosphere. Further, a fraction of the incident sunlight will be scattered by air molecules and suspended particulate matter. The proposed conversion scheme would obtain a higher efficiency by using a higher working temperature medium. In order to achieve high temperatures, the incident light intensity must be concentrated by a factor of several thousand. Only the direct or beam-like component of the incident sunlight can be focussed. It is therefore important to understand how the orientation of the earth and the state of the atmosphere affect the amount of solar energy received at ground level and what fraction of it may be focussed. Chapter 3 describes the nature of solar energy in terms of the effects described above and provides a means of estimating the variation of direct solar intensity throughout the day on clear days using a parameter which represents the clearness of the atmosphere.

To determine the efficiency of a solar energy conversion device the amount of sunlight available at any instant needs to be accurately known. If the conversion device relies on that component of sunlight which can be focussed, then the incident direct intensity needs to be measured separately from the total available. Chapter 4 describes those devices which measure the different components of solar energy reaching the earth.

The proposed converter would require highly concentrated beams of light for its operation. Chapter 5 contains a review of the types of solar collectors describing the advantages and disadvantages of each. It is shown that only two types of solar collector arrangement would be able to provide the amount of concentration of sunlight required, and that of these two the so called solar furnace arrangement was the more suitable for our purposes. The mechanical

and electrical details and the construction of a solar furnace, the only one of its kind in Canada are described in chapter 6.

Once the facility was complete it was necessary to determine by how much the incident sunlight could be concentrated and delivered to the focal plane. In order to do this a radiometric device designed for the purpose of measuring highly concentrated sunlight was used to map out the focal plane intensity contours. The focal plane intensity mapping is described in chapter 7.

As the results of the focal plane mapping were analyzed an anomaly was observed between the expected power obtained at the focus and the measured power. In order to understand this discrepancy, measurements were made to determine the accuracy of figuring of the surfaces of the concentrating system of mirrors. Values of parameters characterizing the system were entered in to a mathematical model. During the course of these measurements the source of the discrepancy was found. Further using the model it was possible to accurately predict the focal plane intensity variation given only two parameters: the incident solar intensity and a representative value of the clearness of the atmosphere. The ability to predict the focal plane intensity distribution based on these two parameters will be extremely useful in evaluating the performance of solar energy converters. The comparison of the predictions of the model with physical data is the first performed. Details of the prediction model, the mirror contour measurements and the conclusions drawn are given in chapter 8.

A summary of the major findings and conclusions from the work on the solar concentrator arrangement is given in chapter 9.

Potential applications of concentrated beams of sunlight mostly consist of established energy conversion techniques that have been adapted for use

with solar energy. These are briefly reviewed in chapter 10. This is followed by a discussion of the proposed converter which is uniquely suitable for use with highly concentrated beams of sunlight.

Chapter 2

A Brief History of Solar Energy Conversion

Solar energy has been investigated as an alternative source of energy in at least two "waves" of popularity. The basic technology of generating steam from solar energy, and then using the steam to drive engines, is so straightforward that several plants were operating successfully over 100 years ago. Some of the early conversion schemes are described below.

In 1874 August Mouchot, a French engineer concentrated sunlight onto a boiler and used the steam produced to operate a small engine. The engine produced steam pressure of 30 psi (2.1×10^5 Pa) in 40 minutes. The boiler vaporized more than 5 quarts (5.5 l) of water per hour, and the engine developed approximately 1/2 hp (0.37 kW). Some engines of this type were used in Algeria for pumping water.

In 1878 in Paris, M. Pifre used a solar engine to run a printing press to print a daily newspaper. In 1883 in the United States John Ericsson demonstrated the first "trough" type solar concentrator. (see Chapter 5) The principle was put to use in 1912 by Shuman and Boys for an irrigation project in the Nile

river basin, the troughs were 220 feet long and generated approximately 60 horsepower (45 kW).

Between the years 1924 to 1934 Robert Goddard, primarily known for rocket work, engaged concurrently in solar power conversion research. He was granted five patents and constructed several laboratory test models of devices which used concentrated sunlight:

> *"to provide a means by which radiant energy may be used to convert a liquid into vapour in a limited space or area, but at which area the rapid flow of liquid prevents an excessively high temperature, notwithstanding the high concentration of solar energy. A further objective is to provide improved means for localizing the heat absorption and for preventing re-radiation thereof."* [1]

Some of Goddard's suggestions were later pursued in current research in solar power conversion. He proposed that the focal plane of a concentrator should contain a liquid with a finely divided solid substance in suspension. In 1982 this idea was being pursued by Hunt et al [2]. In 1929 Goddard described a sun tracking parabolic concentrator made of polished aluminium [3], a type of collector widely adopted since then.

As oil and its derivatives were used more and more as a source of power, solar power became economically less and less attractive. For sixty years (1915-1975) as the price of petroleum effectively fell, the development of solar technologies was suspended.

By 1978, crude oil and its derivatives provided 74% of the prime energy used in the United States (38Q) [1] [4]. Of this, 49% was imported. The relative

---

[1] $1 \text{Quad} = 10^{15} \text{ BTU} = 3 \times 10^{11} \text{ kWhrs} = 1.08 \times 10^{18} \text{ J}$

amount of oil imported had increased from 25% in 1960 to 50% in 1977-80. In early 1973 the price per barrel of oil was US$2.50. During the 1973 oil embargo, OPEC raised the price of oil several fold. By 1980 the price had risen to US$32.00.

This action revealed the dependence of the U.S on imported energy. Consequently there was renewed interest in all forms of alternative energy resources, and a new round of prototype engineering, system modelling and engineering development began. Nuclear power as an alternative was begining to wane in popularity due to huge cost overruns and system failures (figure 2.1) [5], events which preceded the accidents of Three Mile Island and Chernobyl.

In 1977 the U.S Department of Energy was formed to investigate alternative forms of energy. Over a four year period (1978-1982) US$700 million was invested in solar technology [6]. The majority of the funding (US$500 million) was invested in the development of hardware such as: (i) the design and evaluation of heliostats and parabolic trough and dish concentrators as related to mass production, and (ii) the construction of large solar test facilities such as that in Albuquerque, New Mexico, in which a field of 200 sun tracking heliostat mirrors reflect light onto a central receiving tower [7].

Solar powered Rankine and Stirling Cycle engines were also studied during these years, [8], although for many test facilities high temperature steam still formed the working fluid [9] as in the early attempts.

Much work was performed by the industrial sector towards the development of a "low cost concentrator" i.e a sectional parabolic concentrator with a diameter of approximately 10m which could be mass produced. Several of these could then be used
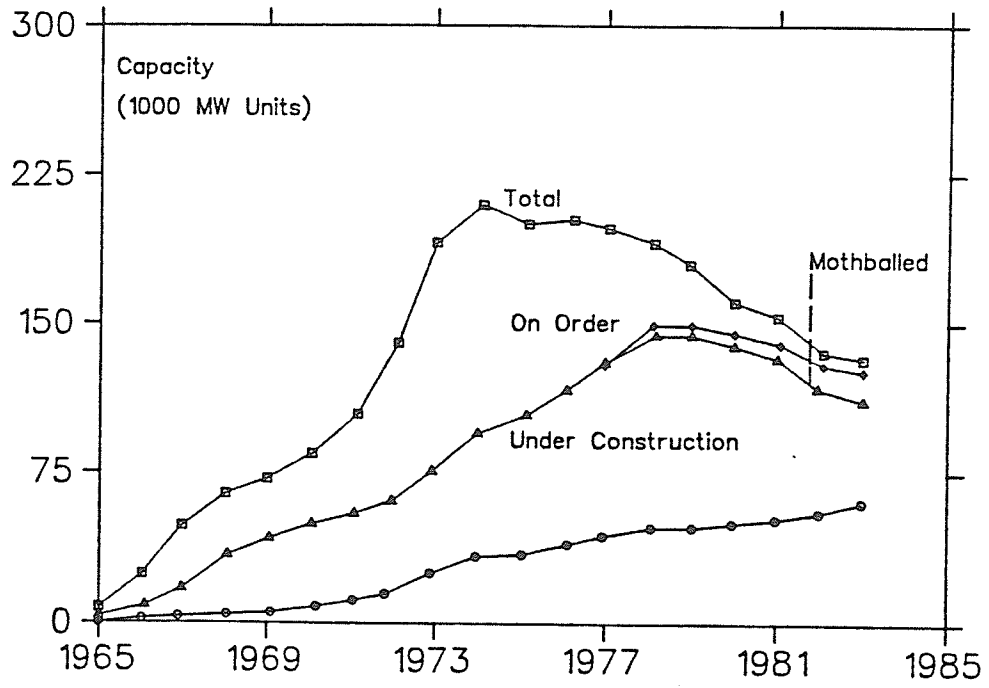
Figure 2.1 United States nuclear power capacity 1965-1985. [5]

together to generate the power required for a particular application, thus forming a distributed collector arrangement for power generation on or close to the site where the power would be required. It was estimated that such a concentrator, with a Stirling engine at the focus would be competitive with oil which cost $40 per barrel [10].

The current interest in solar energy began to wane with the fall in the price of oil and the success of energy conservation programs. The aim of DOE was to establish a solar thermal industry by sponsoring the Solar Thermal Test Facilities Users Association and providing funding for experiments. The industry did not grow and the STTFUA was not funded in FY1983.

An alternative to solar thermal energy conversion is the solar photovoltaic conversion process of solar cells. First manufactured in 1965 these have developed slowly. They were not considered a viable economic alternative to oil at the time of the embargo, due to their high manufacturing cost and relatively low efficiency, approximately 10% compared to 30% for a solar steam plant such as at Barstow, California. Since that time efficiencies have increased and with the development of amorphous solar cells, manufacturing costs have decreased. Currently solar cells are the most actively pursued form of solar energy conversion.

During the most recent wave of interest most of the major funding was applied in the area of solar-thermal technology i.e the application of solar energy to provide the heat input into energy conversion devices. These devices were for the most part already established types of heat engines which were adapted to accept solar thermal energy as the heat input.

The study of new forms of energy conversion devices designed specifically with solar energy in mind received little funding. However during this period

the theoretical basis for a conversion scheme using a solar sustained cesium plasma and a magnetohydrodynamic channel was being developed. In order to investigate the conversion efficiency of this and other new type of energy conversion devices, the solar energy facility at the University of Manitoba was constructed.

Dollar figures in the above are quoted as they were at the time. No attempt has been made to evaluate them in "constant dollars". The Energy Information Association of the U.S applies a "Gross National Product Price Deflator Index" to its quoted figures, however this index is based on all commodities. During 1969-1980 the inflation in fuels was over twice that of other commodities. For want of a better weighting system the prices were left as quoted.

Chapter 3

The Nature of Solar Energy

3.1 Introduction

The investigation of high efficiency solar thermal energy converters implies high temperature receivers and working fluids. This in turn implies that the solar intensity incident on the receiver must be concentrated many times over the value of the intensity reaching the earth. This is accomplished by focussing the light incident on a large collector area onto a smaller receiver area.

Sunlight reaching the outer atmosphere of the earth is essentially monodirectional. Scattering of the sunlight by air molecules and suspended particulate matter in the atmosphere results in a diffuse component reaching the earths surface. Only that part of the incident intensity which is beam like may be focussed. The size of this fraction is determined by the amount of scattering that has taken place as the light passes through the atmosphere.

In order to design solar energy collectors which focus sunlight and deliver a required amount of power to the focus one must know the absolute value of

the sunlight reaching the collector, its variation throughout the day and the year, and what fraction of it may be focussed.

If the operation of the solar energy converter placed at the focus of the concentrator is dependent on the frequency content of the incident sunlight then this must also be known.

This chapter describes the nature of solar energy in terms of the parameters which are of interest to conversion schemes which employ focussing techniques. An explanation of the origin of solar energy and its spectral distribution is given. This is followed by sections on the fraction of the total solar energy output which reaches the outer atmosphere of the earth and how the energy and spectral content are affected by the atmosphere as the sunlight travels towards the ground level. A model is presented which accurately predicts the amount of direct solar energy received on the earth's surface or at any inclination to it, which takes into account the relative orientation of the receiving surface and the sun at any time during the year. The model uses a single parameter to modify the extraterrestrial values of solar energy, determined by solar astronomy. The parameter represents the clearness of the atmosphere for that day. A comparison between the model and measured data shows good agreement.

For the long term assessment of the suitability of a site for the location of focussing type collectors, a relationship needs to be established between the ratio of direct to diffuse sunlight received at ground level and its seasonal variation over many years. In the absence of a large database addressing these requirements, empirical attempts have been made at predicting the ratio of direct to diffuse solar intensity based on limited measured data. A discussion of these attempts is presented for completeness.

3.2 Source

3.2.1 Introduction

The chemical composition of the sun is mainly hydrogen with a lesser amount of helium. The sun transforms mass into energy via a fusion reaction which occurs in the sun's interior. The temperature at which this reaction takes place is 15×10^6 degrees Kelvin. As one moves from the center of the sun to its surface the temperature decreases. The surface of the sun, or photosphere, is a transition region where the density falls off rapidly and the temperature has fallen to approximately 6000 degrees Kelvin. Most of the radiation reaching the Earth emanates from the photosphere. Above the photosphere is the sun's atmosphere or chromosphere, so called since it selectively absorbs a certain part of the spectrum of radiation emitted from the photosphere.

3.2.2 Extra Terrestrial Solar Flux and Spectral Distribution

The radiant energy per unit time per unit area per unit wavelength emitted by a body at temperature T degrees Kelvin is given by:

$$F_\lambda = \epsilon_\lambda \frac{a}{\lambda^5(\exp^{\frac{b}{\lambda T}} - 1)} \qquad (3.1)$$

$$= \epsilon_\lambda B_\lambda(T) \qquad (3.2)$$

where:

$B_\lambda(T)$ is known as The Planck function

ϵ_λ is the emissivity of the body at wavelength λ

a=$2\pi hc^2$ (h=Planck's constant)

b=$\frac{hc}{k}$ (k=Boltzmann Constant)

The spectral distribution of the solar radiation can be approximated by assuming that the sun is a black body at T=5800 degrees Kelvin i.e ϵ_λ=1 for all wavelengths and T= the temperature of the photosphere.

In this case:

$$F_\lambda = B_\lambda(T) = \frac{a}{\lambda^5(\exp^{\frac{b}{\lambda T}} - 1)} \tag{3.3}$$

A plot of the distribution is shown in figure 3.1. It can be seen that approximately 51 % of the radiation emitted lies in the infra red region, that is with wavelengths longer than 0.7 μm, that 37 % lies in the visible region with wavelengths between 0.4 and 0.7 μm, and that 12 % lies in the ultraviolet region with wavelengths shorter than 0.4 μm.

The plot also shows the measured spectral distribution from the sun (solid curve). The differences arise from (i) the assumptions of radiative equilibrium i.e all the energy received by the photosphere is re-emitted and (ii) the absorbtion bands present within the chromosphere.

The maximum of the spectral distribution is given by the Wien displacement law:

$$\lambda_{max} = \frac{\alpha}{T} = \frac{2\pi hc^2}{T} \tag{3.4}$$

which for a Kelvin temperature of 5800 degrees corresponds to a wavelength of 0.500 μm
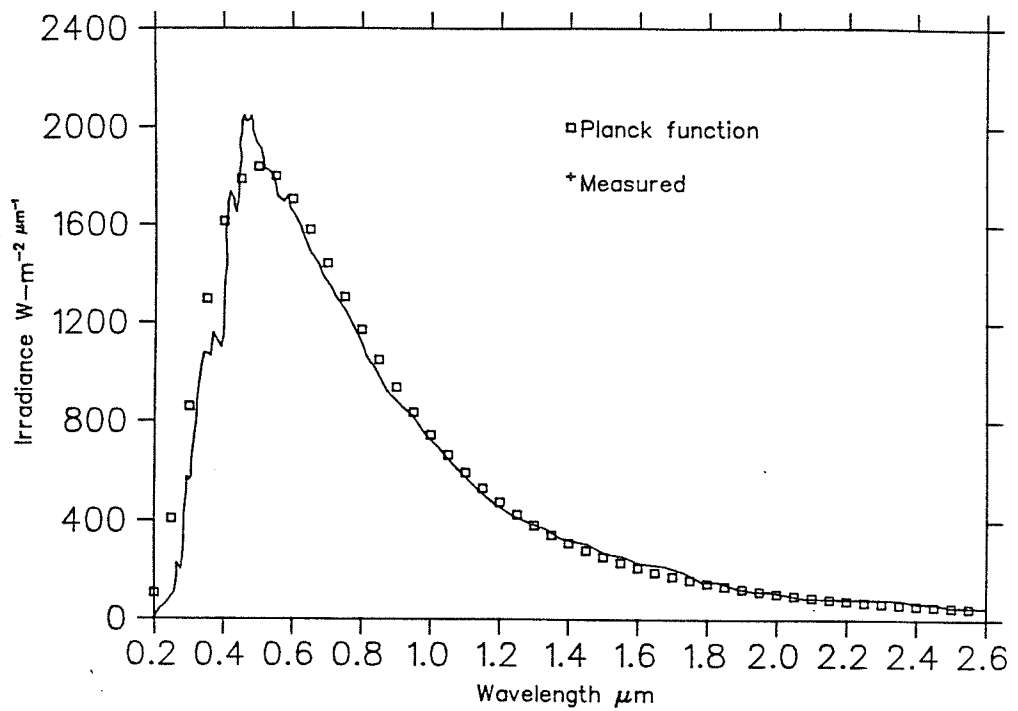
Figure 3.1 Comparison between measured spectral distribution from the sun and blackbody curve at a temperature of 5800 °K. [11] The spectral distribution of light from the sun is given by the Planck function by assuming the sun to be a "black body" source.

The total radiant intensity per unit time per unit area emitted by a black body is given by :

$$F = \int_\lambda B_\lambda(T) = \sigma T^4 \qquad (3.5)$$

where:

$$\sigma = 5.6696 \times 10^{-8} \text{ W m}^{-2} \text{ K}^{-4}$$

This expression is known as the Stefan-Boltzmann Law.

3.3 Solar Energy Reaching the Outer Atmosphere of the Earth

The radiation leaving the solar surface is emitted in all directions, i.e. it is diffuse. The Earth intercepts such a small amount of this radiation, that the angular spread represented by the earth at the sun is small enough (approximately 0.5°) that the radiation incident on the Earth's outer atmosphere is essentially beam like i.e parallel rays.

The total radiant power emitted by the sun is given by:

$$P_s = \sigma T_s^4 4\pi R_s^2 \qquad (3.6)$$

$$= 3.91 \times 10^{26} \text{ Watts}$$

Where the subscript s refers to the sun. As the distance from the sun increases, this power is spread over spheres of increasing area. At the mean distance of the Earth from the sun, (1.496 x 10^{11} m) the radiant intensity will be:

$$F_e = \frac{P_s}{4\pi R_{es}^2} \qquad (3.7)$$

$$= 1382 \text{ Watts/m}^2$$

The value of the radiant intensity and its spectral distribution just outside the Earth's atmosphere form a useful parameter, which is relatively constant throughout the year and is therefore known as the solar constant. It is defined as the energy incident on unit area exposed normally to the sun's rays at the mean Sun-Earth distance. The currently accepted value for the solar constant is 1353 W/m^2 and is the result of nine series of measurements made from high altitude balloons, X15 and other high altitude aircraft and a Mariner Mars probe during the years 1967-70 [11]. The spectral content of the radiation was measured from jet aircraft at an altitude of 11.6 km [12].

3.4 Solar Energy Received at the Surface of the Earth

3.4.1 Introduction

The solar energy which reaches the surface of the Earth can be quite different in intensity and spectral distribution compared to the extraterrestrial case.

The amount of energy available extraterrestrially is reduced by a combination of effects such as the time of day, the time of year, and the latitude of the receiver. As the sunlight passes through the atmosphere its intensity is reduced due to selective absorbtion by dry air molecules, water molecules and suspended particulate matter. The amount of absorbtion is determined by the path length of the sunlight through the atmosphere, which for a

particular location on the Earth is in turn determined by the latitude of the location and the time of year. The parameter which describes the path length is known as the air mass.

Solar radiation is essentially monodirectional extraterrestrially, scattering takes place as the sunlight passes through the atmosphere. On reaching the surface of the Earth, the sunlight will have a diffuse component dependent on the air mass through which it has passed.

The amount of solar radiation received by the surface of the Earth will further depend on the angle between the sun's rays and the normal to the receiving surface. This angle will change throughout the day as the sun appears to move through the sky. The effect of this on the amount of solar energy received is known as the obliquity effect.

The following section describes how these influences effect the extraterrestrial solar energy to give the solar energy received at the surface of the Earth.

3.4.2   Solar Astronomy

It would be useful to separately determine the effect of location and time of year alone on the amount of solar energy received at the surface of the Earth, i.e to assume that the atmosphere plays no part in the absorption of sunlight. This is known as the zero air mass condition and a consideration of solar astronomy will yield the information.

The Earth moves in a fixed plane about the sun with the sun located at one of the foci of an ellipse, this plane is known as the ecliptic plane. The aphelion and perihelion distances of the Earth to the sun differ by less than 2 % from the mean value (1.496×10^{11} m) For the purposes here it is sufficient to assume that the Earth moves around the sun in a circular fashion and that

the effects of the other planets on the orbit of the Earth are negligible.

The axis of rotation of the Earth is inclined to a line perpendicular to the ecliptic plane at an angle of 23.5° and remains constant throughout the year. The Earth makes one revolution about its axis every 23.93 hours and one revolution about the sun every 365.25 days.

At one point in the orbit the Earth's axis is tilted towards the sun (see figure 3.2). This is known as the Summer solstice. It can be seen that in this orientation, for locations in the Northern hemisphere, as the Earth rotates, more time will be spent in the light of the sun than in the shade. At the Winter solstice the opposite is true. At the autumnal and vernal equinoxes day and night are of equal duration. It can be seen then, that the combined motion of the rotation of the Earth about its axis and the rotation of the Earth about the sun gives rise to seasons and to the different lengths of daylight throughout the year. (Except at the equator which has equal days throughout the year.)

The amount of solar energy incident on the surface of the Earth is determined by the angle between the normal to the surface and the sun's rays. The apparent motion of the sun through the sky in terms of solar co-ordinates will yield this information as shown below.

Geocentric co-ordinates

Consider a Cartesian coordinate system with its origin at the center of the Earth. Let the Z axis be along the Earth's North South axis with the X and Y axes in the equatorial plane (see figure 3.3). The X axis represents some local meridian.

In this system of coordinates the sun's position can be fixed by two angles,

19
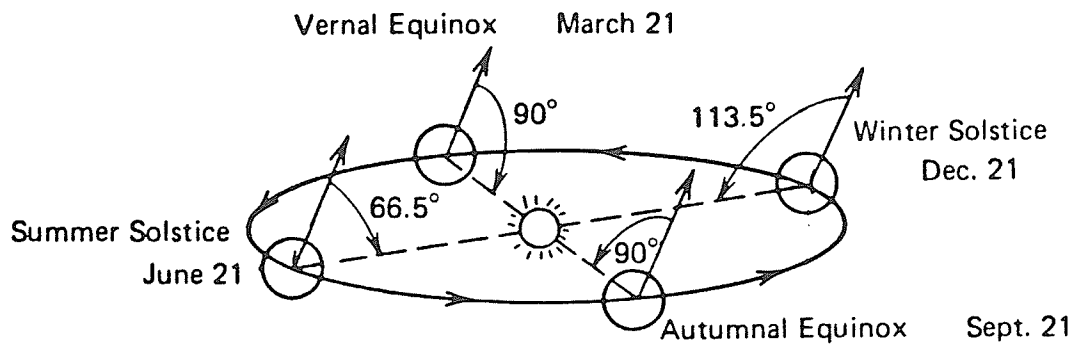
Figure 3.2 The variation in angle between the axis of the earth and the ecliptic plane gives rise to the different length of days and throughout the year [13].
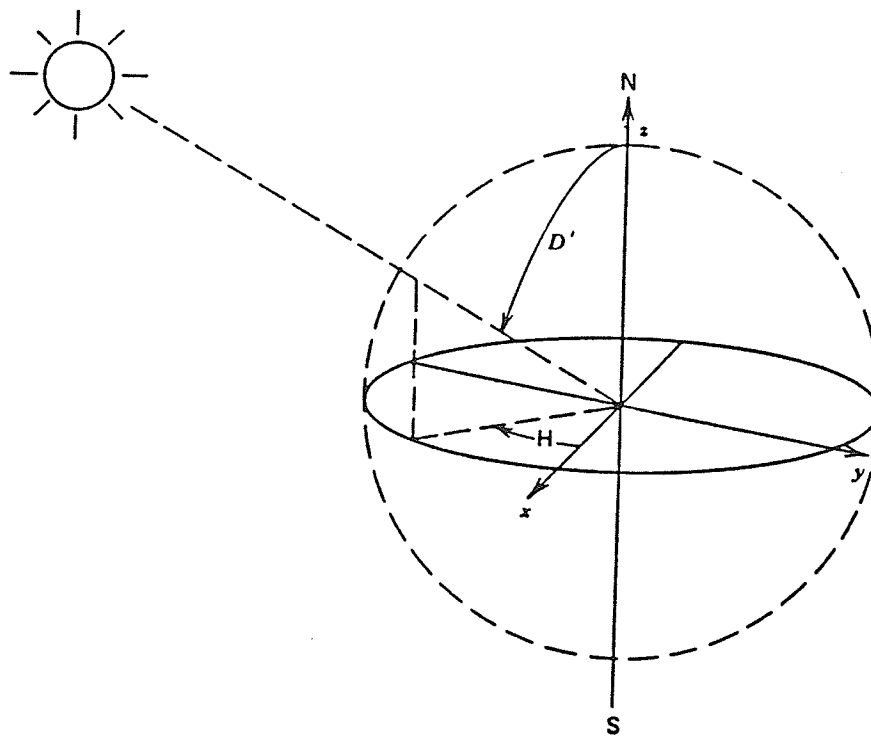
Figure 3.3 Conventions used in geocentric solar coordinates. [13]

the co-declination D′ and the hour angle H. The co-declination is the angle between the North South axis and the line in the ecliptic plane joining the Earth and sun.

It can be shown that:

$$\cos D' = \sin 23.5 \sin \alpha \qquad (3.8)$$

where α is the angle between the Earth sun line on the day in question and that line at the vernal equinox.

Assuming a circular orbit one may write:

$$\alpha = \frac{360\, n}{365.25} \qquad (3.9)$$

where n is the number of days after the vernal equinox.

therefore:

$$\cos D' = \sin 23.5 \sin \left(\frac{360\, n}{365.25} \right) \qquad (3.10)$$

The co-declination therefore varies from 66.5 degrees at the Summer solstice to 113.5 degrees at the Winter solstice (and is 90 degrees at the equinoxes).

The hour angle H is the angle between the projection of the sun's rays in the equatorial plane and the X axis (which represents the location of solar noon). The hour angle is related to the observers local solar time by:

$$H = \pm \frac{360°}{24} t \qquad (3.11)$$

Where t is the number of hours before or after solar noon.

Local solar co-ordinates

For an observer situated on the surface of the Earth, it is more convenient to use the zenith angle and the azimuth angle as the solar co-ordinates, as shown in figure 3.4.

The co-ordinate system is located on the surface at Latitude L and the Z axis is taken as the vertical, the zenith angle Z is the angle between the rays from the sun and the vertical, and the azimuth angle A is the angle between the projection of the sun's rays in the horizontal (X-Y) plane and due south. The azimuth angle is zero at solar noon, negative before and positive after solar noon.

It is possible to relate the local co-ordinates Z, A to the geocentric co-ordinates D' and H using basic vector relations which yield:

$$\cos Z = \cos D'\cos(90 - L) + \sin D'\sin(90 - L)\cos H \qquad (3.12)$$

$$\tan A = \frac{\sin D'\sin H}{\sin D'\cos(90 - L)\cos H - \cos D'\sin(90 - L)} \qquad (3.13)$$

Obliquity Factor

The amount of solar energy intercepted by a fixed surface under zero air mass is determined by the angle θ between the perpendicular to the surface and the sun's rays. The function $\cos\theta$ is called the obliquity factor. This factor depends on the local solar co-ordinates Z and A and on the tilt co-ordinates of the surface Δ and ψ with respect to the surface of the Earth, where Δ is the angle between the perpendicular line to the surface and the vertical, and ψ is the angle between the projection of the surface normal

22
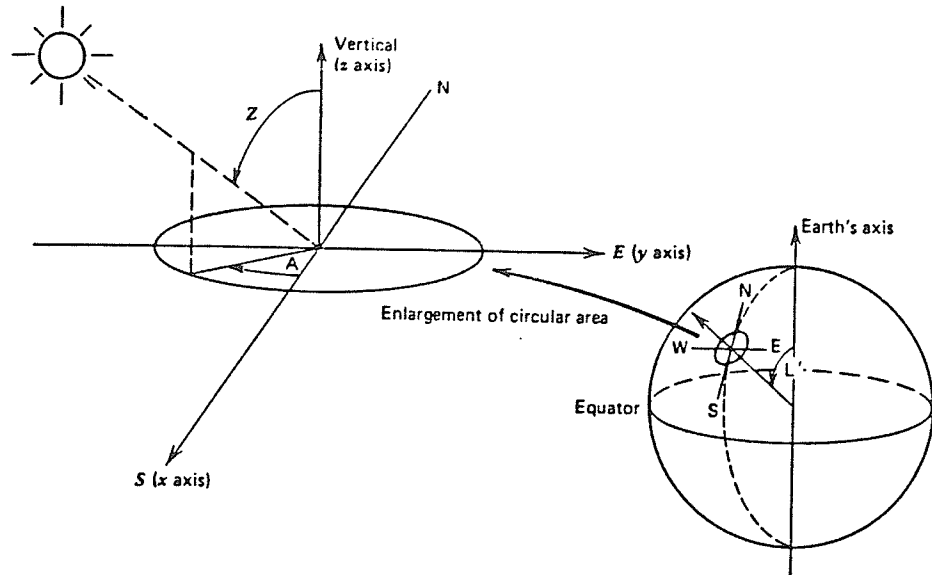
Figure 3.4 Conventions used in local solar coordinates. [13]
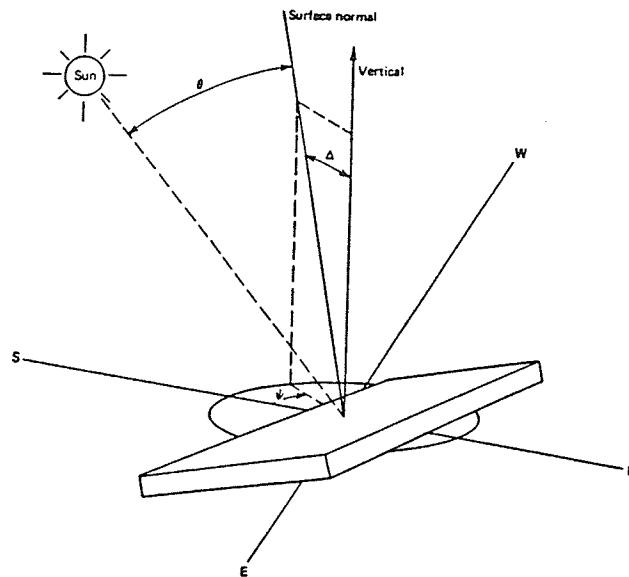
Figure 3.5 Obliquity effect geometry. [13] The amount of solar energy intercepted by a fixed surface under zero air mass is determined by the angle θ between the perpendicular to the surface and the sun's rays. The function $\cos\theta$ is called the obliquity factor. This factor depends on the local solar co-ordinates Z and A and on the tilt co-ordinates of the surface Δ and ψ with respect to the surface of the Earth.

23

in the horizontal plane and due south (figure 3.5). The obliquity of the sun's rays to an inclined surface is given by:

$$\cos\theta = \cos Z \cos \Delta + \sin Z \sin \Delta \cos(A - \psi) \qquad (3.14)$$

3.4.3 Insolation at zero air mass

The intensity incident on a surface under zero air mass conditions is given by:

$$F(t) = I_{sc} \cos \theta(t) \qquad (3.15)$$

Where I_{sc} is the solar constant and $\cos\theta$ is the obliquity factor between the sun's rays and the surface normal. Using the equations above for $\cos\theta$ as a function of Z, A, Δ and ψ one can establish the time dependence of $F(t)$ for various orientations of a surface at various latitudes at various times of the year.

3.4.4 Effect of the Atmosphere on Solar Radiation

The degree to which the solar energy available is reduced as it proceeds from outside the atmosphere to the surface of the earth is determined primarily by the state of the atmosphere. The atmosphere affects the solar radiation by absorption and scattering, the amounts of each depend on the composition of the atmosphere and the air mass through which the sunlight passes.

24

Atmospheric Absorption

The atmospheric constituents are N_2, O_2, CO_2, H_2O, O_3, CO, CH_4, flourine and hydrocarbon emissions in suspension.

The fraction of solar energy absorbed is described by the mass absorption cross section $\sigma^a(\lambda)$ which is dependent on the frequency component of the sunlight. Molecules of O_2 and N_2 do not absorb appreciably in the solar spectrum. Absorption is mainly due to molecules of CO_2, H_2O and hydrocarbon emissions in the troposphere i.e the lower part of the atmosphere near the Earth. The molecules have appreciable characteristic absorption bands in the infra-red portion of the solar spectrum. There is also some absorbtion by ozone in the stratosphere (uppermost part of the atmosphere) which absorbs in the ultra-violet region of the solar spectrum.

The spectral distribution of terrestrial sunlight at various air masses is shown in figure 3.6. The latitude of Winnipeg classifies it as an air mass 2 location.

Atmospheric Scattering

Unlike absorption, scattering does not convert the radiant energy of the sun into heat but rather redirects it in other directions. It is therefore responsible for the diffuse component of solar radiation. On a clear day scattering is produced primarily by Oxygen and Nitrogen. The mass scattering cross section $\sigma^s(\lambda)$ varies smoothly with wavelength according to Rayleigh's law:

$$\sigma^s(\lambda) = \frac{C}{\lambda^4} \tag{3.16}$$

From this it can be seen that shorter wavelengths are scattered more than longer wavelengths and the fourth power results in appreciable scattering in
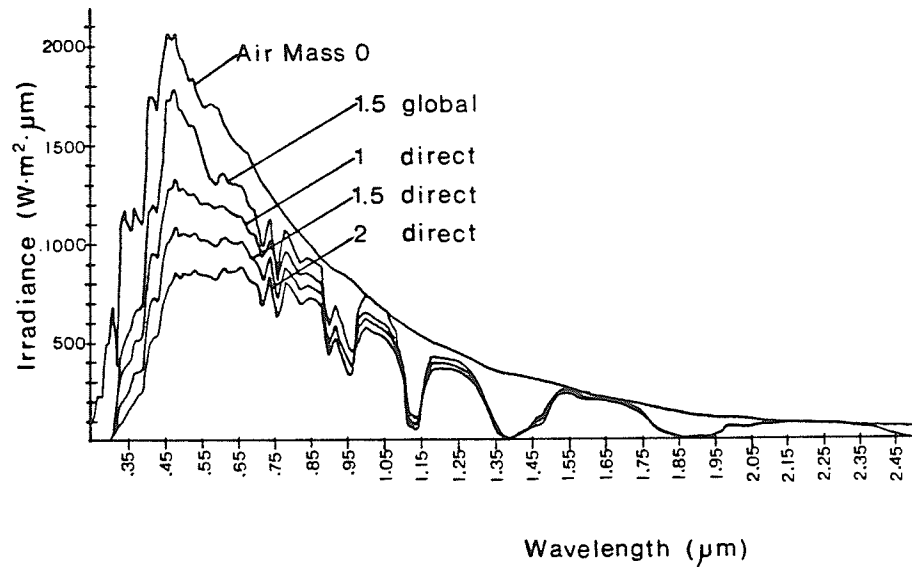
Figure 3.6 Solar spectral distribution at several air mass levels. The spectral distribution of sunlight reaching the earth is dependent on the length of the path through the atmosphere. This parameter is known as the air mass. The latitude of Winnipeg classifies it as an air mass 2 location.

the blue-violet region of the visible spectrum.

3.5 Approximate Equations For Direct Solar Radiation Received at the Surface of the Earth

The solar disk presents a full angle of 0.53 degrees, measured form a point on the Earth. The radiation which has survived scattering and absorption and lies within an angular spread of 0.53 degrees from the line representing the center of the sun is called direct radiation. If one assumes that the atmosphere is uniformly mixed i.e that the density depends on height alone $\rho = \rho(h)$, then one can produce an equation which represents the direct solar radiation.

Let s be the distance measured from the top of the atmosphere as shown in figure 3.7

The fractional change in spectral intensity I when the beam passes through a layer ds can be expressed as: [13]

$$\frac{dI_\lambda}{I_\lambda} = -\rho(s)\sigma(\lambda)dl \qquad (3.17)$$

$$= -\rho(s)\sigma(\lambda)\frac{ds}{\cos Z} \qquad (3.18)$$

Where $\rho(s)$ is the density and $\sigma(\lambda)$ is the total attenuation cross section due to scattering and absorbtion:
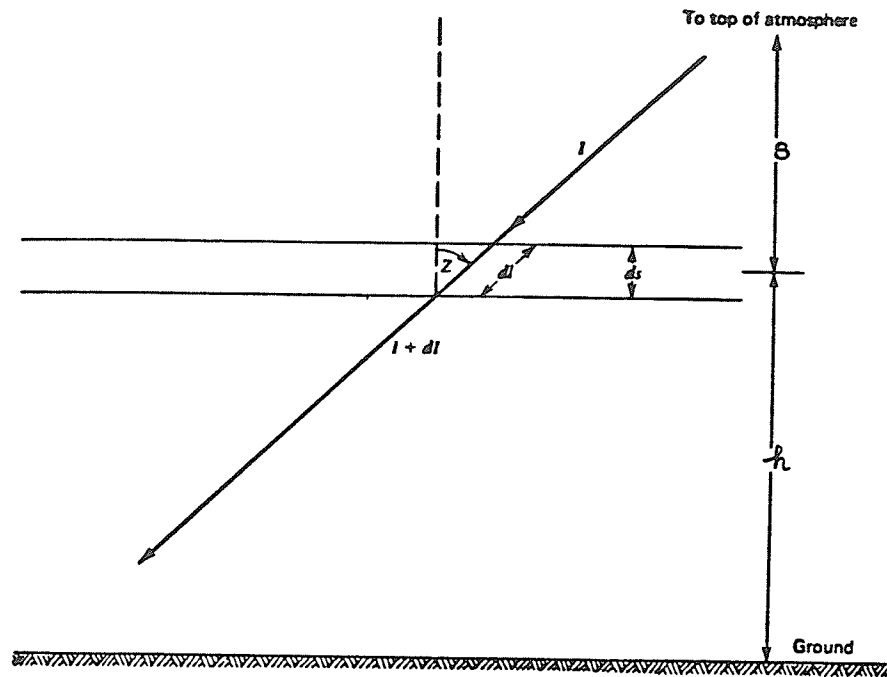
Figure 3.7 Absorption of direct solar radiation. [13] If one assumes that the atmosphere is uniformly mixed i.e that the density depends on height alone $\rho = \rho(h)$, then one can produce an equation which represents the direct solar radiation. Here s = distance measured from the top of the atmosphere and Z = zenith angle.

$$\sigma(\lambda) = \sigma^a(\lambda) + \sigma^s(\lambda) \tag{3.19}$$

The above equation can be written as:

$$\frac{dI_\lambda}{I_\lambda} = -k_\lambda \frac{ds}{\cos Z} \tag{3.20}$$

Where $k_\lambda = \rho(s)\sigma(\lambda)$ is known as the spectral attenuation coefficient.

At ground level one can express the spectral intensity by integrating the above:

$$I_\lambda = (I_\lambda)_{s=0} \int_0^\infty -k_\lambda(s) \frac{ds}{\cos Z} \tag{3.21}$$

to give:

$$I_\lambda = I_{sc_\lambda} e^{-\frac{\tau_\lambda}{\mu_0}} \tag{3.22}$$

where

$$I_{sc_\lambda} = (I_\lambda)_{s=0} \tag{3.23}$$

is the spectral intensity of the solar constant and:

$$\tau_\lambda = \int_0^\infty k_\lambda(s) ds \tag{3.24}$$

is called the spectral optical thickness ($\mu_0 = \cos Z$)

The direct flux incident on a surface inclined at an angle θ with respect to the beam is given by:

29

$$F_\lambda = \cos\theta \, I_\lambda = \cos\theta \, I_{sc_\lambda} \, e^{-\frac{\tau_\lambda}{\mu_0}} \qquad (3.25)$$

The total direct flux intercepted by a surface is given by integrating the above expression for all λ:

$$F(\text{dir}) = \int_0^\infty \mu I_{sc_\lambda} e^{-\frac{\tau_\lambda}{\mu_0}} \, d\lambda \qquad (3.26)$$

$$= \mu e^{-\frac{\tau}{\mu_0}} I_{sc} \qquad (3.27)$$

where I_{sc} is the solar constant (1353 W/m^2), $\mu = \cos\theta$ and $\tau =$ the average optical thickness.

Values of $\tau < 0.3$ represent clear skies, whereas values > 1.0 represent opaque skies. A comparison between the prediction and measured data for Winnipeg on 5th April 1983 using a value of $\tau = 0.32$ is shown in figure 3.8. The good agreement shown provides a useful way of predicting the variation in direct intensity throughout the day. The value of τ may be determined for particular time by taking a single measurement of the direct component of the incident sunlight and comparing the value with equation (3.27).

3.6 Models of Solar Radiation

Under cloudy conditions the equations which predict direct solar radiation do not hold. Theories which attempt to predict the diffuse component of radiation are very complex and give only approximate results. Consequently, semiquantatative analyses have been performed. These attempt to predict the total, diffuse or direct flux on horizontal and inclined surfaces on clear

30
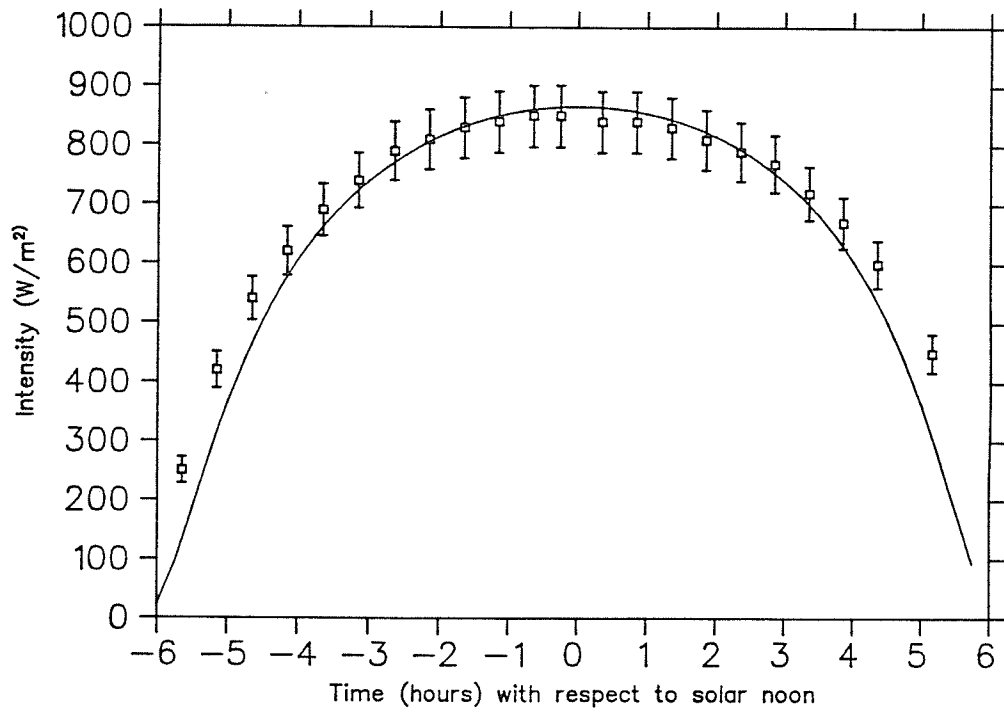
Figure 3.8 Comparison between prediction and measured direct insolation data for Winnipeg on 5-Apr-83. The variation in direct intensity at ground level may be predicted by modifying the expression for the air mass zero case with a single parameter τ which represents the clearness of the atmosphere for that day.

or cloudy days by utilizing previously recorded data for that location.

By analysing data for North Carolina, Liu and Jordan [14] formulated an empirical equation which can be used to predict the hourly and daily diffuse and direct radiation under a cloudless atmosphere on a horizontal surface when the total radiation (direct and diffuse) is known.

The equation is:

$$\tau_d = 0.27 - 0.29\tau_D \tag{3.28}$$

where τ_d is the transmission coefficient for direct solar radiation and τ_D is that for diffuse radiation. The transmission constant was determined by taking the ratio of the measured direct or diffuse intensity value and the extraterrestrial value, assuming the latter to be constant. The total transmission coefficient is $\tau_T = \tau_d + \tau_D$ such that:

$$\tau_d = 0.38 - 0.42\tau_T \tag{3.29}$$

Measurements were made over a 28 day period at Hump mountain, from which the relationship above was derived. Although valid only on clear days and for horizontal surfaces the relationship provides a means of estimating the intensity of diffuse or direct radiation when the total radiation is known.

Liu and Jordan also showed that an empirical relationship exists between the daily diffuse radiation and the daily total radiation. The relationship is shown in figure 3.9. Data were recorded over a 10 year period for Blue Hill Massachusetts and were normalized such that:

$$K_d = \frac{D}{H_0} \tag{3.30}$$
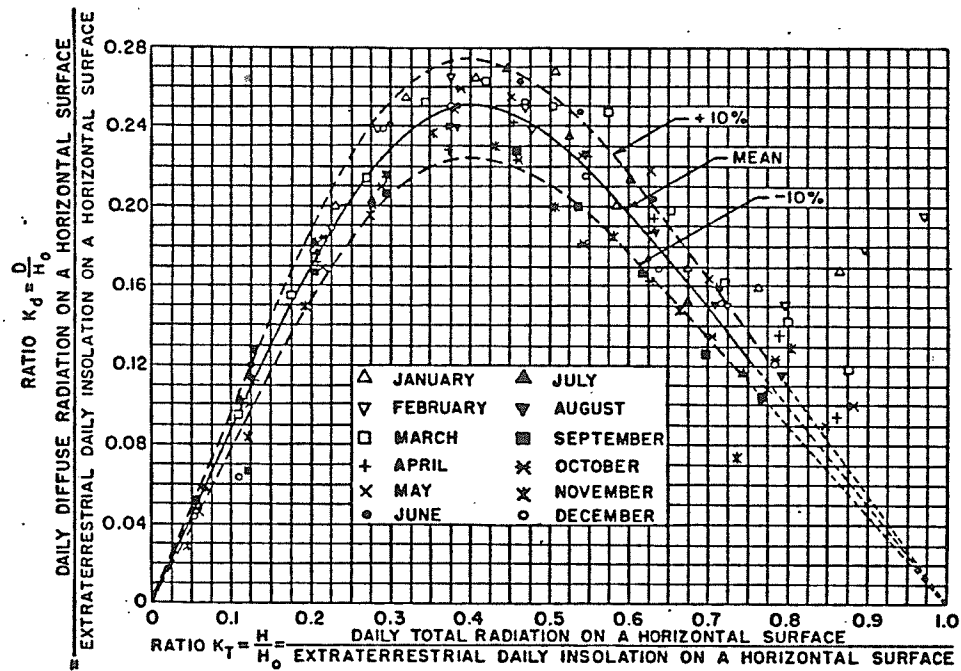
Figure 3.9 The relation between the daily total radiation and the daily diffuse radiation on a horizontal surface. [14] Theories which attempt to predict the diffuse component of radiation are very complex and give only approximate results. Liu and Jordan showed that an empirical relation exists between the daily total radiation and the daily diffuse radiation incident on a horizontal surface.

33

$$K_t = \frac{H}{H_0} \qquad (3.31)$$

where D is the daily diffuse radiation on a horizontal surface, H is the daily total radiation on a horizontal surface and H_0 is the monthly average of the extraterrestrial insolation on a horizontal surface,

Work by Ruth and Chant has improved on the above relationships by replacing the monthly average of extraterrestrial insolation on a horizontal surface by its daily value [15] The extraterrestrial insolation being computed from:

$$H_0 = \frac{24}{\pi} r I_{sc}(\cos L \cos D \sin \omega_s + \omega_s \sin L \sin D) \qquad (3.32)$$

where r is the ratio of the daily normally incident extraterrestrial insolation to the solar constant, which accounts for the small variation in the extraterrestrial solar radiation throughout the year. (The solar constant is assumed fixed). I_{sc} is the solar constant, L is the latitude D is the declination and ω_s is the sunset angle given by:

$$\omega_s = \cos^{-1}(-\tan L \tan D) \qquad (3.33)$$

This revealed a latitude dependence on the correlations between K_d and K_t

Although the work of Liu and Jordan yields only average values, it provides a means for estimating the amount of daily direct and diffuse radiation on horizontal surfaces. It also has been used extensively by designers in the determination of the heating and cooling requirements of buildings.

Other approaches to empirical evaluations of the solar intensity at the surface of the Earth estimate the transmission through a clear atmosphere, modify the expression to account for cloudiness and add an estimated diffuse com-

ponent [16]. This approach has the advantage that the parameters used can be associated with the geographical area of interest and constitutes a simpler input for feasibility studies.

Since many more weather prediction stations keep records of number of hours of bright sunshine than radiometric values of diffuse and total solar radiation, attempts have been made to correlate the direct and diffuse flux with the number of hours of bright sunshine [17].

The depletion of extraterrestrial solar radiation by ozone in the upper atmosphere has also been included in empirical formulae [18] though this represents only a small amount of the total depletion of the solar radiation. The model has as inputs latitude, longitude and day of the year and gives good agreement with ozone depth measurements over North America.

The assumption of isotropic diffuse sky radiation in the Liu and Jordan model has been improved on by modelling a more realistic view of the angular distribution of diffuse radiation which includes the effects of horizon brightening and circumsolar radiation [19].

3.7   Summary

The amount of direct solar intensity available and its variation throughout the day provide vital information in the design and evaluation of solar energy conversion devices. A study of solar astronomy yields the amount of direct intensity available at ground level under air mass zero conditions in terms of the location of the observer and the time of year. This expression may be modified by including a single parameter τ, which represents the clearness of the atmosphere on cloud free days. The result is an accurate representation

of the variation of direct solar intensity throughout the day at any time of the year.

The prediction of solar intensity under cloudy conditions is very difficult to accomplish. In terms of the applicability to the proposed converter, only the number of days of continuous cloud cover, and at what time of year they occur needs to be known. Focussing type collector systems will not function under cloud cover. The number of days of cloud cover needs therefore to be taken into account in the design of focussing type collector systems so that appropriate buffer storage may be incorporated into the system at the engineering stage. The variation in cloud cover levels needs to be recorded over a number of years to determine the suitability of the location for focussing type collectors.

The instruments which record solar radiation data are described in the following chapter.

Chapter 4

The Measurement of Solar Energy

4.1 Introduction

Models which predict the amounts of direct and diffuse solar energy reaching the surface of the Earth need to be verified by comparison with actual measured data taken over several years. This chapter describes those instruments which measure terrestrial solar energy and the standards which have been adopted to calibrate them.

A second reason for establishing a solar insolation database is to determine the suitability of a site for locating a solar receiver or complex of receivers. The ratio of direct to diffuse radiation will determine the suitability of the site as a location, for example, for focussing type or flat plate type collectors. For concentrating collectors optimum sites will have high insolation levels, small cloud cover and few days of continuous cloud cover. The energy available has to be measured over a period of several years in order to determine average values for the required data.

If the insolation level for a particular site is not accurately known, then the

system may not be able to provide the required energy or may require the outlay of unnecessary capital.

4.2 Measurement of Terrestrial Insolation

The term insolation refers to the intensity and also to the spectral content of the incident solar energy. In practice one measures the diffuse and direct components of the solar radiation with instruments which have a constant response over the entire solar spectrum. It is also desirable to use instruments whose response is linear with the amount of solar energy received.

4.2.1 Measurement of Direct Radiation

The term direct solar radiation describes those rays which are contained within the solid angle presented at the earth by the solar disk, this full angle has a value of 0.53 degrees. A device manufactured by the Eppley Laboratory of New York has now become fairly standard for the measurement of the direct component of solar radiation [20]. Called a Normal Incidence Pyrheliometer, or n.i.p, it consists of an array of thermocouples which form a sensor. The sensor is placed at the base of an arrangement of collimator tubes and aperture stops which limit the field of view of the sensor. The surface area of the sensor is 0.57 cm^2. It is coated with an optical black laquer which gives it a constant spectral response. The sensor is located in a tube 20.6 cm long with an aperture stop of 1.03 cm at the other end of the tube. In practice the radiometer is mounted on a suitable tracking arrangement so that it is always pointing at the sun. The normal incidence pyrheliometer is shown in figure 4.1
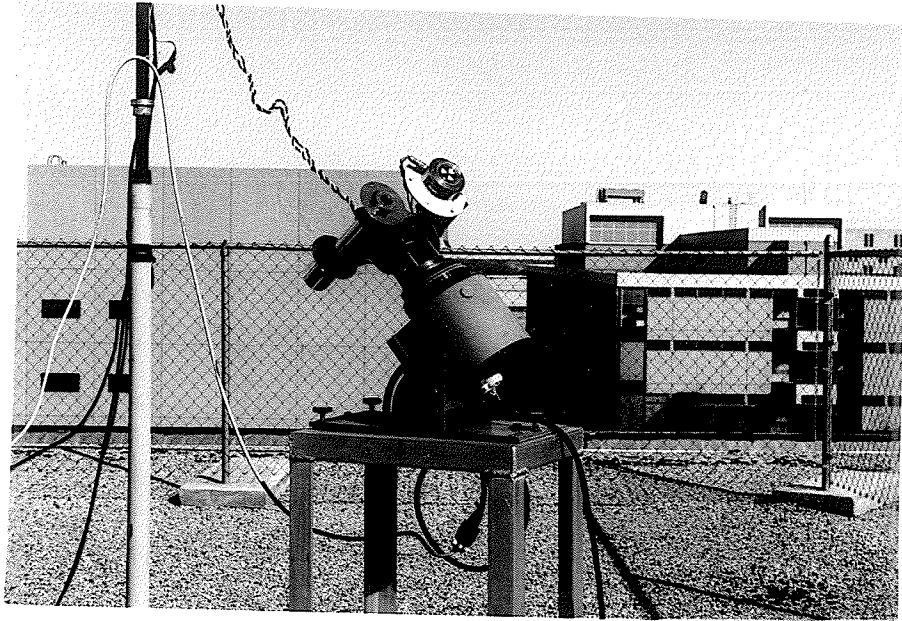
Figure 4.1 Instruments for the measurement of solar intensity levels. The normal incidence pyrheliometer (left hand side) measures only the direct component of sunlight, the pyranometer measures the total diffuse and direct components. The radiometers are mounted on a sun tracking table.

The geometry of the n.i.p. results in a full angle field of view for the receiver of 5.72 degrees. The sun's disk presents a full angle of 0.53 degrees, the radiation from which can be regarded as direct radiation. The radiometer also therefore receives radiation from a region of the sky adjacent to the sun's disk. This region is known as the solar aureole, which is the apparent increase in the solar diameter due to small angle forward scattering of solar radiation by atmospheric particles whose dimensions are comparable to the wavelengths of the scattered light (Mie scattering). Thus the apparent solar diameter is dependent on the amounts and sizes of the material through which the sunlight has passed.

It has been shown by varying the angle of view of a n.i.p. that on a clear day (no cloud cover) the radiation from the solar aureole to a full angle of 5.72 degrees is of the order of 1% of that contained within the true solar diameter [21]. On a day of thin cloud cover while the n.i.p. reading was 630 W/m^2 (i.e approximately 70 % of the maximum direct solar component that reaches the earth) it was found that 11% of the measured intensity was contained within an annulus formed by angles 1.01 degrees and 2.86 degrees from the center of the sun. The radiometer aperture is thus set so that the total radiation that can be regarded as beam radiation is always measured. It can be seen that the effect of the solar aureole may need to be taken into account in the design of concentrating solar systems, and that the effect will depend upon the location of the collector system.

4.2.2 Measurement of Diffuse Radiation

A typical instrument for measuring diffuse radiation is the Eppley "black and white" pyranometer. The receiver is in the shape of a disk, mounted

horizontally and sealed from the environment under a hemispherical dome of glass of constant spectral transmission. The receiver consists of two adjacent flat surfaces, one black and one white, as shown in figure 4.1. Each surface has a thermocouple fixed to it and the thermocouples generate a voltage that is directly proportional to the temperature differences between the black and white surfaces [20]. It is necessary that a horizontally fixed pyranometer has a response that is independent of the incident radiation. The area of the receiving thermopile is constant. Its output is therefore proportional to the cosine of the angle of incidence of the radiation. To produce the required output an "inverse cosine response" must be incorporated into the optical design of the pyranometer. The design involves introducing a slight curvature into the thermopile surface. By using a hemispherical quartz window above the thermopile, reflection varying with angle of incidence at the glass surface is compensated for by refraction effects.

4.2.3 Electrical Compensation Radiometers

The radiometers mentioned above employ a temperature dependent solid state device to adjust the output of the devices for changes in ambient temperature. In this way the output of the device is made approximately linear with the intensity of incident solar radiation.

To avoid the inaccuracies caused by this technique, an electrical compensation radiometer may be used. In this type of radiometer a receiver surface is connected to a thermopile which produces a voltage when solar radiation is incident upon it. Within the radiometer a similar sensor, which is shielded from solar radiation, is heated with electrical energy. When the output from the thermopile attached to this sensor matches that from the illuminated

41

sensor then the electrical energy applied to the second sensor is equal to the solar energy incident on the first.

This technique was used in the construction of a "standard" radiometer called an Angström type against which other types of radiometers can be calibrated.

4.2.4 Measurements from satellites

The amount and distribution of solar energy, received by the surface of the earth, may be determined by measuring the intensity of sunlight reflected by the surface using earth - orbiting satellites. By digitizing the image formed by a television camera mounted in an orbiting satellite and by introducing a grey-scale to the intensities of light received by the camera, it is possible to measure the total solar intensity distribution over the surface of the earth. The technique of determining solar energy levels from space centers on the development of suitable algorithms to correlate the intensity received by the camera with that received at ground level [22]. Two algorithms are required, the first operates on data for clear days where the sunlight is reflected by the surface of the earth, and the second operates on the data for cloudy days where the sunlight is mostly reflected by clouds. In the second case the height of the cloud needs to be taken into account in the algorithm. At the present time models only exist which attempt to correlate the total radiation at ground level (i.e the sum of the direct and the diffuse components) with the intensity recorded by the satellite.

4.3 History of Radiometric Standards

The standards of radiometry are based upon the measurements of so-called absolute instruments which have been constructed from time to time and against which all other instruments are calibrated.

In the years before 1956 two scales of radiometry existed; the Angström scale of 1905 (AS05), which was used mainly in Europe and the Smithsonian scale of 1913 (SS13) which was favoured in the United States. In 1956 at an international comparison of pyrheliometers from various countries it was found that the outputs from radiometers which represented the "standard" for each scale differed by 3.5%.

In consequence a new scale, the International Pyrheliometry scale (IPS56) was adopted which unified the readings from the standard instruments. Its value was set 2% below SS13 and 1.5% above AS05.

In the mid 1960's an anomaly in the equilibrium temperature of a spacecraft in flight, from that which was predicted from solar simulation studies was observed. This brought into question the validity of irradiance measurements made with respect to the scale of IPS56. In consequence, Kendall [23] developed an accurate electrical compensation radiometer known as the Primary Absolute Cavity Radiometer whose measurement accuracy was demonstrated by an experimental determination of the Stefan Boltzmann constant.[24] The so called PACRAD radiometer gave readings 2% higher than the standard instruments of IPS56. In 1973 it was accepted as the new international reference for the absolute scale of units [25]

4.4 Solar Insolation Data for North America

Although there is a considerable amount of measured information pertaining to the amount of solar radiation incident on the earth's surface, it is not in a form that may be easily used to determine the suitability of a site for the location of a focussing type solar collector. The most frequently kept statistics are total (direct and diffuse) radiation on a horizontal surface and number of sunshine hours [26]. Records of direct radiation have rarely been kept. The quality of recorded data is in need of improvement. The number of stations which record both the direct and diffuse components of sunlight is too few to accurately represent the distribution over North America. Further, the averages of the values of the data measured are questionable since the stations have varying levels of operational status. The calibration frequency and status of the instruments, has not been ascertained over time and therefore leads to a further reduction in the accuracy of the data. Although the quality of the data needs improvement, attempts have been made to predict the direct radiation component from the total data using the results of Liu and Jordan [27]. The results are shown in figure 4.2. The curves suggest that locations as far north as Winnipeg may be equally suitable for the location of concentrating type solar collectors as parts of Texas.

4.5 Summary

In order to determine with confidence the distribution of solar radiation across North America an accurate data base is required. The spatial density of the stations needs to be increased. The type of measurements recorded needs to be increased to include direct, diffuse and total radiation at several
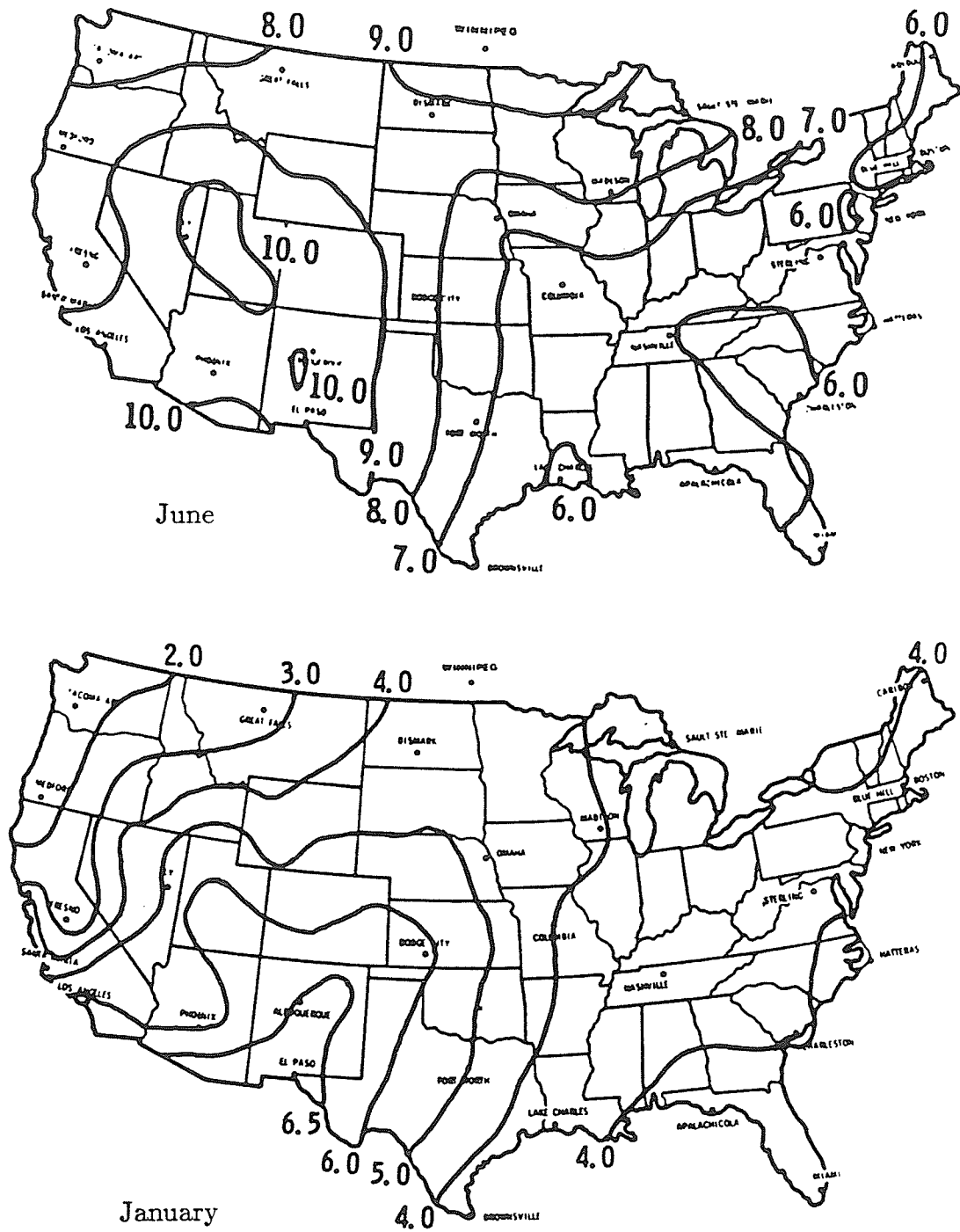
Figure 4.2 Direct Normal radiation in North America for June and January (kW-hrs/m². The data shown is derived using the relationship of Liu and Jordan from the total intensity recorded on a horizontal surface.

angles of incidence. The calibration accuracy of the radiometer used needs to be determined at regular intervals. Finally the time each station is not recording data due to a system malfunction needs to be minimized. It is unlikely that such a detailed program will be mounted at ground level. Fortunately satellites provide the spatial resolution required but much work is needed in correlating the signal output from the satellite camera with, for example, the direct component of sunlight received. This can only be done by comparison of the algorithm outputs with data measured at ground level.

The suitability of a site for the location of solar energy converters which offer potentially high efficiencies is dependent on the amount of direct sunshine received over the course of the year. At present there is no substitute for an accurate data base of measurements at ground level, established over several years which contains measured values of direct and total radiation at several inclinations. The extended periods of cloud cover from this data will yield the information required by system designers so that appropriate buffer storage may be provided to cover the periods when the direct component on the sunlight is negligibly small.

Chapter 5

Solar Collectors

5.1 Introduction

The topic of solar collectors encompasses all kinds of construction which utilize the energy from the sun in their design. This includes applications from buildings with shading extensions so that rooms are illuminated in Winter and shaded in Summer, to computer controlled, sun tracking focussing systems.

Of particular interest to us are those schemes which have potentially high conversion efficiencies. In converting solar energy to more useful forms higher efficiencies may be obtained by using higher temperature receivers. This is achieved by focussing the sunlight incident on a large area onto a smaller area thereby increasing the intensity of the sunlight incident on the receiver.

This chapter reviews the forms of solar energy collectors that are currently used in the context of their applicability to developing a test facility for investigating highly efficient forms of solar energy conversion.

Solar energy collectors can be broadly classified into active and passive types.

Passive solar collection describes the use of the position of the sun throughout the year in, for example, the design of buildings. Of more interest to us is active collection, in which solar energy is collected and converted to more useful forms.

Active solar collectors can be classified into those which are mounted so that they track the sun as it appears to move through the sky, or those which are fixed at optimum angles of tilt and azimuth so that they collect as much energy as possible throughout the day, i.e they are called tracking and nontracking collectors.

Tracking collectors can further be divided into those which focus the sun's rays and those which do not. In this chapter a description will be given of each type of collector:

5.2   Non Tracking Collectors

5.2.1   Flat Plate Collectors

In this type of collector, tubes containing a heat exchange liquid are welded to a large flat plate. The Plate is painted black for maximum absorption over the solar spectrum. The collector is placed in a frame with a transparent cover to reduce the re-radiated heat loss. A typical plate plate collector is shown in figure 5.1. For maximum average efficiency throughout the day, the collector is tilted so that its azimuth angle coincides with solar noon. The angle of elevation of the collector is adjusted for optimum performance through the year, alternatively the collector is adjusted in elevation at several month intervals.

One or two glass covers

Air

Insulation

Aluminum plate
painted black

water
tank
storage

storage
bypass

to
building

pump

from
building

pump
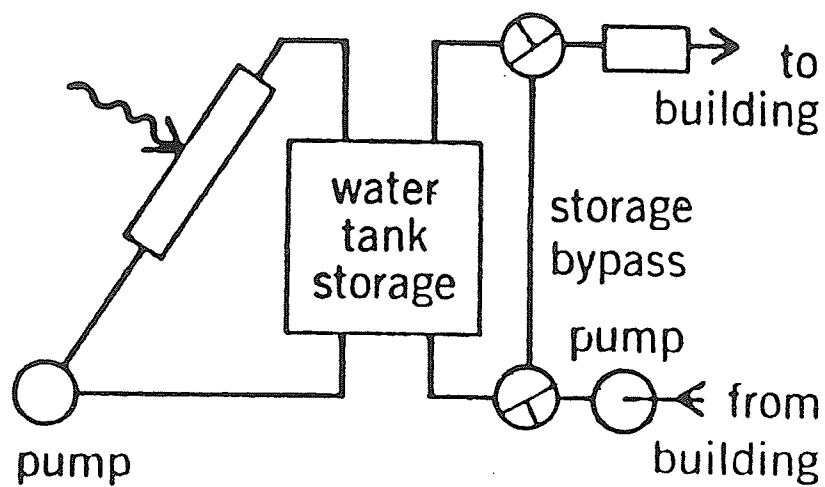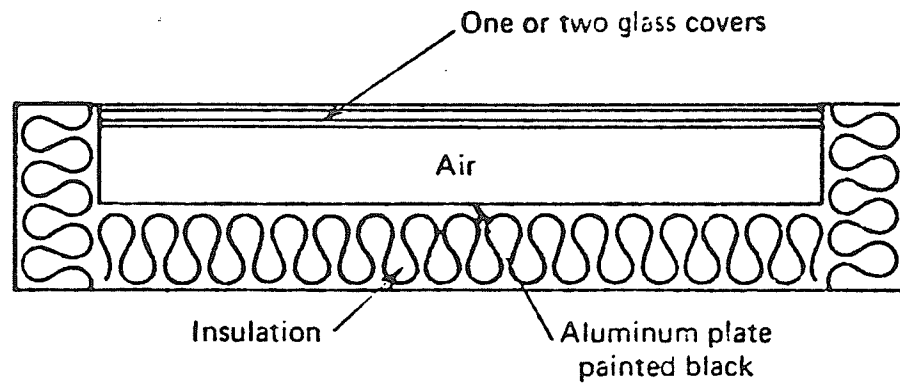
Figure 5.1 Flat plate collector arrangement schematic. The working fluid (water, air) is heated in the collector by sunlight and transferred to a storage or heat exchange unit.

Flat plate collectors operate in bright sunshine or cloudy conditions, which is the major advantage of the collector i.e they make use of both the direct and diffuse components of sunlight. Disadvantages include high cost per unit area of collector and poor efficiency of collecting solar energy, i.e. the ratio of the energy transferred to the medium versus the energy incident. Typically the efficiency with which the incident solar energy is transferred to thermal energy of the circulating fluid is 10%.

5.2.2 Photovoltaic Collectors

Photovoltaic collectors or solar cells convert solar energy directly into electrical energy by generating electron-hole pairs in the junction region in semiconductors. Suitable semiconductors will have a work function which is of the same order as the energy contained in the quanta of light, examples are Silicon or Gallium Arsenide. First used to provide electrical power in space, solar cells were considered to be too expensive for terrestrial power generation on a large scale, since they needed to be produced in pure single crystal form. However with the development of amorphous cells, with advances in the technology of production [28] and with the development of cells designed to be placed at the focus of a fresnel lens, solar cells are currently the most actively pursued form of solar energy conversion.

In a non-tracking arrangement the solar cell panel is aligned in the same way as a flat plate collector, to receive the maximum amount of solar energy possible through the year for that orientation. The output from both photovoltaic panels and flat plate collectors can be augmented by using low cost side reflectors which reflect more incident solar energy onto the panel.

5.3 Focussing Collectors

In order to design highly efficient solar thermal energy conversion devices the intensity of sunlight needs to be concentrated many times over the incident intensity reaching the surface of the earth. There are 5 ways to accomplish this as described below.

5.3.1 Fresnel Lenses

Fresnel lenses consist of sheets of plastic which have been moulded so that their surface consists of many light refracting facets. Very high concentration ratios are possible with such lenses. The lenses suffer from the disadvantage that they are available only in relatively small diameters, hence the power delivered to the focal plane is correspondingly small.

5.3.2 Parabolic Troughs

Troughs consist of a reflecting mirror surface, parabolic in cross section, which extends the length of the collector as shown in figure 5.2. The focus produced lies along a line and therefore the geometry lends itself to perform the heating of a liquid flowing through a tube placed along the line focus. The advantage of the system is that the required tracking (see section 5.3.6) needs only be performed on one axis. The disadvantage of this and other focussing type collectors is that they only concentrate the direct component of the incident sunlight, their use is therefore limited to areas which have a large number of clear days throughout the year.
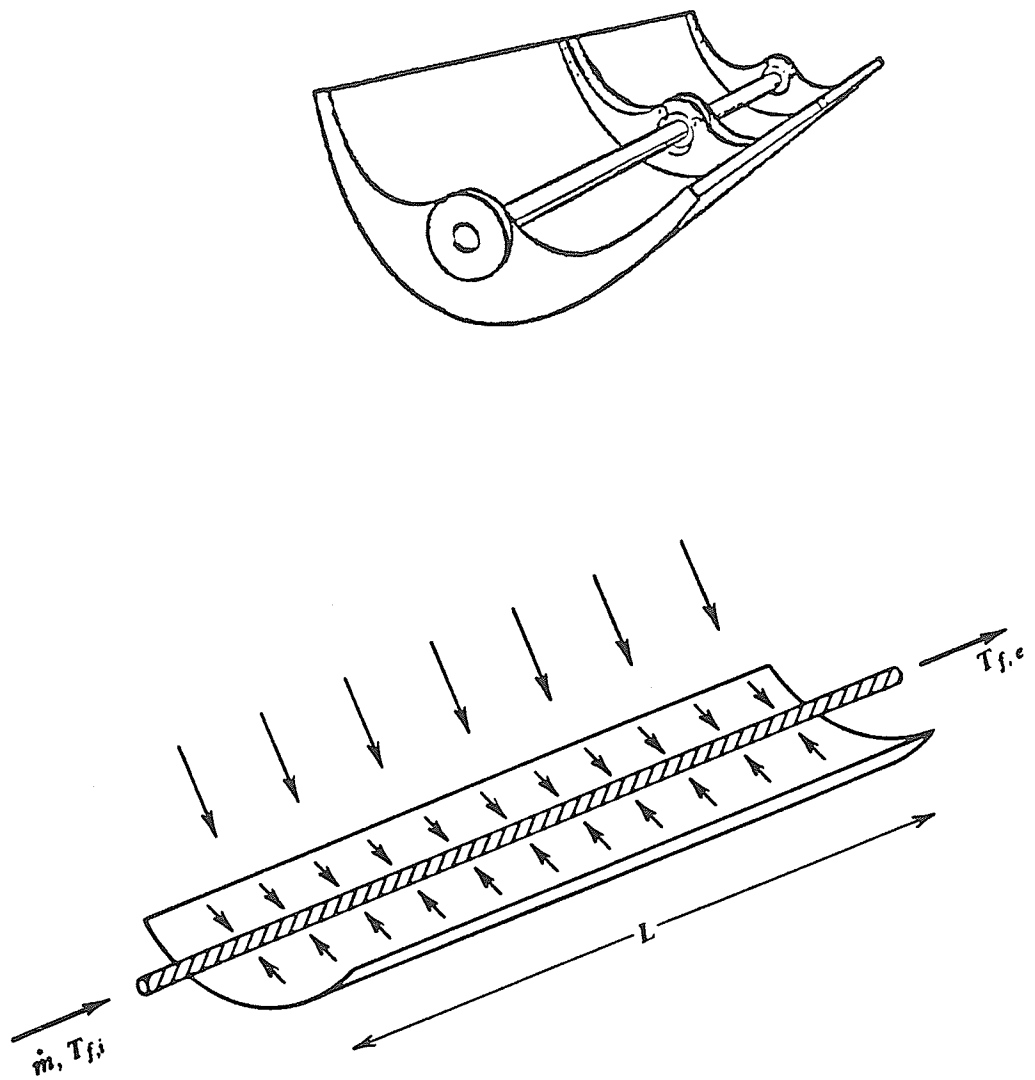
Figure 5.2 Parabolic trough type collector. A liquid is heated as it passes through a tube placed along the line focus of this focussing type device.

5.3.3 Parabolic Dish Concentrators

By mounting a parabolic mirror on a tracking arrangement, concentrations of the order of several thousand of the incident solar energy can be produced at the focus. Figure 5.3 shows a typical arrangement of an elevation-over-azimuth mounted mirror.

A receiver placed at the focus of the mirror converts the incident solar energy into a more transportable form by producing steam for example or by using the incident energy to drive Stirling or Rankine Cycle engines which then drive a generator to produce electricity [29,30].

Both the parabolic mirror and trough can be used to form a "distributed" collector system where a number of units can be used to meet the required load.

5.3.4 Central Receiver System

In the central receiver system a field of sun tracking flat mirrors reflects the sunlight to a single target receiver. The receiver is usually mounted on a tower in the center of the heliostat field. This system has the advantage that only a single large receiver is involved, however the power output from the facility is fixed at the outset since the receiver is designed to accept the power of the heliostat field. An example of the central receiver concept is that at Barstow California, steam is generated in the receiver and used to drive a turbine which produces 10 MW of electricity.

parabolic
mirror
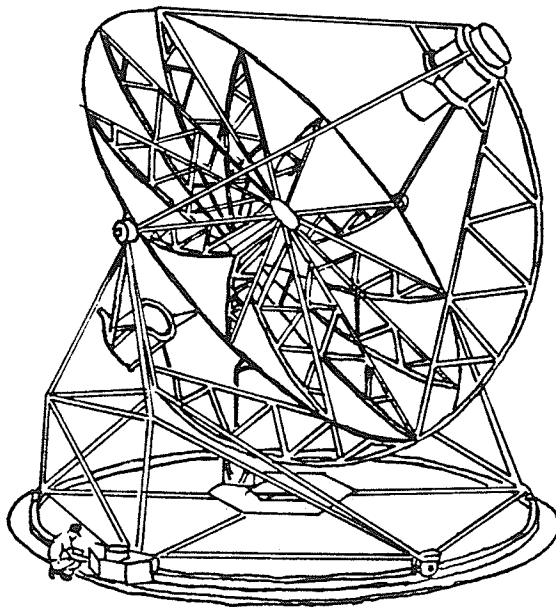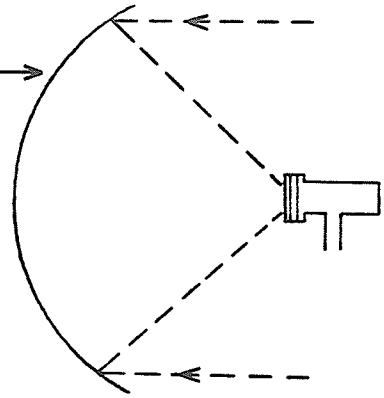
Figure 5.3 Concentrating parabolic mirror mounted on an elevation over azimuth mount.

5.3.5 Heliostat - Concentrator

Also known as a solar furnace, this arrangement consists of a sun tracking heliostat flat mirror which reflects sunlight into a parabolic concentrating mirror.

The arrangement has the advantage that the focus of the parabolic mirror is relatively fixed in space and is therefore very useful for the testing of prototype solar energy conversion devices.

5.3.6 Tracking Schemes

In order for focussing devices to perform throughout the day, the mirror surface must be mounted on an arrangement which tracks the apparent motion of the sun through the sky.

There are two basic forms of sun tracking arrangements. The first is the elevation over azimuth mount. In this arrangement two axes are motorized and drive the collector in the local solar co-ordinates described in chapter 3. The elevation and azimuth angles are given by:

$$Z = \cos^{-1}\left(\cos D' \cos(90 - L) + \sin D' \sin(90 - L) \cos H\right) \qquad (5.1)$$

$$A = \tan^{-1}\left(\frac{\sin D' \sin H}{\sin D' \cos(90 - L) \cos H - \cos D' \sin(90 - L)}\right) \qquad (5.2)$$

A computer could calculate the position of the sun on a particular day and drive the sun tracking device or heliostat to the required position. Such "sun pointing programs" are in widespread use. [31]

Alternatively a sensor, limited in view angle, similar to a normal incidence

pyrheliometer, can be mounted on the heliostat and its output connected to elevation and azimuth drive motors in such a way that the output from the sensor is kept at a maximum. A disadvantage of this arrangement is that if there is an extended period of cloud cover during which the heliostat is not tracking, then the tracking sensor may not be able to recover after the cloud has passed, i.e. the sun may have moved out of the field of view of the sensor.

The second method of tracking is known as the equatorial mount. In this arrangement only one drive motor is used to drive the collector about an axis that is parallel to the axis of the Earth. In this way any point on the collector moves on a plane parallel to the equator. The speed of the drive motor can be set such that one revolution about the axis is performed every 24 hours. As the declination of the earth changes, small changes need to be made to the tracking arrangement to compensate. These are necessary typically every few days.

5.4   Conclusions

The type of collector system built at the University of Manitoba was dictated by two requirements, the first was the production of as high a concentrated intensity as possible. The second requirement was that the power contained in the focal region should be large enough so that small prototype energy conversion devices, which would exhibit all the characteristics of the larger working devices could be built. These characteristics would be, for example, energy losses due to re-radiation and converter maintainance problems such as fogging of windows, cracking of seals etc.

These basic requirements require collectors which employ focussing in their

56

operation. Line focus devices such as "solar troughs" do not meet the criterion of a small area focal region. Single Fresnel lenses, though offering high concentration, provide too small an amount of power in the focal region. Many Fresnel lenses may be mounted on a frame which would be arranged to track the sun, at which point their merits become those of a sun tracking parabolic mirror as discussed below.

The choice of collector system was also influenced by the desire to have a focal region that was stationary. Since the system was to be used for prototype testing, it was envisaged that access to the focal region would be necessary for short periods on an intermittent basis, even while the system was operating. The focus of tracking parabolic mirrors moves with the mirror as it tracks the sun. In order to access the focal region, the system would need to be moved off track, and later moved back into the appropriate orientation. In practice this would take some time if the size of the mirror is appreciable, since to provide the required torque to move a large mirror, the driving motors would need to be geared down many times, consequently the resulting speed of movement would be quite slow.

At this point there were two collector systems which could meet the requirements. These were the solar tower or central receiver concept and the heliostat concentrator arrangement. The desired concentration ratio was to be of the order of several thousand. Consider a solar tower arrangement with each heliostat containing ten mirrors, with each mirror providing some focussing, for example 5 times concentration of the incident beam. If all the mirrors are aligned so that their reflected beams strike a single target area, then to achieve a concentration of 2000 times, 40 heliostats would be required. The solar tower concept was therefore discounted on the basis of cost alone. The heliostat concentrator arrangement can provide the required

power while providing higher concentrations that the solar tower concept.

It was envisaged that after prototype development was complete the production converter would be used with a single sun tracking parabolic dish system. In this way the power requirement could be met by increasing the number of dish systems used. If the required energy should increase then more dishes could be added. In this case of the power tower concept the power output has to be specified at the outset of the design phase.

It was therefore decided that a heliostat concentrator system would be built at the University of Manitoba. The details of the mechanical and electrical construction are presented in the next chapter.

Chapter 6

The Construction of a Solar Energy Concentrator System

6.1 Introduction

In order to study new and potentially highly efficient solar energy conversion devices a facility for concentrating the intensity of sunlight was constructed on the roof of the Physics building at the University of Manitoba in Winnipeg. Winnipeg has one of the highest levels of direct radiation of all Canadian cities, levels that compare favourably with areas commonly associated with the United States "sunbelt" such as parts of California and Texas. Winnipeg is therefore an ideal location for a focussing type solar collector system.

A survey of collector and concentrator systems led to the choice of a heliostat concentrator configuration which met the design criteria of being able to provide highly focussed beams of sunlight in a stationary focal region and which could deliver several kilowatts of power to the focal region.

In the course of designing the system, it was noticed that a satellite dish

pressed from a single piece of stainless steel had a high surface quality. The diameter of the dish (2.3 m) was such that it could deliver the required power to the focus. The size of the dish was such that its mounting was within the capabilities of the Department of Physics mechanical shop. Further the construction cost of a suitable heliostat, tracking equipment, alignment equipment and control electronics was within the financial resources of the Department of Physics for a project of this size.

If one assumes a direct intensity of 800 W/m^2 incident on the concentrating mirror and further assumes that its reflectivity is 90% then the power delivered to the focus will be approximately 3000 W. Practical energy conversion systems based on tracking parabolic mirrors would deliver of the order of 30 kW. The system can therefore be regarded as providing the energy input for 1/10 th scale, research energy conversion prototypes.

The facility is the only one of its kind in Canada and the only one in North America in a northern location, i.e away from the "sunbelt" regions, it was constructed and calibrated over the period June 1981-August 1985.

The mechanical and electrical details of the construction, alignment and operation of the facility are described in this chapter.

6.2   Mechanical Details

The layout of the solar concentrator is shown in schematic form in figure 6.1. The facility was built on a fenced off section of the roof of the 5 storey Physics building.
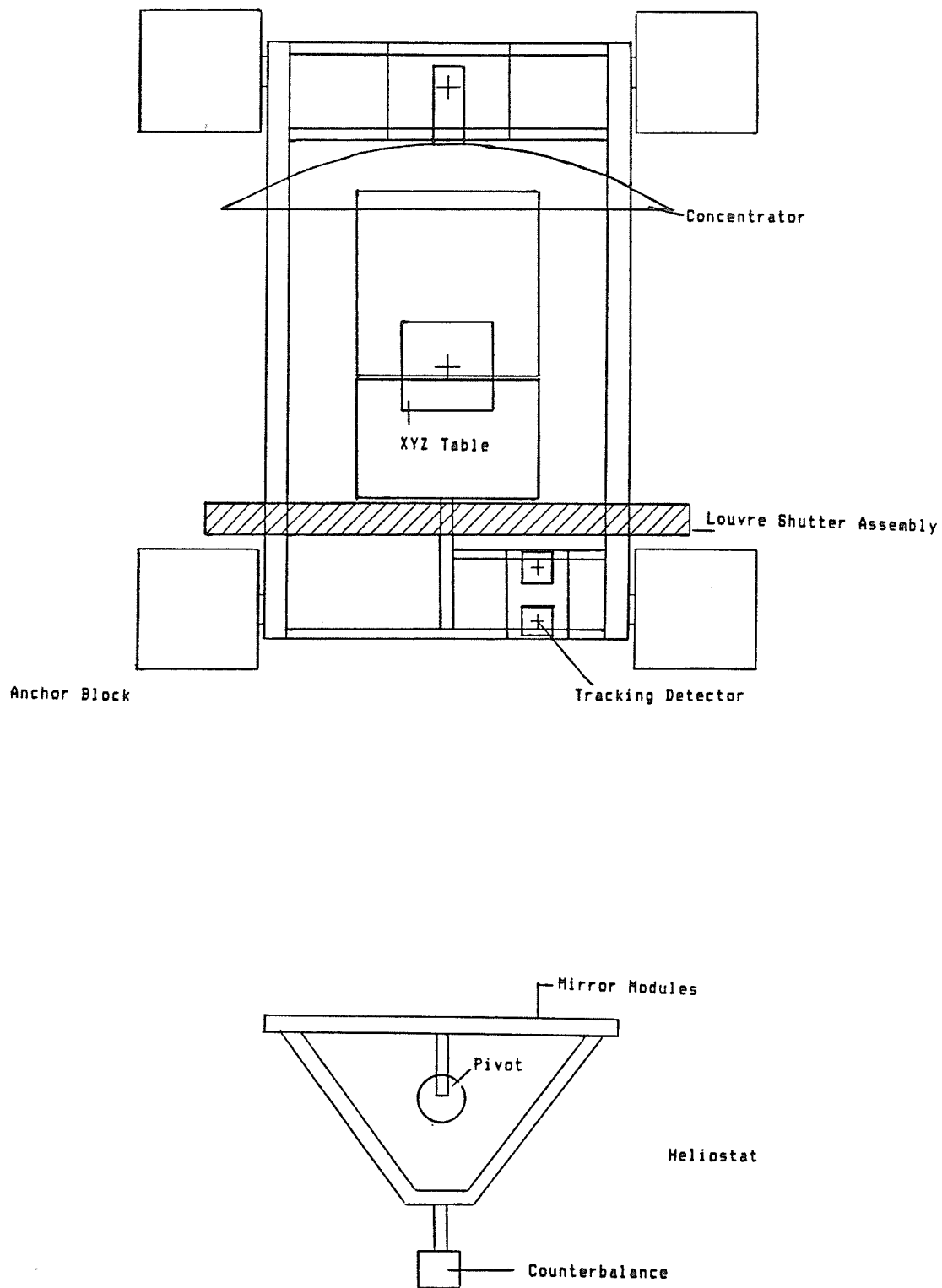
Figure 6.1 Schematic diagram of the heliostat - concentrator type arrangement constructed at the University of Manitoba.

6.2.1 Heliostat

The heliostat consists of an array of 6 plane mirror "modules" attached to a frame, and mounted on an elevation over azimuth tracking arrangement as shown in figure 6.2. Each mirror module is 3ft by 3ft (0.9 m) so that the overall heliostat surface is 9ft (2.7 m) high by 6ft (1.8 m) wide

Mirror Modules

The construction of the mirror modules is based on the "second generation"heliostat mirror modules developed for the Barstow California, Central Receiver facility [32]. To fabricate a mirror module, a sheet of back silvered float glass, 3mm thick, is placed in a sandwich arrangement to reduce distortions. The mirror rests on a 1 inch thick sheet of polystyrene foam which in turn rests on a 3mm sheet of aluminium, as shown in figure 6.3. The aluminium sheet is attached to a base frame which has an X-shaped cross member for support. No adhesive is used in the construction so that the mirror is not subject to stresses caused by differential contraction. The whole sandwich is held together by L-shaped clamps which are attached to the base frame via a screw in a slotted hole. A rubber "O" ring fits between the L-shaped clamp and the mirror surface. The sandwich is laid out horizontally and the screws tightened. Over the period since the heliostat was built, the mirror modules have survived ambient temperature excursions of -40°C to +30°C, hail and winds in excess of 100km/hour without damage.

Heliostat Mount

The heliostat frame is mounted on a pivot using counterbalancing weights. This allowed for the use of smaller driving motors than would have otherwise
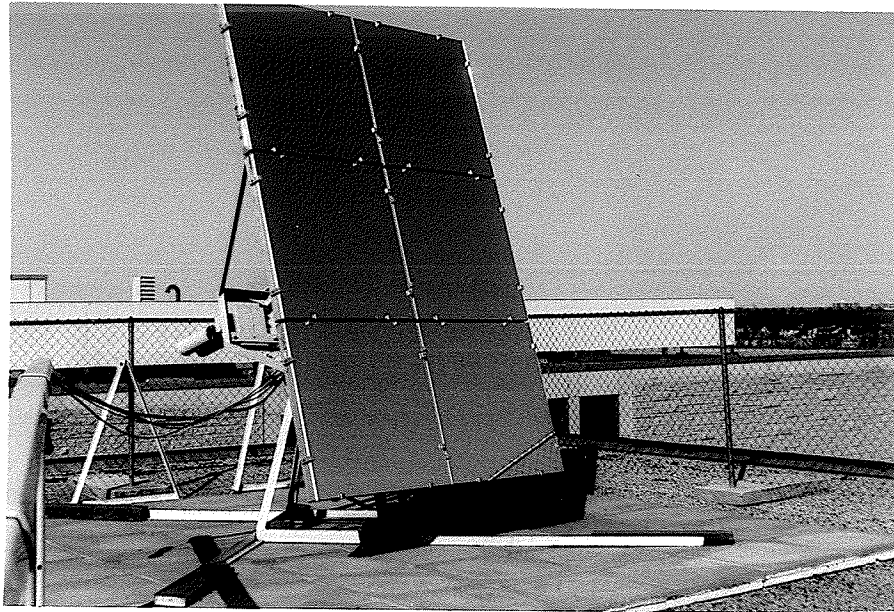
Figure 6.2 2.74 m x 1.83 m elevation over azimuth mounted heliostat at University of Manitoba.

O ring

3mm float glass

polystyrene foam

aluminium plate

base frame
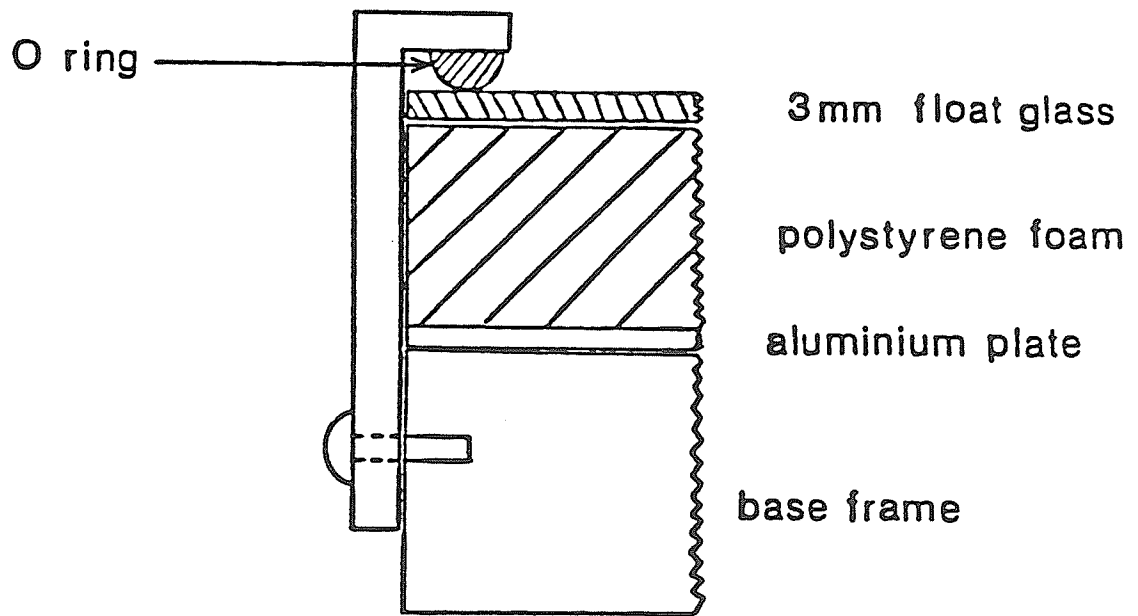
Figure 6.3 Heliostat mirror module construction.

been necessary for the elevation drive.

Stepper motors are used to drive the heliostat in elevation and azimuth. The output of the azimuth drive motor is geared down in the ratio 72:1 by a gearbox unit, and a further 100:1 by the main gear attached to the heliostat. When running constantly the stepper motor rotates at 100 r.p.m and the heliostat turns through 0.013 r.p.m or 5.0 minutes of arc per second.

The elevation drive uses a 50:1 gear ratio after the 72:1 gearbox resulting in a constant elevation angle driving rate of 10.0 minutes of arc per second.

The original size of the heliostat front surface was 9ft by 9ft. An unfortunate consequence of the counterbalance design was that the heliostat would oscillate in windy conditions, the resultant movement of the focal "spot" of the concentrator was unacceptable. Consequently the heliostat size was reduced to 9ft vertical by 6ft and air filled dampers attached between the frame and the pedestal in order to minimize the oscillations.

6.2.2 Concentrator Arrangement

To fix the concentrating mirror firmly in place it was bolted to a pedestal which was in turn bolted to a frame constructed from 4 inch wide steel "I" beam. To hold the frame firmly, large concrete anchoring blocks were poured. Each block has a 2 ft by 2 ft base, is 1ft deep and weighs 560 lb. As the blocks were being poured 1 inch steel plates were set in each of them (figure 6.4) the plates extended 6.25 inches outside and 18.0 inches inside the blocks. The frame was then levelled and bolted to these plates. This formed a rigid structure that would withstand the considerable wind loading that occurred occasionally on the roof of the building.

The parabolic mirror was made by coating a 90 inch (2.3 m) diameter

64
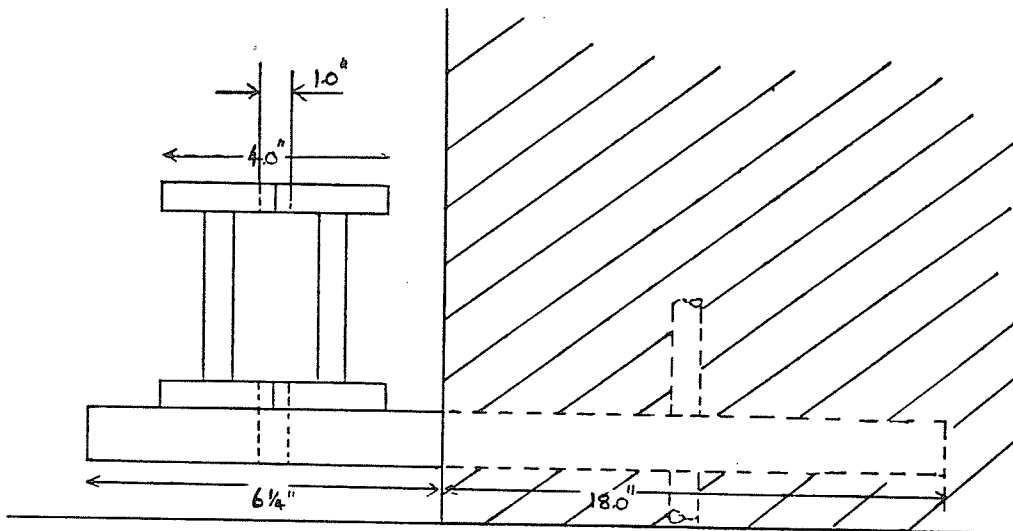
Figure 6.4 Concentrator anchor details. The base frame which holds the concentrating mirror assembly is bolted to 1 inch steel plates set in concrete.

microwave dish with ECP91A, an aluminized polycarbonate film. The microwave dish was fabricated from a sheet of stainless steel with a single welded seam, and was pressed into the required shape. The focal length of the dish is 36 inches (0.9 m). The ECP91A film is manufactured by 3M corporation for solar energy applications, its spectral reflectance is constant over the entire solar spectrum (figure 6.5) [33]. To coat the mirror, triangular strips 22 inches in length with an approximate apex angle of 10° were cut from the film. The film has an adhesive backing that is activated on contact with water. A second set of strips was cut to coat the dish from 22 to 45 inches radius. Air bubbles trapped under the film as it was fixed to the dish were removed, as much as possible, using a printers' brayer. The edge of each strip was made to overlap slightly with the previous strip so as to cover the entire dish.

The result was a parabolic concentrating mirror well suited for solar energy work but not of such quality that Gaussian optics could be employed to predict the focal plane intensity profile (see chapter 8).

A louvre type set of shutters was constructed so that the solar power incident on the concentrator could be controlled during an experiment or removed completely to access the focal plane area. The louvre shutters are shown in figure 6.6.

6.3   Alignment

Before the heliostat and concentrator assembly were moved into position a line was marked out on the roof of the building which would be parallel to the "optical axis" of the system. Fluorescent marker pins were sunk into the roof at intervals along the line. In the process of installing the heliostat, the
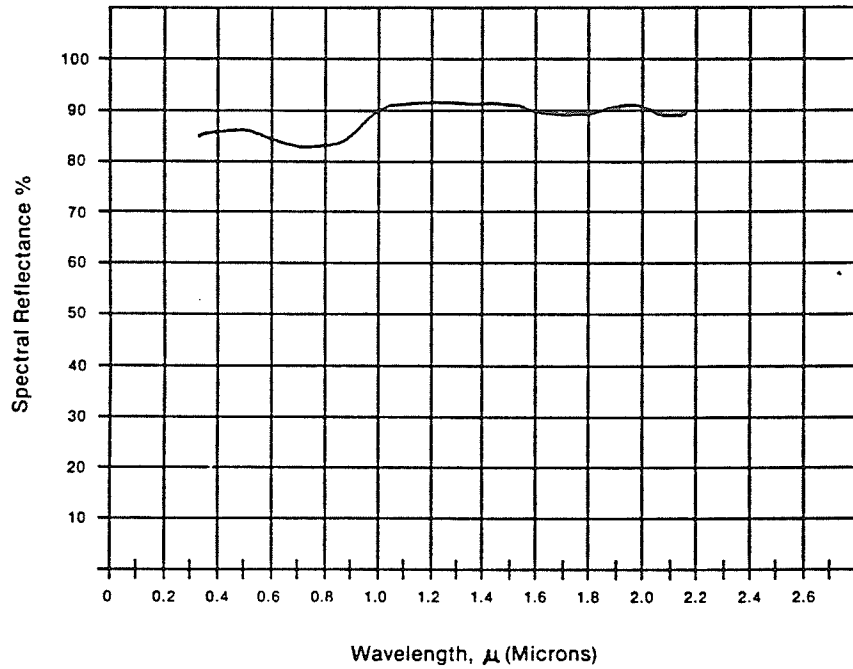
Figure 6.5 Spectral reflectance of ECP-91A [33]. The reflectivity of the ECP91A aluminized polycarbonate film used to cover the parabolic dish, has a minimum of 85% across the solar spectrum.
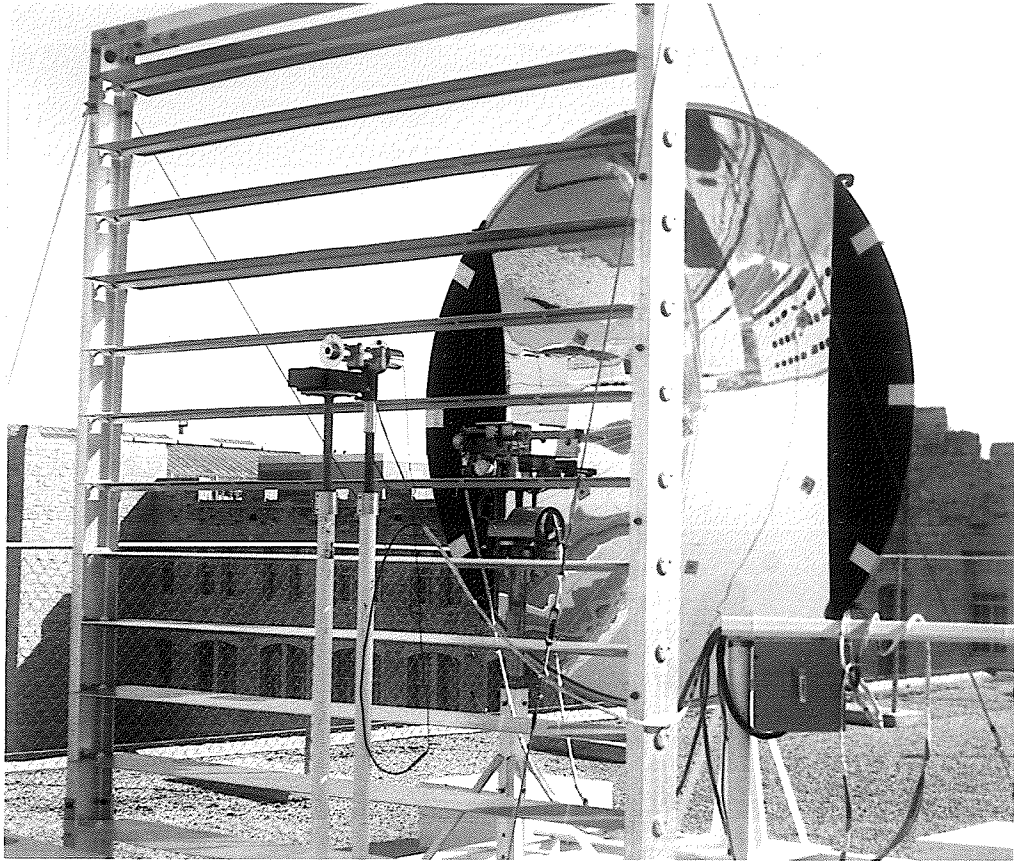
Figure 6.6 Louvre shutter and concentrator assembly. The louvre shutters serve to control or eliminate the illumination of the concentrator by the heliostat.

vertical axis of a theodolite was mounted directly above one of the pins, the azimuth movement of the theodolite was rotated and fixed in a position such that, as the elevation of the theodolite telescope was varied successive pins along the line would come into view. The heliostat pivot was placed into position so that its center was in the plane defined above.

A similar technique was used to align the frame of the concentrator assembly. The centers of the front edge and rear edge of the frame were scribed, the frame was then positioned such that as the theodolite telescope elevation was varied, the front scribe mark and then the rear scribe mark appeared on the vertical axis cross hairs of the telescope. The frame was held against the steel plates protruding from the anchor blocks using clamps until the alignment was completed. After alignment, a hole was drilled through the frame, where it would be bolted to the steel plates. The frame was then made level with metal shims and bolted to the steel plates.

As the concentrating mirror was moved into place its center was positioned to be in the plane of the optical axis in the same way as described above for the heliostat. Having fixed the center of the mirror at zero degrees azimuth, the theodolite telescope was rotated in azimuth and an edge of the mirror located on the cross hairs, the deviation from 0 degrees azimuth was recorded. The cross hairs were then located on the opposite edge of the mirror. The mirror was adjusted in azimuth until the deviation from zero degrees was equal for each side of the mirror. A plumb bob was used to ensure the top and bottom edges of the mirror lay it in the vertical plane by adding small metal shims between the pedestal and the bracket holding an aluminum ring to which the concentrator was attached. Finally all the bolts on the concentrator pedestal and support ring were tightened and the final alignment checked again using the theodolite.

6.3.1 Relative Heights of Heliostat and Concentrator

The maximum variation in the elevation of the sun at solar noon for a particular latitude L is given by:

$$\varepsilon = (90 \pm \beta - \text{L}) \qquad (6.1)$$

Where β is the angle of the earth's axis with respect to the perpendicular to the ecliptic plane and has a constant value of 23.5° and L is the latitude of the site. In Winnipeg (latitude 43° 55') the highest elevation reached by the sun is 63.5° at solar noon on June 21st, the longest day. The lowest elevation is 16.5° reached on December 21st. As the declination of the earth changes throughout the year the elevation at solar noon varies accordingly, however for determining the relative heights of the components of the system only the extremes are required. The heliostat surface is offset from the pivot by an arm of length 22 inches (0.56 m) (figure 6.7). On June 21st at solar noon the obliquity effect reduces the vertical dimension of the area illuminated by the heliostat to

$$y_{\text{Summer}} = \text{L}_1 \cos \frac{63.5}{2} = 7.6\,\text{ft} = 2.3\,\text{m} \qquad (6.2)$$

Where L_1, the length of the heliostat surface is 9 ft. (2.74m). The dimension illuminated at solar noon is centered on a height $h_1 = 71.58$ inches (1.82m)

On the shortest day the elevation at solar noon is 16.5 degrees and the vertical dimension illuminated is now:

$$y_{\text{Winter}} = \text{L}_1 \cos \frac{16.5}{2} = 8.9\,\text{ft} = 2.7\,\text{m} \qquad (6.3)$$

70
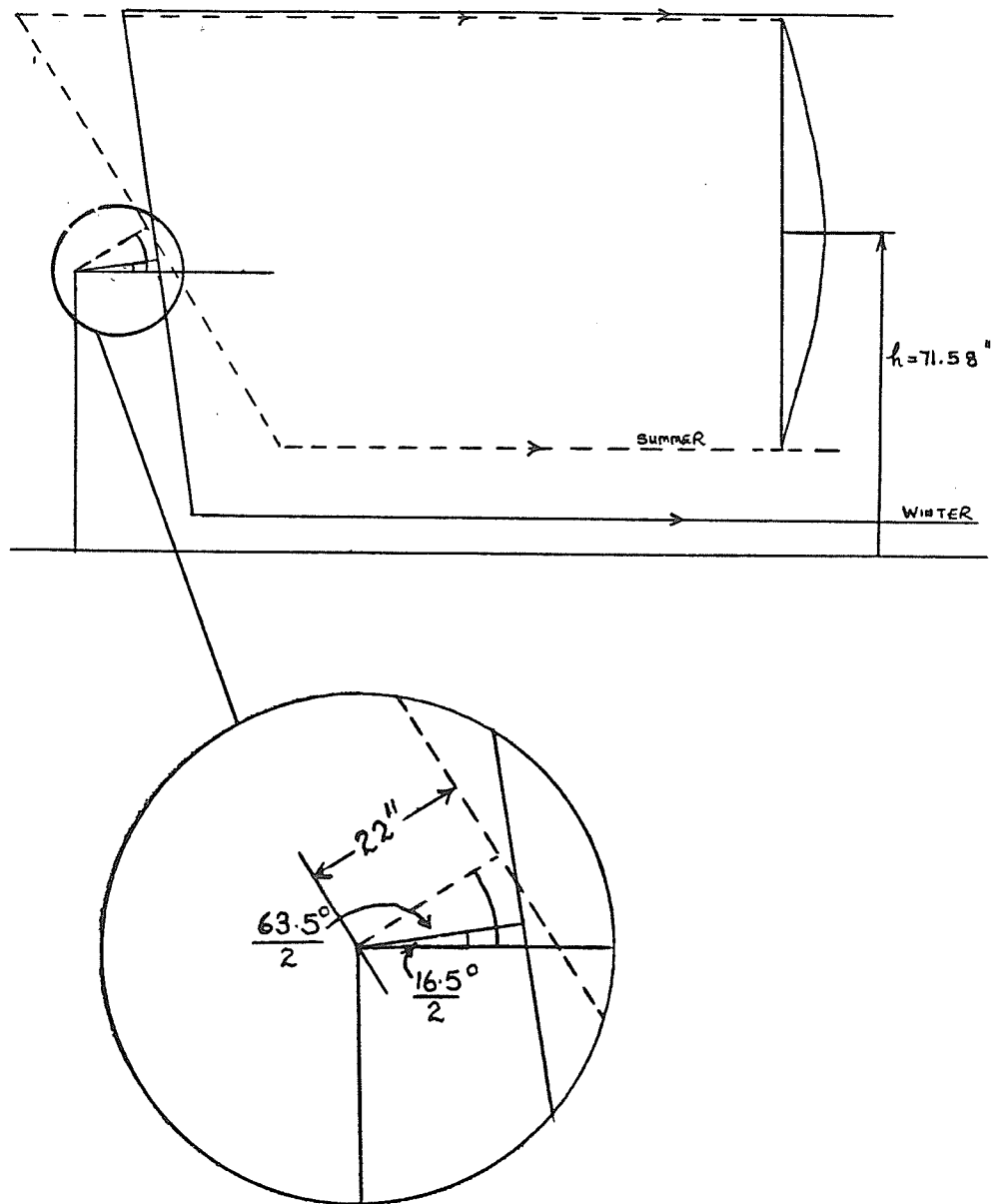
Figure 6.7 Relative heights of heliostat and concentrator for maximum illumination throughout the year. The height of the concentrator is adjusted such that it is fully illuminated in the vertical dimension throughout the year.

71

In this case the illuminated dimension is centered at a height $h_2 = 63.2$ inches (1.6 m).

It is desirable to illuminate the vertical dimension of the mirror fully in both these cases. One must locate the mirror in the overlap of the two dimensions above, assuming the mirror dimension is less than the overlap. If the height of the pivot of the heliostat is set at 60.0 inches and the height of the center of the concentrating mirror is set to 71.6 inches then the concentrating mirror can be illuminated fully in the vertical dimension throughout the major part of any day of the year.

6.3.2   XYZ Positioning Table

For accurate measurement of the variation of focal plane intensity with position, a three axis positioning table was designed and constructed in the department of Physics, and is shown in figure 6.8. The table can move independently on any of three mutually perpendicular axes. Precision linear encoders allow the position of the table to be read with an accuracy of 0.1 mm (0.004 inches). The range of motorized travel is 7 inches (17.8 cm) in the Y (up-down direction), 6.5 inches (16.51 cm) in the X (side-to-side) direction and 4 inches (10.16 cm) in the Z (forward back) direction. Set screws allow the height to be changed manually through approximately 18 inches (45 cm). The two horizontal (X and Z) planes are each mounted on two linear bearings and driven by a feed screw arrangement geared down to a small d.c. motor. The vertical movement section is mounted on a large threaded rod and supported by three linear bearings. An a.c motor is geared down to drive the table in this direction.

A device mounted on the table can be moved into position at a speed of
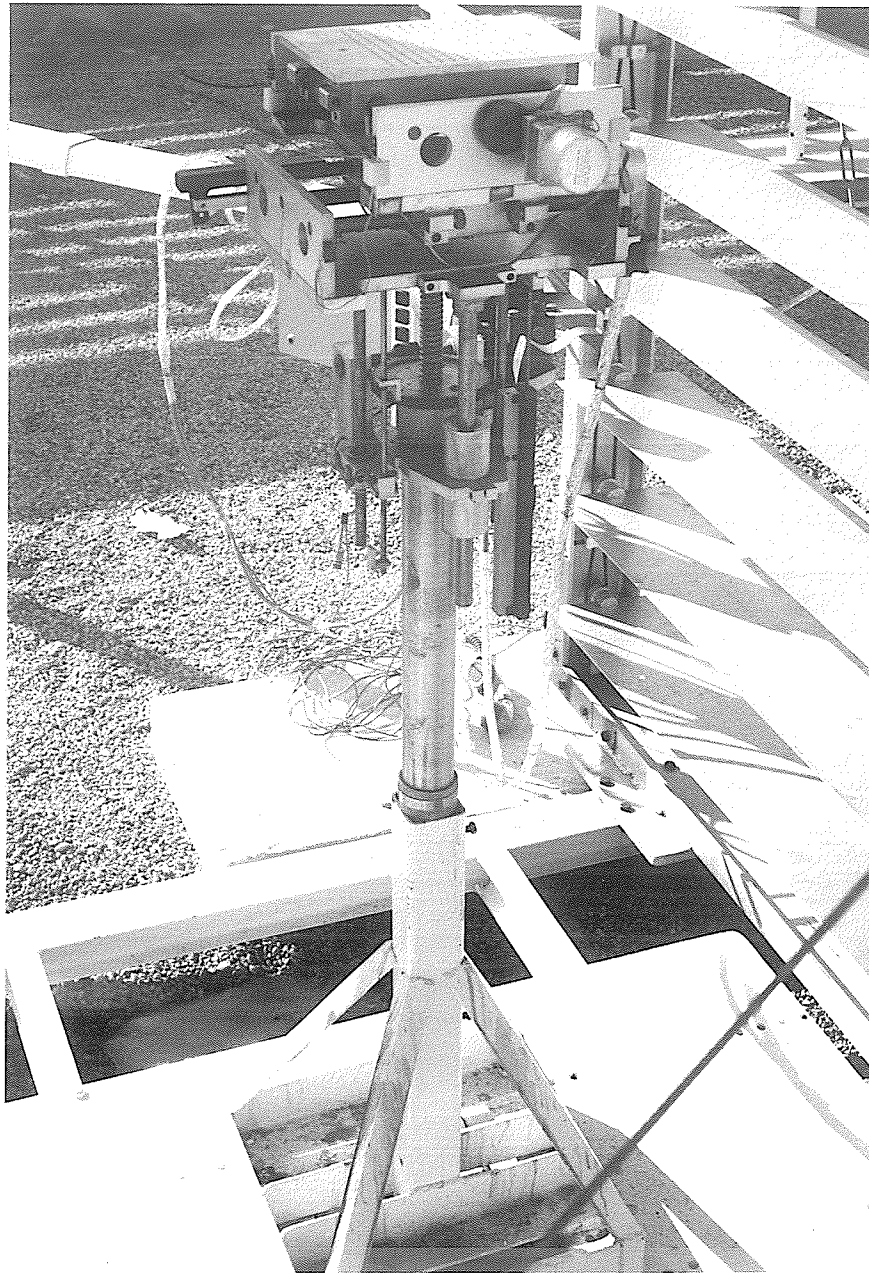
Figure 6.8 Three axis xyz positioning table used to accurately determine the focal plane intensity distribution when used in conjunction with a suitable radiometer.

approximately 0.5mm/sec in Y and Z directions. The X direction was to be used for the scanning of the focal plane intensity and its movement was therefore made faster. (6 mm/sec)

To calibrate the position of the table a regulated voltage was applied to the precision linear potentiometer. The displacement versus voltage was measured using vernier calipers and a 6-1/2 digit digital voltmeter. A least squares fit was performed on the data recorded.

During manual positioning of the table, the voltage from each axis is read by a digital voltmeter and its position determined from a look up table. During the focal plane intensity mappings, the output from each axis was connected to an analogue to digital converter through an eight channel multiplexer mounted in an IBM PC computer, the voltage was recorded by the computer and the position calculated. The intensity mapping process is described in chapter 7.

Each direction of movement has limit switches at the ends of travel which turn off the driving motors when activated. The drives and position encoders are thus protected in the event of a hardware/software error.

6.3.3   Tracking Arrangement

An optical closed-loop feedback system is used to keep the heliostat reflecting sunlight into the concentrating mirror. It is shown schematically in figure 6.9. Two pairs of photocells are mounted in a view limiting enclosure which is mounted at the front of the concentrator assembly. The sensor field of view contains a single mirror module on the heliostat (the left center module). To bring the heliostat on track, the heliostat is driven into approximate position by manual control of the drive motors. The heliostat drive control unit is
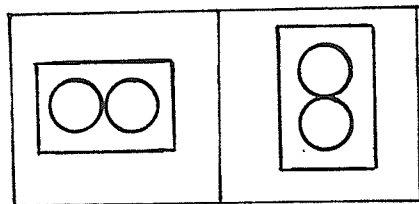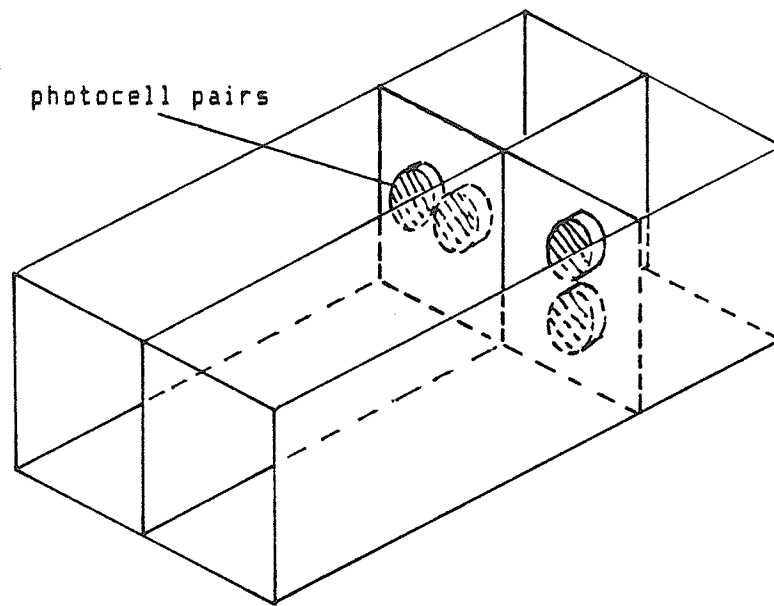
photocell pairs

Figure 6.9 Tracking sensor schematic. Two pairs of photocells are illuminated by the heliostat. If one cell of a pair is illuminated more than the other, a signal is sent to the heliostat motor control unit. The motor control unit then drives the heliostat to compensate so that both cells are equally illuminated. In this way heliostat tracking is accomplished.

next switched to automatic and the drive motors are controlled by the sensor.

One of the pairs of photocells in the sensor is mounted vertically, the other horizontally. If one of a pair of photocells is illuminated more than the other a difference signal is output which activates the appropriate heliostat drive motor.

To give the required sensitivity in tracking, the depth at which the photocells are mounted within the sensor can be varied, thus changing the view angle of the sensor. A welding glass filter is placed over the end of the sensor to screen out diffuse light.

The stepper motors on the heliostat do not run constantly when the heliostat is tracking but rather pulse intermittently. Each motor requires 200 pulses to complete one revolution of the motor shaft. Each pulse to the azimuth drive motor represents a rotation of the heliostat by 0.015 minutes of arc. In practice the azimuth drive motor receives a train of pulses approximately every 2 seconds from the sensor to keep the heliostat on track.

6.3.4   Tracking Sensor Alignment

It was realized that the alignment of the tracking sensor would be crucial to the resulting intensity at the focal plane of the mirror. The smallest spot size, and hence the maximum intensity will result when the incident rays are parallel to the optical axis of the system To optimize the alignment of the sensor a radiometer was placed on the XYZ table at the focus of the mirror. The sensor was mounted on a spectrometer table mount with the axis of the sensor parallel to the centre line of the heliostat concentrator system.

The spectrometer table mount was aligned in the horizontal plane using a

76

precision spirit level. As described above, the top and bottom edges of the concentrating mirror were aligned using a plumb bob so that they lay in the vertical plane.

Given this initial alignment, the sensor was moved in azimuth through a small angle, typically on the order of one degree. The radiometer was moved through the focal plane and a new maximum intensity found. This procedure was repeated for sensor positions at several azimuthal angles either side of the zero determined as described above. The sensor was finally fixed at the azimuthal angle which gave the highest intensity reading from the radiometer.

A normal incidence pyrheliometer was mounted on top of the sensor arrangement to give an absolute reading of the radiation incident on the concentrator (figure 6.10). In this way the variation in reflectivity of the heliostat, dependent on the time since its last cleaning was removed from the measurements.

During periods of intermittent dense cloud cover, the heliostat control system would switch off. The system could recover from approximately 15 minutes of cloud cover. If the period was longer the heliostat would have to be brought back on track manually. The system would remain on track during extended periods of thin cloud cover. It was found that the tracking system would operate under conditions where the direct component of the incident sunlight was reduced by cloud cover to 213 W/m^2, a typical value for direct radiation at that time being 700 W/m^2

Limit switches were mounted at the extremes of movement in the elevation direction of the heliostat to stop movement in the event of an error in the control system.
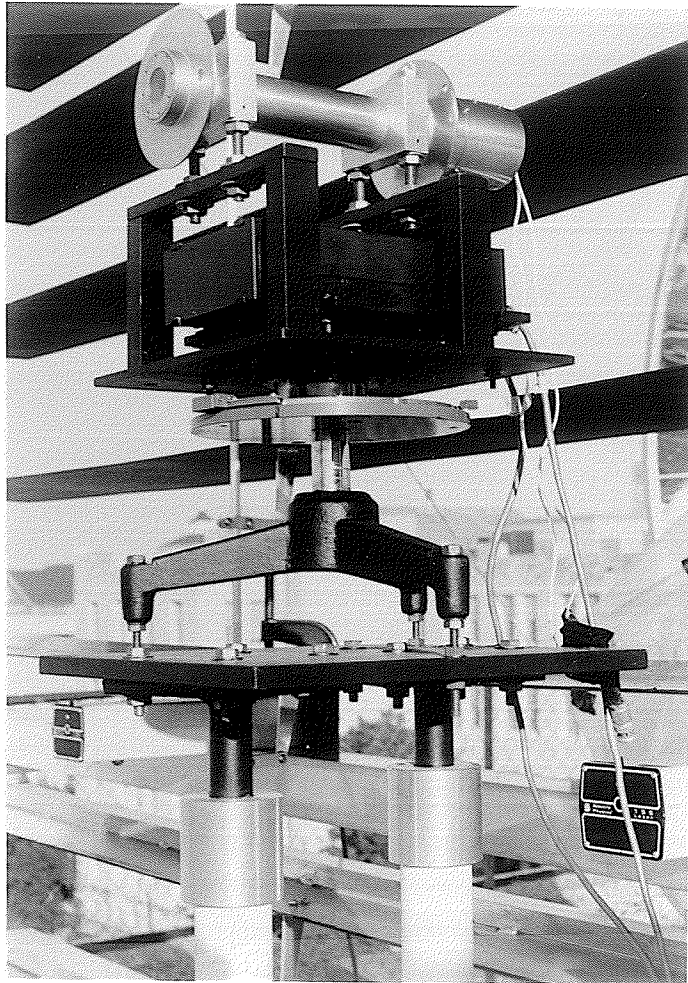
Figure 6.10 Tracking sensor and dish incident intensity normal incidence pyrheliometer. The alignment of the tracking sensor and the intensity incident on the concentrator are critical in the operation of the system. Both devices are mounted on a spectrometer table for accurate alignment.

6.3.5 Insolation Recording Station

To complete the data recorded from the solar concentrator system a station was installed nearby to measure the direct and diffuse component of the incident sunlight. This data, when accumulated over a number of years will help determine the suitability of the site for large scale solar collectors. The ratio of direct to diffuse radiation will determine the type of solar collector that would be best used.

6.3.6 System Control

All functions of the concentrator system can be remotely controlled from a control area. After initial alignment the heliostat tracking is automatic. Transducers are used to give readouts of heliostat elevation and azimuth, positioning table X, Y and Z positions, normal incidence pyrheliometer readings from the concentrator assembly, Louvre shutter orientation, radiometer output and radiometer housing temperature and direct and diffuse insolation readings.

6.4 Conclusions

The facility described above was constructed over the year 1982-83. The reduction in size of the heliostat reduced the power delivered to the focus. This amount of power would also change during the course of the day as different amounts of the area of the concentrator were illuminated due to the obliquity effect. In order to determine the amount of power delivered to the focus the focal plane intensity mapping described in the following chapter was performed.

Chapter 7

Intensity Mapping of the Concentrator Focal Plane

7.1 Introduction

In order to better understand the performance of the heliostat concentrator system as related to the design criteria of high concentration ratio and reasonable power, an intensity versus position mapping of the focal plane was performed.

The determination of the efficiency of solar energy converters tested with the system will also require focal plane intensity data. This chapter describes how the measurement was performed.

7.2 Radiometer

To measure the intensity at various positions within the focal plane, an electrical compensation type radiometer adapted for measuring high intensities was used. Known as a Kendall radiometer, it consists of a cavity receiver

to which thermopile junctions are attached [34]. The radiometer is shown in schematic form in figure 7.1. Solar radiation enters the cavity through a hole, which is view limited to a ray acceptance angle of 120° i.e rays up to ± 60° off the optical axis are received by the cavity. The walls of the cavity are coated with an optical black material which gives an effective absorptance of 0.992. The value of absorptance is constant over the solar spectrum [35]. As solar energy is incident on the cavity, its temperature increases producing a voltage between the hot and cold junctions of the thermopile. The cold junctions are mounted on an identical cavity within the radiometer, which is not illuminated, both cavities are fixed to the body of the radiometer which consists of a water cooled copper block. Since the illuminated and shielded cavities are identical, changes in the output due to changes in the temperature in the main body of the radiometer are eliminated.

To calibrate the radiometer, the aperture is shielded from incident solar radiation. A calibrating heater, wound around the receiver cavity applies electrical heating (see figure 7.1). When the thermopile output due to electrical heating is equal to that due to solar heating, measured later, then the electrical power applied is equal to the solar power received. The electrical power can be measured easily and accurately. An accurate knowledge of the area of the aperture will then yield the intensity of the incident sunlight in Watts/m². In this way measurements of solar intensities of up to a concentration ratio of 10,000 times may be measured with an accuracy of 1%.
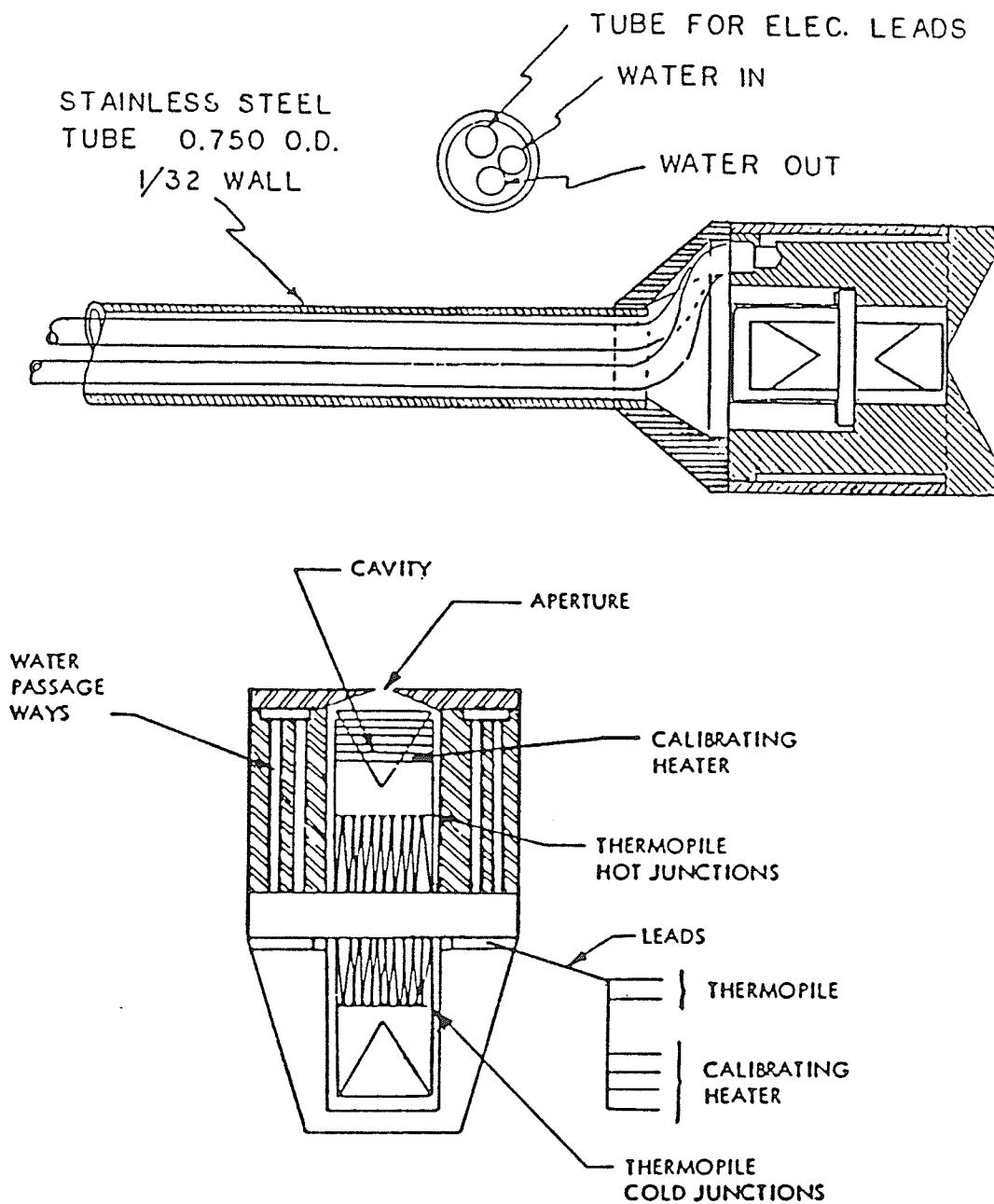
Figure 7.1 Radiometer schematic. A "Kendall" electrical compensation radiometer, especially constructed for the purposes of measuring highly concentrated beams of sunlight is used to perform the focal plane mapping in conjunction with the XYZ table.

82

7.3 Measurement Technique

The radiometer was mounted on the XYZ movement table and the position of maximum intensity along the axis of the system (z direction) found to give the location of the focal plane. Figure 7.2 shows the radiometer mounted on the table. The radiometer was then driven down through a vertical distance (y direction) of 20 mm, and driven in the horizontal (x) direction to a position -37 mm. This formed the starting location for the mapping. The radiometer was then scanned from -37 mm to +37 mm in the x direction and readings taken of the intensity. The y position of the radiometer was then incremented by 3 mm and the scanning process repeated until scans had been performed for extremes of y of ±20 mm from the optical axis.

The voltage output from the radiometer, the three linear position encoders, and the incident intensity on the concentrator, i.e the amount of sunlight reflected by the heliostat, were measured by an 8 channel analogue to digital converter mounted inside an IBM PC microcomputer. Before each scan the initial y and z positions and the incident intensity were recorded. As the scan took place the outputs from the radiometer and x position were alternately measured at a sampling rate of 10 readings per second. The radiometer moves through the focal plane in x at a speed of 6.5 mm/sec giving a position reading every 0.65 mm. Data for x,y,and z positions, incident intensity on the concentrator and focal plane intensity were written to disk at the end of each scan for analysis.
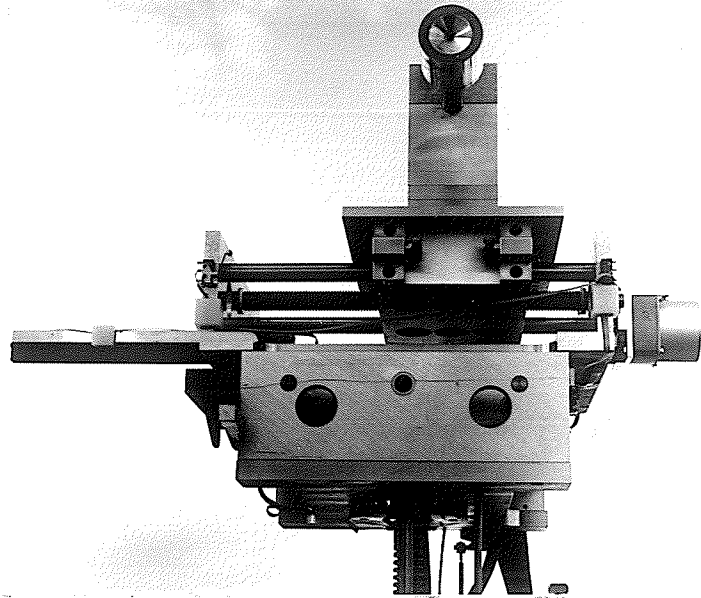
Figure 7.2 Radiometer mounted on positioning table.

7.4 Analysis

The radiometer has a 1/e response time of 1.84 seconds, i.e if the incident intensity is initially zero (for example if the radiometer is shielded) and then changes abruptly to I_0 the output of the radiometer after a period of 1.84 s will correspond to I_0/e The initial driving speed in the x direction was 0.5 mm/sec which was slow enough for the radiometer output to accurately represent the intensity variation in the focal plane. It was found however that the process of mapping the focus in this way would take over an hour to perform, over which period the insolation conditions could change considerably. The scanning speed of the radiometer was therefore increased to 6.5 mm/sec and a focal plane map could then be accomplished in approximately 5 minutes. This resulted in a time lag of the radiometer response with respect to the variation in applied intensity, an electrical analogy to this situation is the charging of a capacitor in a RC circuit when the switch connecting a dc source is closed.

The data from the radiometer was corrected for the time response in the following way: Consider the true intensity distribution to be a series of discrete changes in intensity as shown in figure 7.3. The radiometer is positioned at the extreme x position before the scan begins, it is located in the low intensity region of the focus, i.e it is receiving solar radiation intensity that is small compared to the maximum of the focus, yet still represents a several fold concentration over the intensity incident on the concentrator. Assume the radiometer output is V_1 and that the incident intensity at this position is E_1, the radiometer has been in this position long enough so that the two values are equal. As the radiometer moves through the focus, stepwise increments in the intensity level to E_n result in the corresponding radiometer

$$V_1 = E_1$$

$$V_2 = E_1$$

$$V_3 = (E_2 - V_2)k + V_2$$

$$V_4 = (E_3 - V_3)k + V_3$$

$$V_{n+1} = (E_n - V_n)k + V_n$$

thus:

$$E_n = V_n + \frac{(V_{n+1} - V_n)}{k}$$
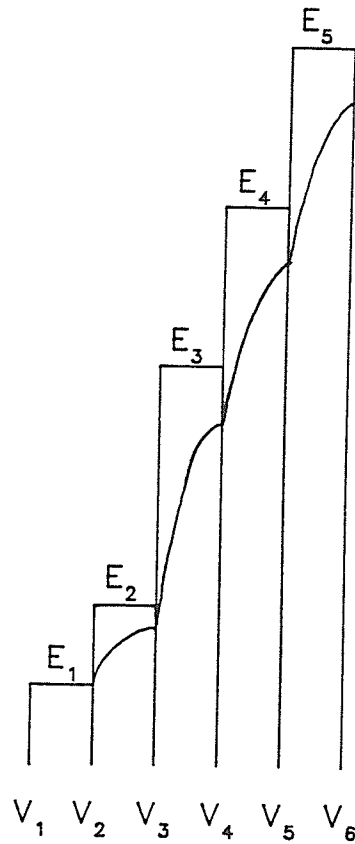
Figure 7.3 Radiometer time response correction. The data from the radiometer was corrected by considering the true intensity distribution to be a series of discrete changes in intensity.

response V_n as shown in the figure.

It can be seen that in general:

$$V_{n+1} = (E_n - V_n)\,k + V_n \qquad (7.1)$$

where the time response of the radiometer is given by:

$$k = \left(1 - \exp^{\frac{-\Delta T}{RC}}\right) \qquad (7.2)$$

ΔT is the reciprocal of the measurement rate.

rearranging:

$$E_n = V_n + \left(\frac{V_{n+1} - V_n}{K}\right) \qquad (7.3)$$

where E_n is that voltage corresponding to the true intensity when the voltage reading from the radiometer is V_n.

In order to verify the behaviour of the radiometer time response, a step heating function was applied to the calibrating heater. Figure 7.4 shows the output of the radiometer and a curve of the predicted response for step increases and step decreases to the calibrating heater. The area under the curves would, in practice, be proportional to the power at the focus. The difference between the predicted and measured values of this area is less than 2 %.

The data recorded by the PC was transferred to a VAX 11/750 for further analysis.

The measured data for the focal plane is shown in contour and transect plots in figure 7.5. For this data the incident intensity on the concentrator was

87
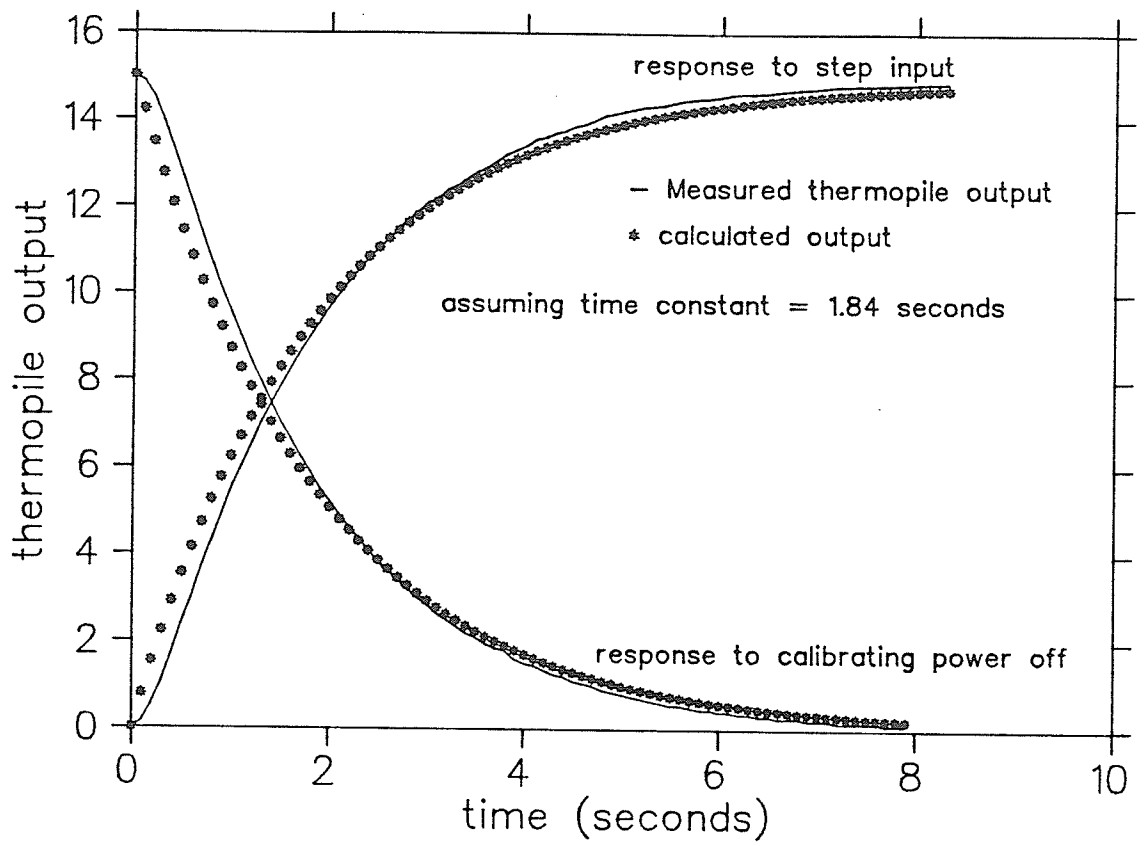
Figure 7.4 Radiometer time response correction. The figure shows the measured and predicted radiometer response to a step increase and a step decrease in calibrating heater current. The calibrating power is entirely equivalent to solar power in terms of response time. The area under each curve is proportional to the power contained in the region. The difference in areas between the measured and predicted cases is of the order of 2%.
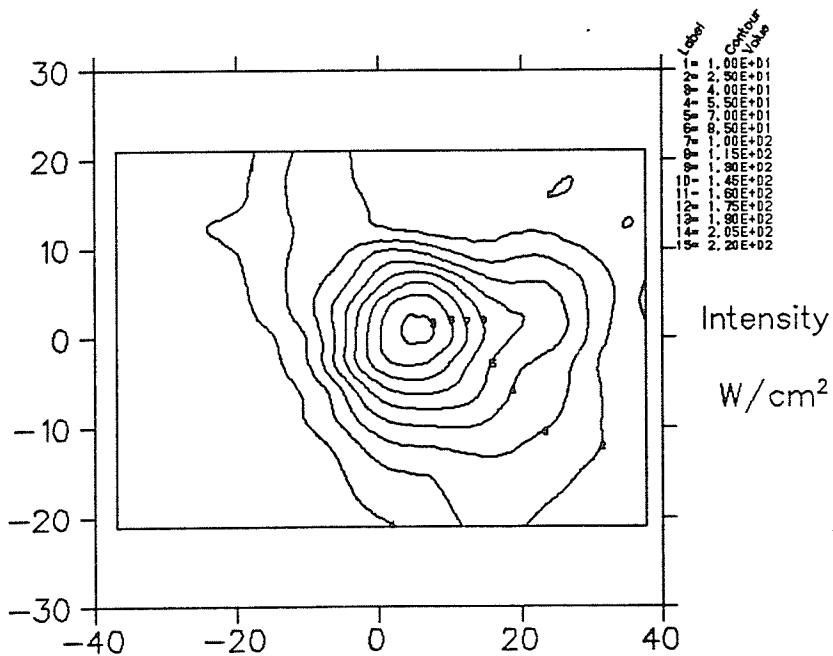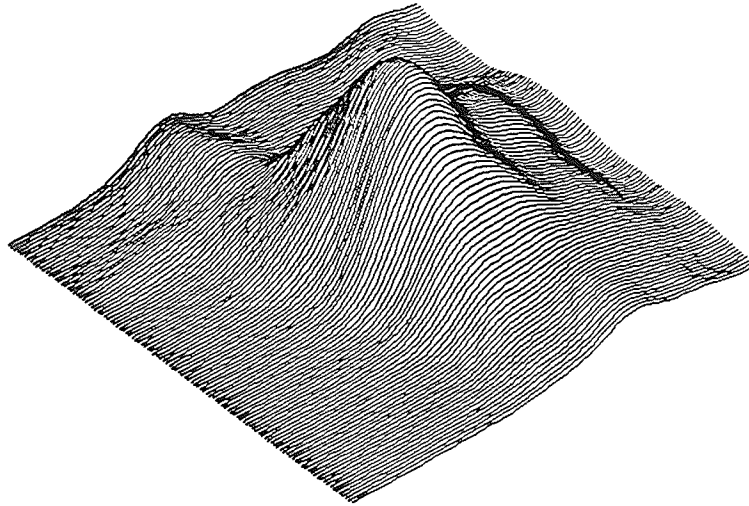
Figure 7.5 Contour and transect plots for focal plane intensity formed by the concentrating mirror on 27-08-85. For this data the incident sunlight intensity on the mirror was 856 W/m². The power contained in the focal region is 958 Watts.

856 W/m^2. The power contained in this region is 958 Watts.

7.5   Summary

The concentration ratio of the system has a maximum value of 1500 times which is of the order expected. However the measured power contained within the focal region is significantly less than the expected value. In order to further study the discrepancy between the two values a set of measurements were performed on the system and the results entered into a theoretical model. This work is described in the next chapter.

Chapter 8

The Prediction Of The Focal Plane Intensity Distribution Formed By a Parabolic Concentrator

8.1   Introduction

The measurement of the intensity distribution within the focal plane of the concentrating system revealed a discrepancy between the measured and the expected power avaliable. In order to investigate the origins of this discrepancy a series of measurements was performed on the collector system to determine the quality of figuring of the reflective surfaces.

It is also desirable to be able to predict in advance the focal plane intensity distribution and total power contained within the focus, since it may not always be possible to measure these quantities while an experiment is taking place. This chapter describes the measurement of parameters of the collector system, their incorporation into an existing model, and the comparison with the measured focal plane distribution.

8.2 The Problem:

The measurement of the intensity distribution in the focal plane began in earnest in December, 1983. The results of the first mapping are shown in figures 8.1 and 8.2. Figure 8.1 represents a scan through the center of the focus and figure 8.2 shows a transect/contour plot of the area of the focal plane containing the major part of the power. These measurements were performed on December 30, 1983 when the solar intensity was 535 W/m^2 and the ambient temperature -20°C.

To record the focal plane distribution the radiometer was driven on an "x-y" grid at the focal plane of the concentrator, y being the vertical direction and x the horizontal. Scans were made in the x direction (as described in the previous chapter) and the radiometer incremented in the vertical displacement.

Initially, the radiometer output was recorded by a chart recorder. Scans were performed for 27 vertical settings over a distance of 15.6mm, only half the plane was mapped, as it was assumed the distribution would be symmetrical. From each scan, 27 data points were read and manually entered into a VAX11/750 computer for analysis. The total travel in the x direction at this time was 53mm. By discretizing the data in this way, each value measured by the radiometer represents the concentrated intensity incident on an area $\frac{1.56}{26}$ cm by $\frac{5.3}{27}$ cm i.e 0.0117 cm^2. The total power contained within the measured area of the focus is given by:

$$\text{Power} = 0.0117 \sum_{i=1}^{n} \phi_i \quad \text{Watts} \qquad (8.1)$$

Where ϕ_i is the output from the radiometer in W/cm^2

92
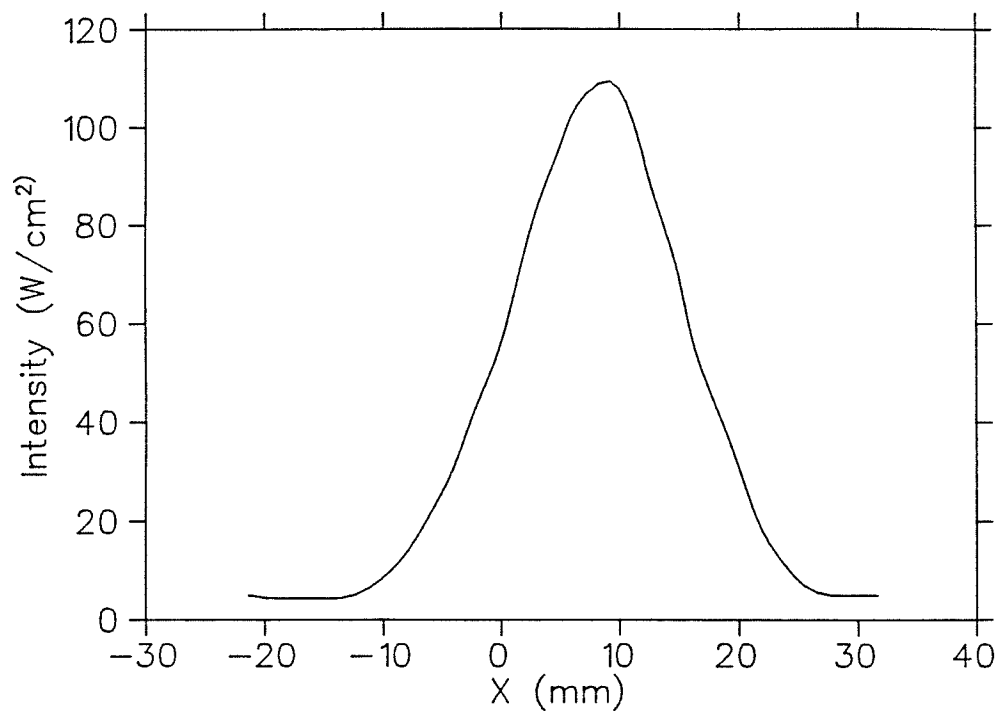
Figure 8.1 Focal plane intensity profile measured 31-12-83.
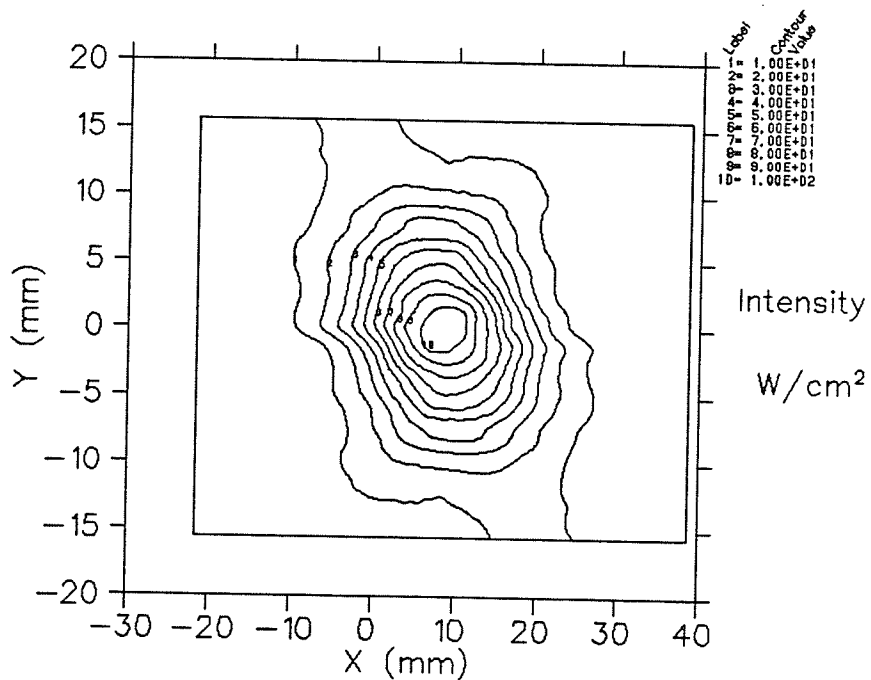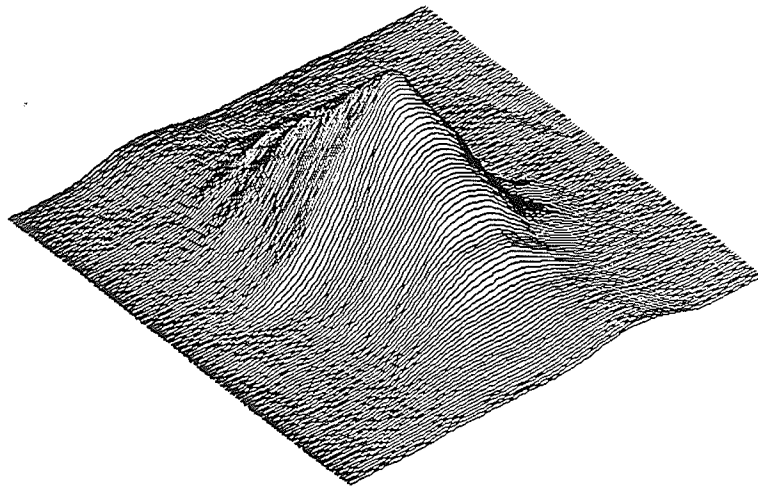
Figure 8.2 Contour and transect plots for 31-12-83. For this data the incident sunlight intensity was 535 W/m². The power contained in the focal region is 340 Watts.

In the case of the mapping of figure 8.2, this power is 340W.

One would expect that the power at the focus could also be calculated by multiplying the illuminated area of the concentrator by the intensity of sunlight incident. This leads to a gross discrepancy with the figure as calculated above:

$$\text{Power} = 535\,\text{W/m}^2 \text{ x } 2.83\,\text{m}^2 \; = \; 1515 \text{ Watts} \qquad (8.2)$$

In order to determine the cause of the apparent missing power at the focus, and to predict in advance the intensity distribution in the focal plane, a series of measurements was performed on the collector system and the parameters measured incorporated into an existing model. The details are described below:

8.3 A Model For the Prediction of Focal Plane Intensity Distribution Formed by a Concentrating Collector:

8.3.1 Introduction

In order to accurately predict the focal plane intensity distribution formed by a concentrating solar collector one must incorporate several parameters into a model, namely:

(i) The "sunshape" which takes into account the finite size of the solar disk and the intensity distribution across the disk. The sunshape function may change due to atmospheric scattering in a way that is essentially impossible

to predict, and some way must be found to incorporate this variation into a prediction model

(ii) The deviation of the concentrator shape from the ideal (parabolic) shape, it will be shown that this is the most important parameter in explaining the origin of the apparent missing power.

(iii) The reflectivity of concentrator surface.

(iv) Errors due to misalignment of the concentrator and errors caused by tracking inaccuracies.

(v) The part of the concentrator that is shaded, or that does not contribute to the power at the focus.

Early attempts at predicting focal plane distributions assumed perfect optics [36,37] or used raytrace techniques. A combination of the work of Pettit [38], Butler and Pettit [39] and Biggs and Vittitoe [40] has been presented by Harris and Duff [41] and it is this model that is described below. The predictions of the model are compared with measured data on the concentrator system.

8.3.2   The Model

Consider the reflection of light rays from a concentrator surface as shown in figure 8.3. The incident ray vector is shown as $\hat{I}$. For a perfect surface the reflected ray $\hat{R}$ will lie in the same plane as the incident ray and the surface normal $\hat{N}$. For a real concentrator surface, the reflected ray will take some other path such as $\hat{R}'$ or $\hat{R}''$ in the figure. Experiments by Pettit and Butler have shown that the deviation of $\hat{R}'$ about $\hat{R}$ may be described by a bivariate probability density function f(x,y) where:-
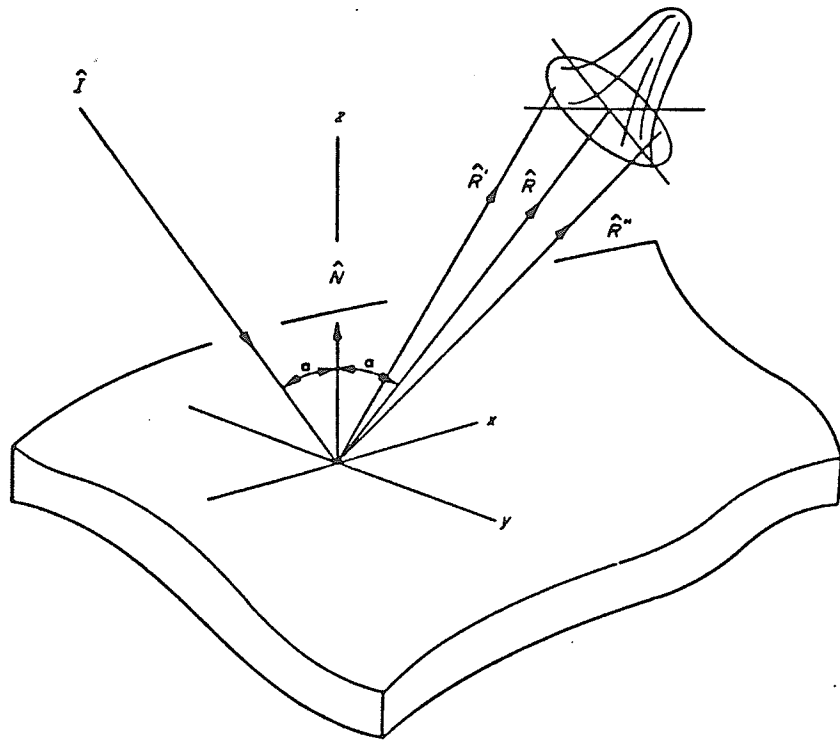
Figure 8.3 Reflection of light rays from a concentrator surface. [41] For the perfect surface the reflected ray $\hat{R}$ will lie in the same plane as the incident ray and the surface normal $\hat{N}$. For a real concentrator surface, the reflected ray will take some other path such as $\hat{R}'$ or $\hat{R}''$ in the figure.

$$f(x, y) = \frac{1}{2\pi\sigma_x\sigma_y}\exp\left(-\frac{x^2}{2\sigma_x^2} - \frac{y^2}{2\sigma_y^2}\right) \tag{8.3}$$

Where σ_x and σ_y characterize the rays reflected from the mirror surface.

The second parameter to be included when describing the distribution of rays reflected from the concentrator surface is the variation in incident angle due to sunshape. Sunlight incident on the concentrator surface is in the form of a diverging beam of light due to the finite size of the solar disk. The beam forms a cone with an apex angle of approximately 0.5 degrees, and the cone may be further widened due to scattering of the sunlight as it passes through the atmosphere.

In order to incorporate this effect, a second bivariate probability density function is introduced. Figure 8.4 shows the actual sunshape and the normal approximation having the same variance. In this way changes in the sunshape function due to atmospheric scattering can be easily entered into the prediction.

The cone of solar photons reflected by a point on the concentrator surface is formed by the convolution of the sunshape probability distribution function and the surface error probability distribution function. The summation at the focal plane of the intensities represented by these cones of photons will yield the required intensity distributions.

8.3.3   Application to a Parabolic Mirror Concentrator

Consider a cartesian co-ordinate system fixed to the mirror as shown in figure 8.5. The z axis is normal to the concentrator surface and the x axis intercepts the axis of symmetry of the concentrator. The components δx and δy are
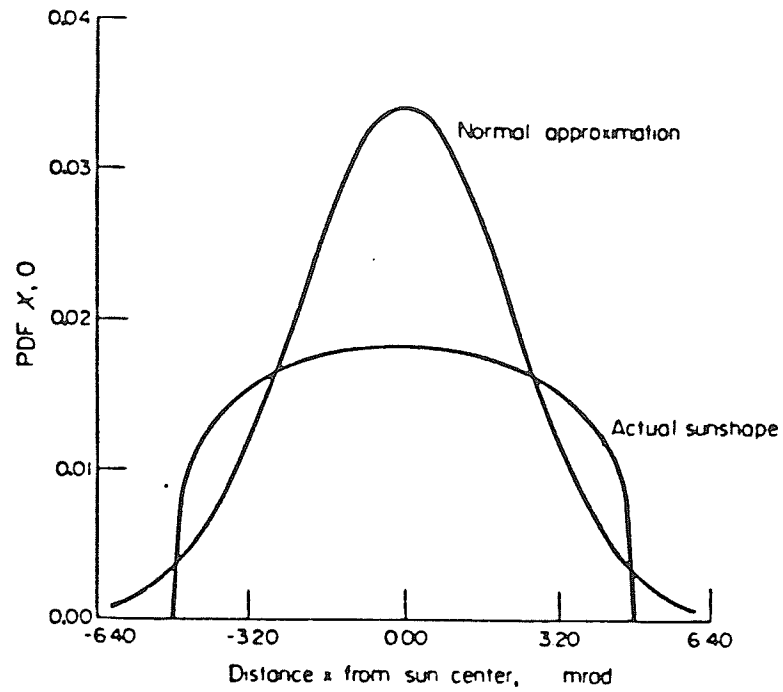
Figure 8.4 Sunshape function and bivariate probability density function with the same variance [41]. The sunshape function is incorporated into the prediction model by introducing a normal distribution function with the same variance.
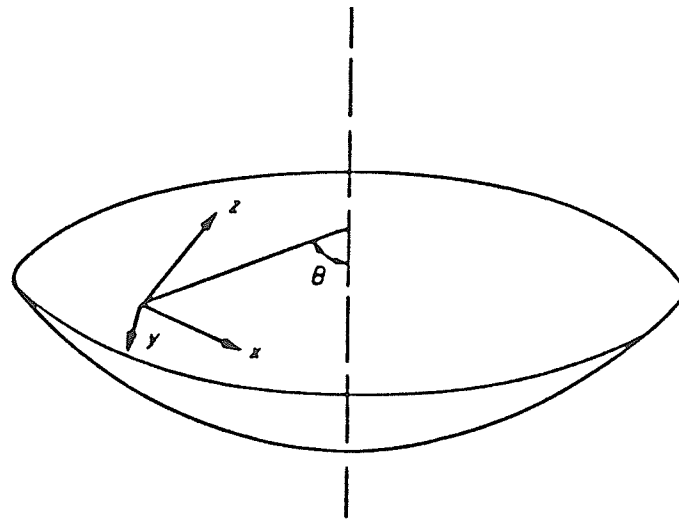
Figure 8.5 Convention of coordinates used in the model applied to a parabolic dish concentrator [41].

the angular deviation of the surface normal from the ideal surface normal.

Imagine an x-y grid located on the solar disk and let ϵx and ϵy represent the angular co-ordinates of a photon's origin. In the bivariate normal sunshape approximation ϵx and ϵy are normally distributed random variables. Since δx and δy are also assumed normally distributed, the target flux probability density function due to reflection from a given point on the concentrator can be approximated by a normal distribution having parameters:[41]

$$\sigma_x^2 = \left(\frac{R}{\cos\phi}\right)^2 \left(\sigma_{\epsilon x}^2 + 4\sigma_{\delta x}^2\right) \tag{8.4}$$

$$\sigma_y^2 = R^2 \left(\sigma_{\epsilon y}^2 + \left(2\cos\frac{\theta}{2}\right)^2 \sigma_{\delta y}^2\right) \tag{8.5}$$

8.3.4 Flux Distribution Produced by a Parabolic Concentrator

To find the flux distribution produced by a parabolic concentrator one must find the flux probability density function produced by rays reflected by the locus of points on the concentrator located by the angle θ as shown in figure 8.6. An analytic expression for this probability density function is given by: [41]

$$f_\theta(x, y) = B\exp(-A)I_o(A) \tag{8.6}$$

where:

$$A = \frac{x^2 + y^2}{4R^2} \left[\frac{\cos^2\theta}{\sigma_{\gamma x}^2} - \frac{1}{\sigma_{\gamma y}^2}\right] \tag{8.7}$$
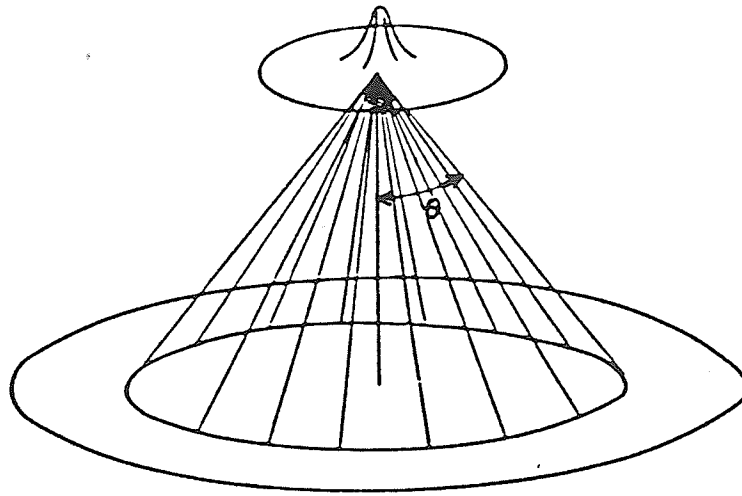
Figure 8.6 Rays reflected from angle θ form the focal plane flux distribution. To find the flux distribution produced by a parabolic concentrator one must find the flux probability density function produced by rays reflected by the locus of points on the concentrator located by the angle θ as shown in figure.

and:

$$B = \frac{\cos\theta}{2\pi R^2 \sigma_{\gamma x} \sigma_{\gamma y}} \exp\left[-\frac{x^2 + y^2}{2R^2 \sigma_{\gamma y}^2}\right] \tag{8.8}$$

where R is the distance from the point of the theoretical focus point:

$$R = \frac{2f}{1 + \cos\theta} \tag{8.9}$$

and:

$$\sigma_{\gamma x}^2 = \sigma_{\epsilon x}^2 + 4\sigma_{\delta x}^2 \tag{8.10}$$

and:

$$\sigma_{\gamma y}^2 = \sigma_{\epsilon y}^2 + \left(2\cos\frac{\theta}{2}\right)^2 \sigma_{\delta y}^2 \tag{8.11}$$

and I_o is the modified Bessel function of zero order.

The total flux distribution at the focus is given by:-

$$f(x, y) = \int_{\theta_{min}}^{\theta_{max}} f_\theta(x, y) p(\theta) d\theta \tag{8.12}$$

Where $p(\theta)$ is the probability that a photon reaching the target came from the interval $d\theta$ located at θ, which for a parabolic concentrator is given by:-

$$p(\theta) = \left[\frac{1}{1 + \cos\theta_{max}} - \frac{1}{1 + \cos\theta_{min}}\right] \frac{\sin\theta}{(1 + \cos\theta)^2} \tag{8.13}$$

Since the equation above cannot be solved analytically it may be approximated by:-

$$f(x, y) = \sum_{i=1}^{n} f_{\theta_i}(x, y) P(\theta_i) \tag{8.14}$$

The computer code written by Harris [41] to predict the focal plane intensity profiles was obtained and adapted to run on a microcomputer at the University of Manitoba [42]. The program prompts the user for:

(i) Focal length of concentrator.

(ii) Dish distortion parameter $\sigma_{\delta x}$, $\sigma_{\delta y}$

(iii) Sunshape parameter ϵx, ϵy.

(iv) Minimum and maximum dish angle to be included in computations.

(v) Focal plane target radius to which computations are required.

(vi) Dish Aperture.

(vii Incident solar beam intensity.

(viii) Dish surface reflectivity.

The parameters (iv) and (v) were added to the program to include shading effects involved in the system at the University of Manitoba. After reading in the parameters the program calculates the focal plane intensity versus position. In order to compare the predicted profile with that measured, a series of measurements were performed on the system to determine values for the parameters listed above. This is described in the next section.

8.4 Measurement of System Parameters:

In order to determine the values of the parameters described above the following aspects of the concentrator system need to be evaluated.

(i) Obliquity Effect. (As related to area of concentrator illuminated)

(ii) Concentrator Shading Effects.

(iii) Concentrator reflectivity.

(iv) Concentrator distortions.

Further influences listed below will also affect the focal plane intensity variation:

(v) Heliostat flatness.

(vi) Heliostat reflectivity variation across entire surface.

(vii) Heliostat tracking accuracy

It is possible that at a later date these may also be included in the model. At the time of the measurements above these parameters were optimized as will be described below.

8.4.1 Area of Concentrator Illuminated

(i) Obliquity Effect

One of the input parameters to the model of Harris and Duff is the concentrator area. For a sun tracking paraboloid this is simply the area the mirror surface presents to the sun. In the case of a heliostat concentrator configuration this area is constantly changing due to the obliquity effect.

As the heliostat tracks the apparent motion of the sun, reflecting the light toward the concentrator, different areas of the concentrator are illuminated due to the oblique angle between the axis of the system and the plane of the heliostat face. It was possible to design the system so that the concentrator is always illuminated in its vertical dimension (see chapter 6.). A computer

104

program was written to calculate the area of the concentrator illuminated at any time by projecting the heliostat orientation into the x-y plane formed by the rim of the concentrator as shown in figure 8.7.

(ii) Concentrator Masking

The illuminated area of the concentrator is also reduced by objects between the heliostat and the concentrator. It was found by measurement that the Louvre doors, in their fully open position, obscure 10% of the illuminated area of the dish. Similarly it was found that the xyz table and stand obscure 1730 cm^2 of the illuminated area.

As the reflective film coating was applied to the concentrator surface, small bubbles would appear under the film, further, as the film was applied in triangular shaped strips, the edge of each strip was laid over the previous strip in an effort to cover the whole dish area and leave no unreflective areas.

It was found during the laser-scanning of the dish, described below, that rays striking either the bubbles or the seams were not reflected onto a 100 mm by 50 mm grid placed at the focus. Previous measurements of the focal plane intensity had shown that this grid effectively defined the extent of the focal region. Therefore the areas of the bubbles and seams are essentially shaded areas. Surprisingly these areas totalled 3526 cm^2 or 12.5% of the illuminated area.

8.4.2 Reflectivity of ECP91A

The reflectivity of the reflecting surfaces is another input parameter into the focal plane intensity prediction. The variation in reflectivity of the heliostat with the length of time since it was last cleaned, or since it last rained, etc. was eliminated by placing an Eppley Laboratories normal incidence
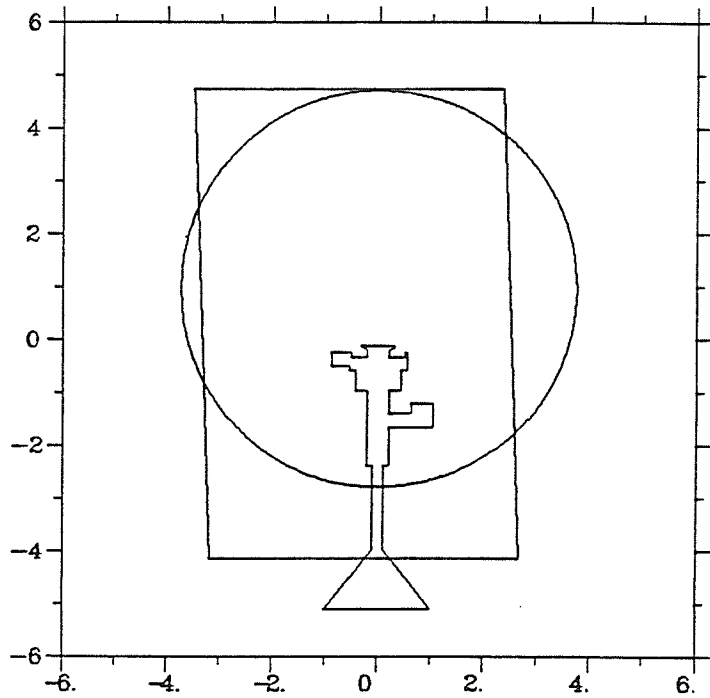
Figure 8.7 Output of computer program to show portion of concentrator illuminated due to the obliquity effect. The program also calculates the area of the mirror that is illuminated.

pyrheliometer between the heliostat and the concentrator, which measures the light intensity incident on the concentrator directly.

To determine the reflectivity of the film coating the concentrator, known as ECP91A, a length was peeled from the concentrator and fixed to a piece of glass. Two Eppley normal incidence pyrheliometers were used to determine the reflectivity of the film. The first was pointed directly at the sun to read the incident normal intensity, and the second was illuminated by reflection from the ECP91A film. In this way the reflectivity, and its variation with angle of incidence could be investigated.

It was found that the reflectivity of the film was $(85\pm2)\%$ and was essentially independent of angle of incidence (only those angles of incidence that would occur on the concentrator were investigated).

8.4.3   Evaluation of Concentrator Profile Distortions

For perfect focusing of rays from the sun the concentrator surface must be a paraboloid of revolution. In practice it will not be and its deviation from a perfect parabolic shape must be measured for incorporation into the prediction model. In order to determine the concentrator profile distortions an $x'\,y'$ grid was placed at the focal plane as shown schematically in figure 8.8. A Helium Neon laser was mounted on a travelling telescope arrangement and placed approximately 3m away from the concentrator. A hole was made at the center of the $x'\,y'$ grid. When the laser light passed through this hole, was reflected by the concentrator, and passed through the hole again on reflection, the origin of co-ordinates was found. The set-up was aligned such that x and y movement of the laser head was in a plane parallel to that formed by the rim of the concentrator.
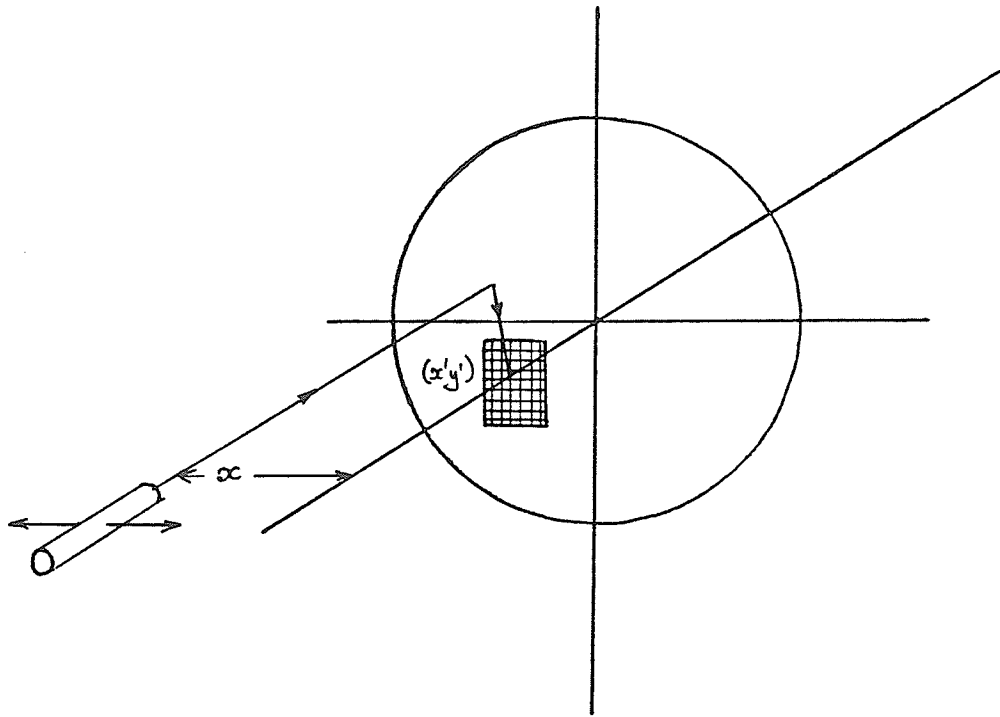
Figure 8.8 Arrangement to determine concentrator surface distortions. The beam from a laser located at (x,y) strikes the concentrating mirror and is reflected to strike the focal plane at (x',y') from these data the figuring accuracy of the mirror is determined.

The laser head was first moved in the horizontal, or x direction, with the vertical position corresponding to the center of the concentrator, at increments in x of 2 cm. The intersection of the reflected beam with the focal plane, $x'y'$ was recorded. From these data the angular deviation between the normal to the concentrator surface and the ideal normal was calculated as shown below. The equation describing the surface of a paraboloid of revolution in 3 dimensions, with z axis the axis of symmetry may be written:-

$$x^2 + y^2 = 4fz \qquad (8.15)$$

the unit normal to the ideal paraboloid is given by:

$$\hat{n} = \pm \frac{\nabla F}{|\nabla F|} \qquad (8.16)$$

where:

$$F(x, y, z) = x^2 + y^2 - 4fz = 0 \qquad (8.17)$$

taking the inward directed normal:

$$\hat{n} = \frac{-2x\hat{x} - 2y\hat{y} + 4f\hat{z}}{(4x^2 + 4y^2 + 16f^2)^{\frac{1}{2}}} \qquad (8.18)$$

the angle of incidence α of the laser beam is given by:

$$\alpha = \cos^{-1}\left(\hat{z} \cdot \hat{n}_{inward}\right) \qquad (8.19)$$

$$= \cos^{-1}\left[\frac{4f}{(4x^2 + 4y^2 + 16f^2)^{\frac{1}{2}}}\right]$$

109

The point of intersection of the reflected beam with the grid placed at the focal plane is $(x', y', z' = f)$. The unit vector between the point of incidence on the concentrator and the intersection point on the focal plane grid is $\hat{u}$ given by:

$$\hat{u} = \frac{\langle x' - x, y' - y, f - \frac{x^2 + y^2}{4f} \rangle}{\left[(x' - x)^2 + (y' - y)^2 + \left(f - \frac{x^2 + y^2}{4f} \right)^2 \right]^{\frac{1}{2}}} \qquad (8.20)$$

The angular deviation between the real normal to the concentrator and the ideal normal is given by:

$$\hat{n}_{\text{deviation}} = \frac{\alpha - \beta}{2} \qquad (8.21)$$

where:

$$\beta = \cos^{-1} (\hat{u} \cdot \hat{n})$$

hence:

$$\hat{n}_{\text{deviation}} = \frac{1}{2} \cos^{-1} \left(\frac{4f}{(4x^2 + 4y^2 + 16f^2)^{\frac{1}{2}}} \right)$$

$$- \cos^{-1} \left(\frac{[(-2x)(x' - x) + (-2y)(y' - y) - 4f^2 - x^2 + y^2]}{\left[(4x^2 + 4y^2 + 16f^2)((x' - x)^2 + (y' - y)^2 + \left(f - \frac{x^2 + y^2}{4f} \right)) \right]} \right) \qquad (8.22)$$

A computer program was written to calculate the concentrator surface distortions from the measured data [43]. The results of the laser scanning are shown in figure 8.9. The dimensions of the grid placed at the focus were ± 100 mm in x' and ± 50 mm in y'. These dimensions were chosen by considering previous focal plane maps and by the range of movement available

110
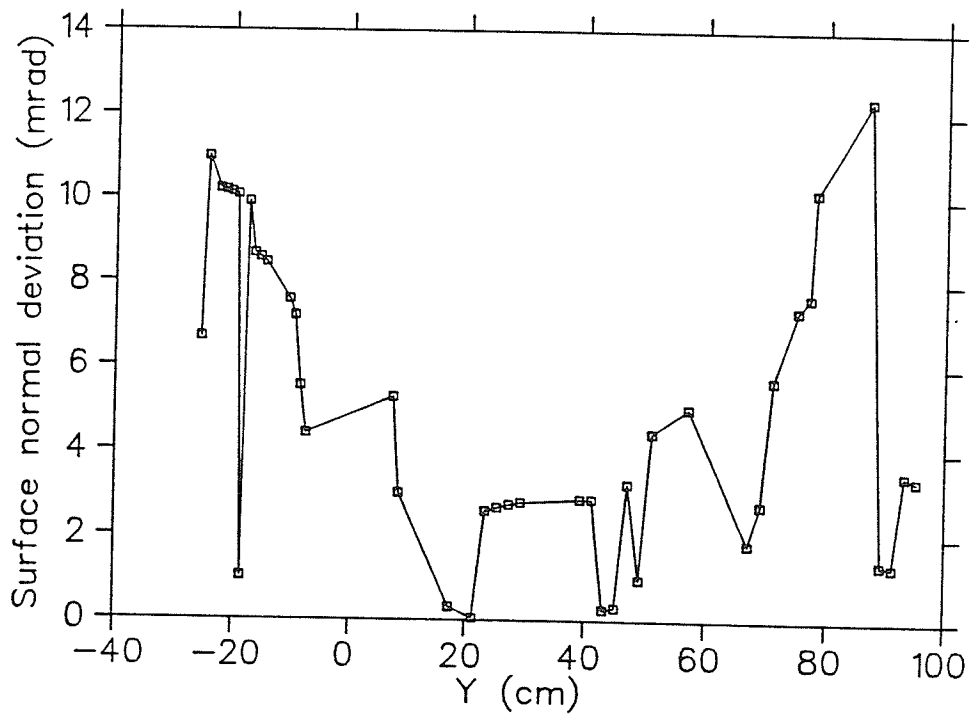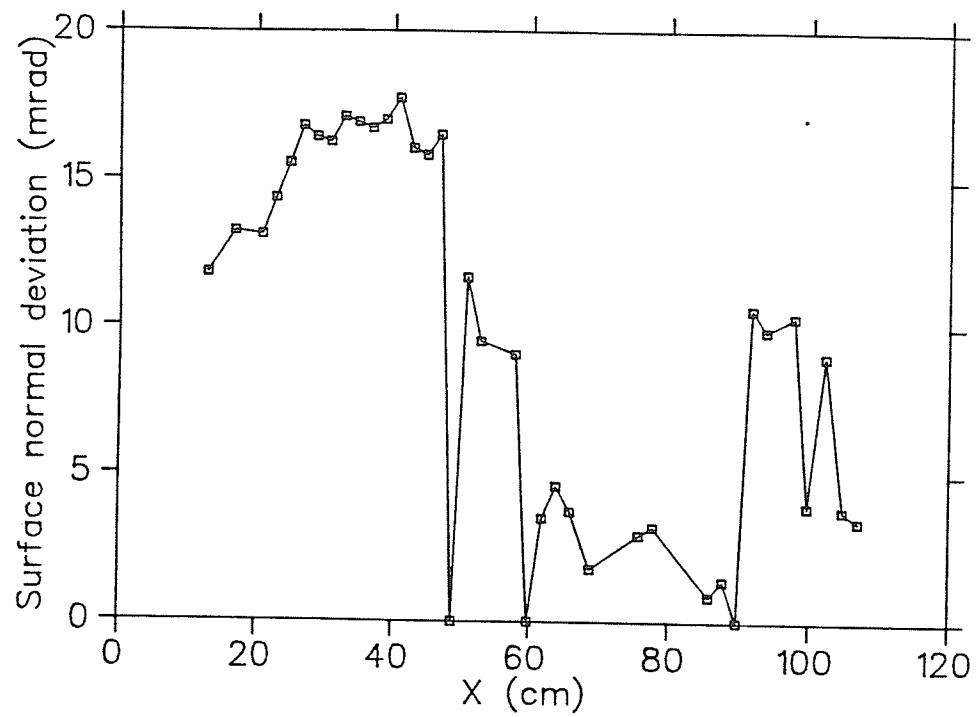
Figure 8.9 Concentrator distortion versus distance from center in x and y. The deviation of the concentrating mirror surface normal from perfect, expressed in milliradians, is plotted as a function of horizontal and vertical distance form the center of the mirror.

to the radiometer. They represent the effective dimensions of the focal spot. It was also assumed that any solar receiver used with this system would have an aperture much smaller in area than the area of the grid, since for solar-thermal energy converters the area of the aperture is related to the overall conversion efficiency in that the smaller the aperture the higher the efficiency.

During the laser scanning of the concentrator, it was found that rays incident at values of x, or y greater than 98 cm, on reflection by the mirror, missed the target completely. This effectively means the radius of the concentrator is 98 cm and not its physical radius of 114 cm. Together with the large amount of shading caused by the xyz table, the louvre doors, and the film seams, the origin of the majority of the missing power at the focus was found.

8.5 Incorporation of measured data into the model

One of the basic assumptions of the model of Harris and Duff, as measured by Pettit and Butler [39] is that the surface distortions of a concentrator can be described by a normal distribution characterized by $\sigma_{\delta x}$ and $\sigma_{\delta y}$

Figure 8.10 shows the distribution of surface distortions for the x scan, as can be seen, the assumption is not valid for the concentrator described here. In order to see what effect the parameters measured above would have when entered into the prediction, the averages of the dish distortions in x and y were used. After the system parameters were measured as described above, a further mapping of the focal plane was performed. The results are shown in figure 8.11. The focal spot profile is now asymmetric, suggesting the

112
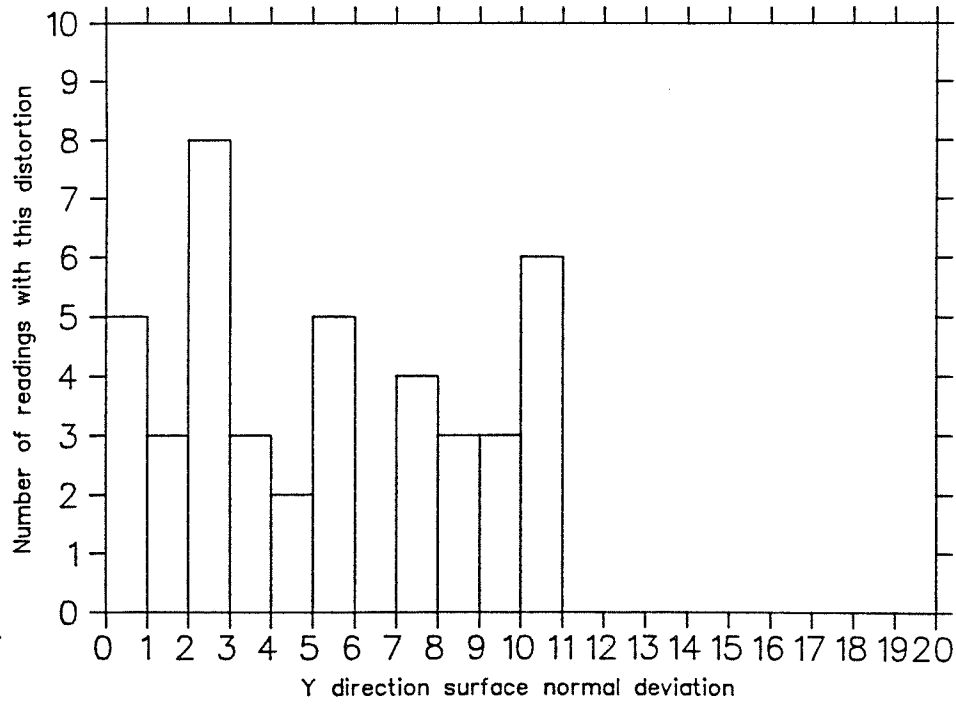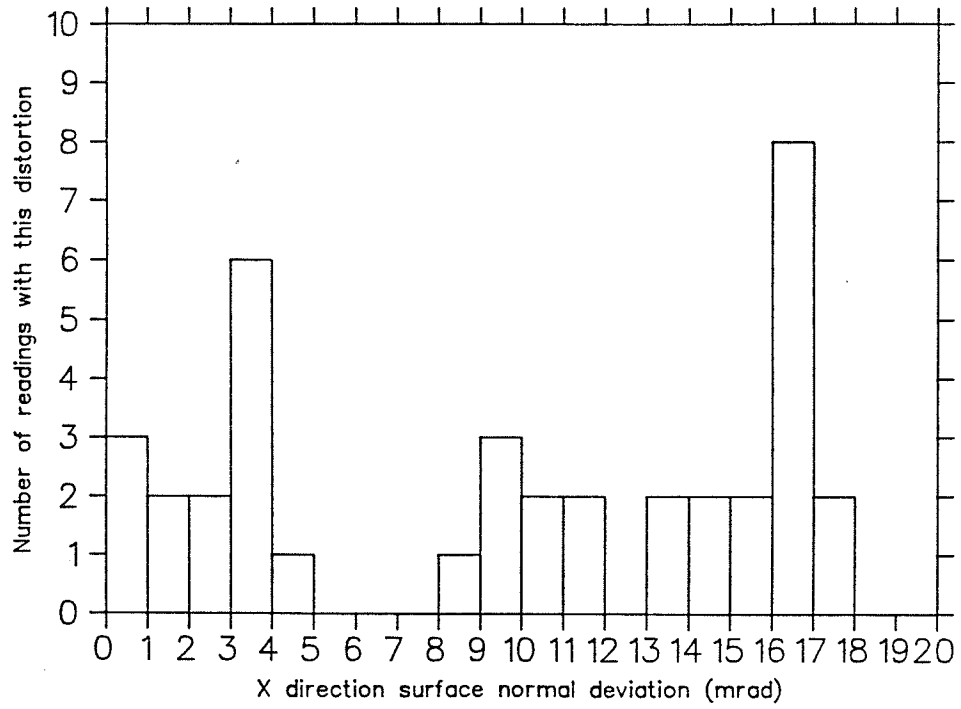
Figure 8.10 Concentrator measured distortion distribution. The value of the surface normal deviation from ideal is plotted against the number of data points recorded with that value.
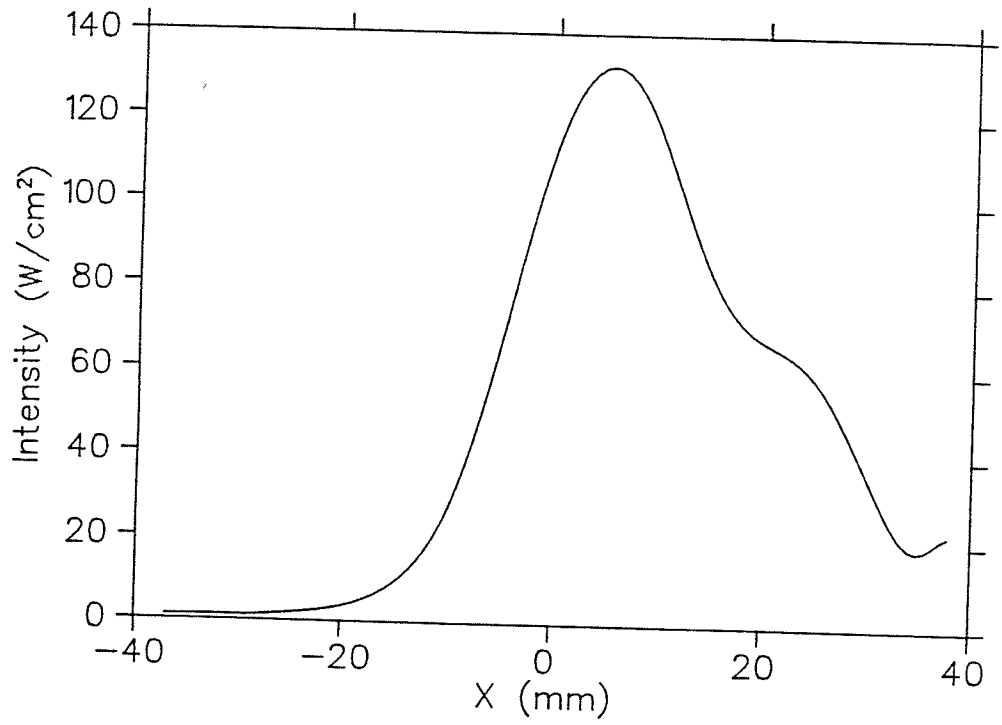
Figure 8.11 Measured focal plane intensity for 04/27-08-85. For this data the incident sunlight intensity on the mirror was 856 W/m².

concentrator was distorted by the strong gusts of wind (up to 100 km/hour) that had occurred since the construction was completed. A comparison with the prediction is shown in figure 8.12. The predicted intensity is strongly dependent on the values of $\sigma_{\delta x}$ and $\sigma_{\delta y}$, as shown in figure 8.13. The range bars shown are for deviations of ± 0.5 mrad from the values measured.

It can be seen that the measured intensity profile is displaced from the predicted, due to skewness of the concentrator with respect to the axis of the collector system, or due to misalignment of the tracking sensor. The displacement of peaks is 5 mm.

When the effects of obliquity and shading are taken into account, there is still a discrepancy between the measured power at the focus (939 W) and the predicted power (1400 W). This power is probably located around the edges of the focal plane limits, as described above, in values of intensity which although small compared to the peak intensity, are still several fold concentrations of the incident intensity from the heliostat. Further, since this intensity falls on a larger area, it accounts for all of the missing power. To investigate this, the travel in the x,y and z directions would have to be increased several times, and such an investigation would not increase the power that could be collected by a receiver.

It is possible that a more detailed measurement of the concentrator distortions, perhaps at 0.5 cm intervals would yield a normal distribution and it would be advisable to do this. It is also possible that values of $\sigma_{\delta x}$ and $\sigma_{\delta y}$ that best describe the intensity variation could be found by comparison of the measured profiles with predictions. When such a process was optimized regular mappings of the concentrator with the radiometer would still need to be performed to ensure that wind conditions had not distorted the concentrator further.
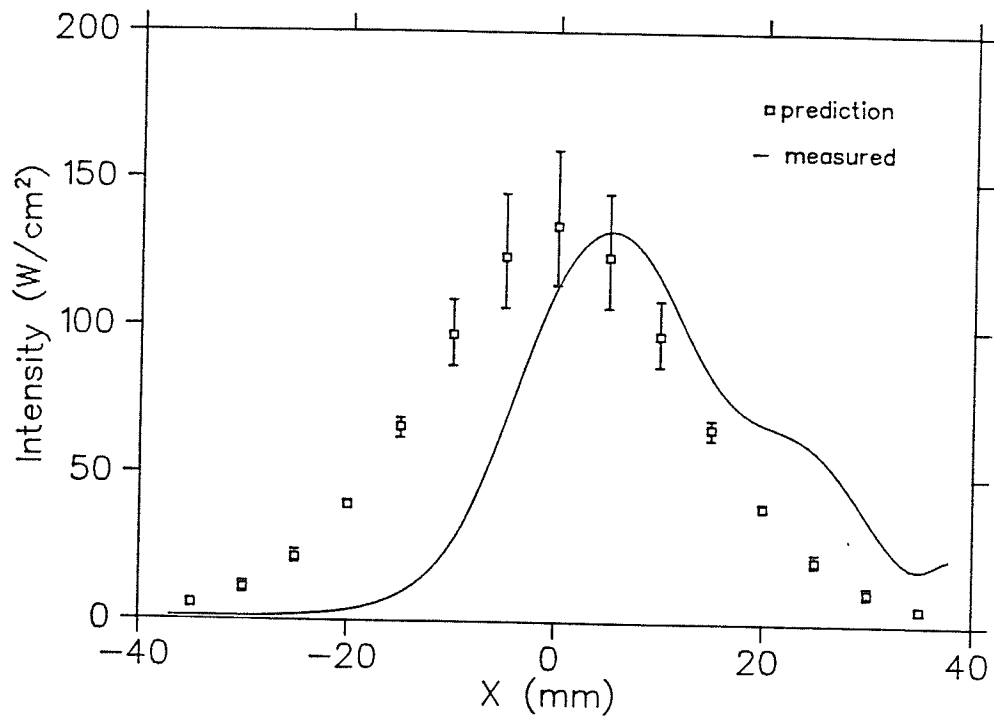
Figure 8.12 Comparison between theoretical prediction and measured focal plane intensity. The predicted and measured intensity distributions agree well. The separation of the peaks is 5mm. It will be possible to account for this skewness of the concentrating mirror in the prediction code.
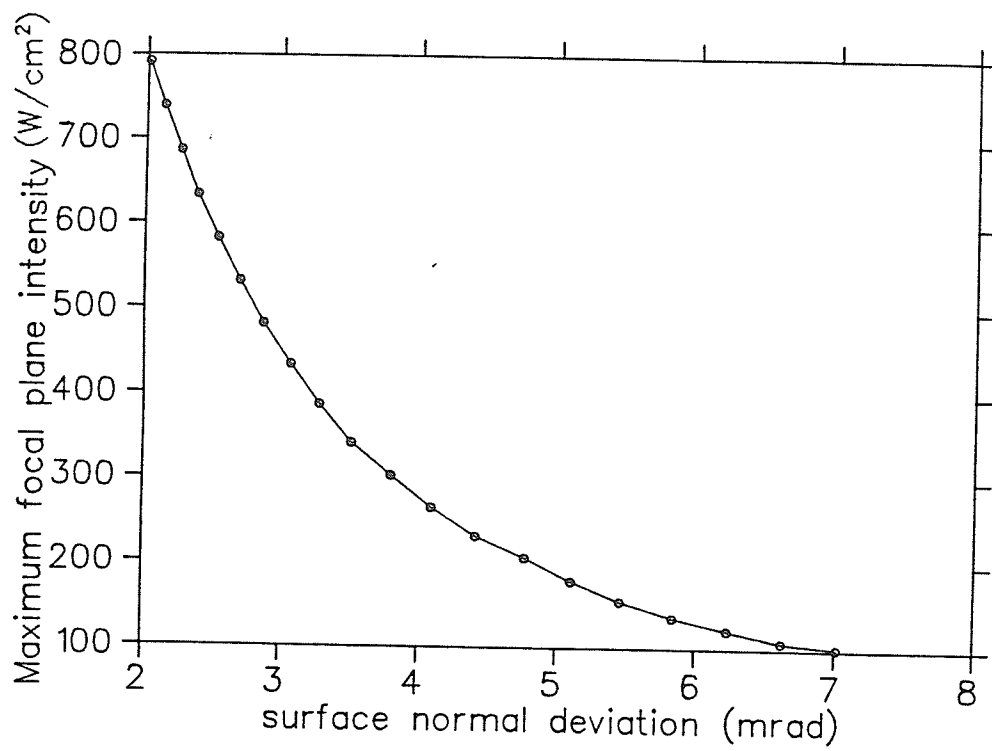
Figure 8.13 Dependence of intensity predicted versus $\sigma_{\delta x}$ and $\sigma_{\delta y}$ for theoretical model.

8.6 Other Effects

The model correlates several measured parameters to predict the focal plane intensity distribution. There are however, other variables in the system described here that also affect the intensity distribution and would be difficult to incorporate into the model. These parameters are described briefly below.

(v) Heliostat flatness.

The heliostat consists of 6 mirror modules mounted to a rib type frame. The reflecting surfaces of the modules must be parallel to a single plane if the heliostat is not to affect the focusing action of the concentrator. To achieve this, a laser was mounted on a large x-y frame at a distance of approximately 10 m from the heliostat where x is the horizontal and y the vertical direction. The heliostat was set so that the plane of the mirrors was approximately vertical (and parallel to the xy plane). The laser was pointed at the center of each mirror module in turn, and the module independently adjusted so that the reflected and incident laser beams lay along the same path. In this way the surface normals from the centers of the mirror modules are made parallel to each other. After alignment of a mirror, the laser was scanned along the rest of the mirror surface. Distortions corresponding to an angular deviation of the surface normal of several mrad were observed at some points on the surface. Given that the mirror modules are designed to minimize distortions, little more can be done about this.

The heliostat is of a counterbalance design. The frame which holds the mirror modules is constructed from steel "u" channel and is consequently very strong. However the frame as a whole tends to bow by different amounts depending on the angle of elevation of the heliostat. This in turn affects the relative alignment of the heliostat mirror modules.

The mirrors used in the mirror modules are industry standard back silvered mirrors. When the reflectivity of each module was measured independently, it was found that variations across the heliostat of $\pm 10\%$ were possible.

8.7 Summary

A mathematical model which accepts mirror surface figuring parameters as input, has been used to predict the focal plane intensity distributions formed by a heliostat concentrator configuration. The model predictions agree well with the data measured in the focal plane region. Comparison of the two sets of data show that the concentrating mirror is slightly skewed with respect to the optical axis of the system. A slight modification to the prediction code will account for this skewness.

The comparison of focal plane data, measured with high accuracy, with the predictions of the theoretical model are the first available for a concentrating system of this type.

The accuracy of figuring of the mirror surfaces is of crucial importance to solar energy collector systems which employ focussing. It is possible to receive less than 50 % of the power at the focus that would be expected by a simple calculation multiplying the area of the focussing collector by the incident intensity.

The major conclusions and observations drawn from the work on the solar intensity concentrator system are described in chapter 10. The following chapter contains a description of the potential applications of concentrated intensities, this is followed by a description of a new form of solar energy converter proposed at the University of Manitoba.

Chapter 9

Potential Applications of Highly Concentrated Beams of Solar Energy

9.1 Introduction

Solar energy converters receive the sun's energy from collectors and convert the energy into another form that is more convenient to transport and use, or into a form in which it may be stored. In some cases the converters may form part of the collector as in, for example, a flat plate type collector or a solar cell array. In other cases the converter and receiver are separate, for example the converter may be placed at the focus of a concentrating mirror type collector.

These converters fall into the broad categories of (i) solar-thermal, (ii) solar electric and (iii) "solar-heat of fusion" converters.

This chapter contains a brief description of each category. This is followed by the description of a new conversion scheme, proposed at the University of Manitoba, which involves the direct generation of electricity through the use of a cesium plasma which is sustained be solar energy.

120

9.2 Solar Thermal Receivers

In solar-thermal converters the incident solar energy is received by a working fluid in the form of heat. The working medium, for example, air, steam or ammonia is then used to drive an engine specifically adapted to the purpose, for example, a Stirling engine [44], Rankine-Cycle engine [45] or a steam turbine. The power output from the engine is used to drive an electrical generator.

These kinds of converters for solar energy have been vigorously studied in the recent wave of interest in solar energy due to existing technology in their design and construction. The overall efficiency (electrical energy output versus solar energy input) of the converter is limited by the combination of the Carnot efficiency for the engine part of the converter and by the efficiency of the electrical generator. The overall efficiency of such systems is between 25-30 %.

9.3 Solar-Electric

The most common form of solar-electric device converts solar energy directly to electricity via a photovoltaic process. Solar cells, wired together in an array are capable of generating several megawatts of power. Their efficiency is typically lower than that for a Stirling engine arrangement since the spectral response of a solar cell is not well matched to the spectral distribution of energy from the sun. Figure 9.1. shows the response of a monocrystalline solar cell which has a maximum of its response at a wavelength of 833 nm whereas the maximum of the solar output occurs at 500 nm.

The efficiencies available from solar cell arrays has slowly increased since
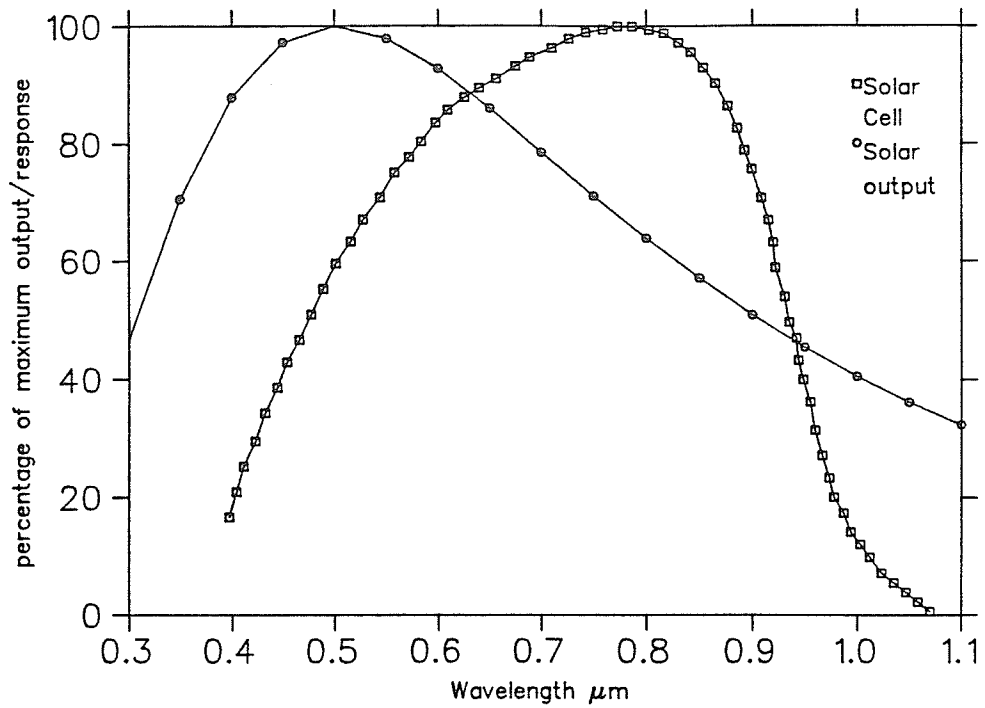
Figure 9.1 Solar photovoltaic cell spectral response compared to solar spectrum. The frequency at which a monocrystalline solar cell shows its maximum response to light (833 nm) is not well matched to the maximum of the solar spectral distribution (500 nm). Hence the relatively low efficiency for these cells.

they were first manufactured. The current value of efficiency with which solar cells directly convert solar energy to electrical energy is of the order of 27%. Higher efficiencies have been obtained by concentrating sunlight onto cells manufactured for the purpose.

9.4 Solar-Heat of Fusion

A third method of collecting solar energy is the "solar-heat of fusion" method. Solar energy is used to accomplish a chemical reaction, the products of which have a higher heating value than the original reactants. In this way a part of the solar energy is both collected and stored at the same time. The application of solar energy to the retorting of shale oil is discussed below.

9.4.1 Solar Energy in Oil Shale Retorting

The U.S. known reserves of petroleum are equivalent to 36 billion barrels of oil (bbl). However, the known reserves of oil shale are equivalent to 2,300 bbl. In Canada oil shale is found in parts of Manitoba and Saskatchewan and supplements the 26 bbl of oil equivalent of the Athabasca tar sands in Alberta. The potential application of solar energy in extracting energy from the shales is described below.

Oil shale is a mixture of organic and inorganic material in the form of thinly layered sedimentary rocks widely dispersed across the surface of the earth. The organic component of the oil shale is called kerogen, which can be decomposed by heat into oil and gas. This process of decomposing the kerogen is known as pyrolysis or retorting.

Kerogen may be subdivided into three types on the basis of the petroleum

products generated as shown in figure 9.2.

Kerogen I - Generates mostly oil vapour. (Green River, Colorado Shale)

Kerogen II - Generates mostly oil and some gas. (German shales)

Kerogen III - Generates mostly gas.

Shale oil found in Manitoba is a mixture of types II and III as shown in the diagram. Shales from the Green River area typically yield 25 gallons/ton (100 litres/tonne) of shale, whereas Manitoba shales yield at best 15 gallons/ton (60 litres/tonne) [46].

9.4.2 Oil Shale Retorting Energy Balance

The decomposition of Kerogen with applied heat is as follows:

Kerogen $\Rightarrow$ Bitumen $\Rightarrow$ Oil + Gas + char.
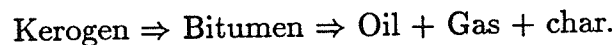
In the use of shale oil a a source of energy the exothermic processes are:

(i) combustion of oil

combustion of CHx

combustion of CH_4

combustion of H_2

combustion of C

(ii) combustion of iron pyrites (FeS_2)

The endothermic processes in decomposing the shale are:

(i) Kerogen decomposition (0.33 MJ/kg)

(ii) release of bound water from hydrated silicates

(iii) decomposition of carbonate minerals

124
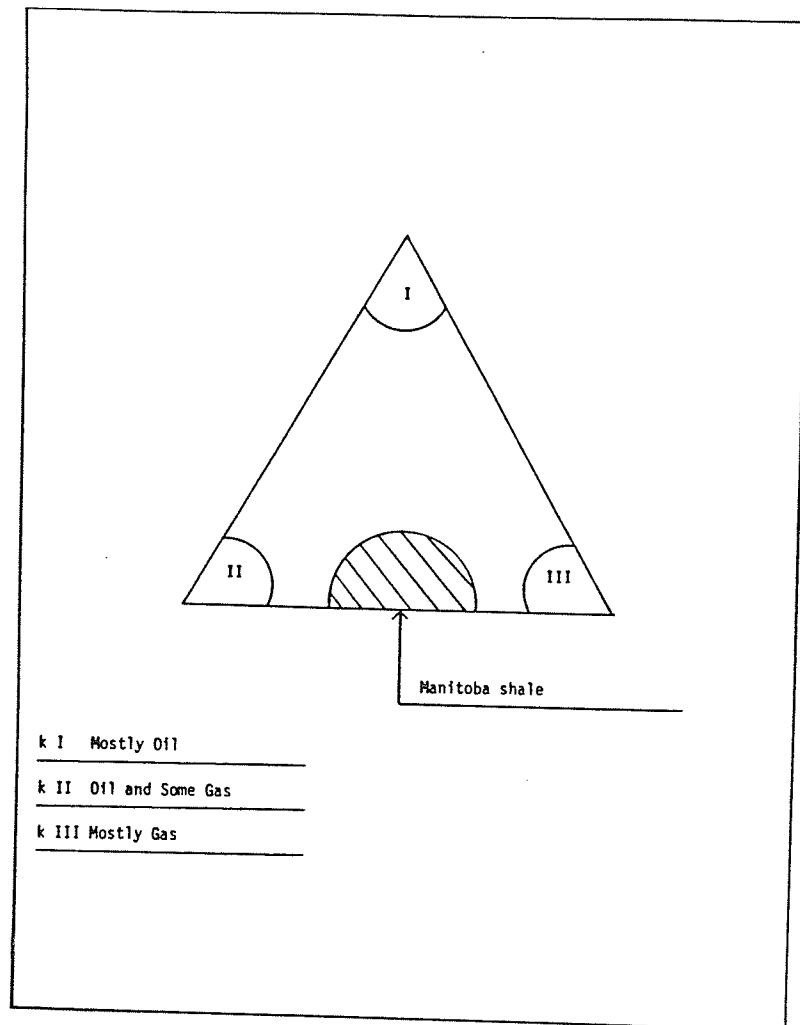
Figure 9.2 Kerogen classification on products derived.

Under these conditions the total endothermic energy is equal to the total exothermic energy for class II kerogen, at grades of 19.2 gal/ton. If solar energy is used to provide the required energy for decomposition of the kerogen, this represents a way of storing the solar energy.

9.4.3 Heating Rate

The yields of shale oil are determined by a laboratory standard known as Fischer Assay, whereby a known amount of shale is heated at 12 °C/minute to 500 °C and is then held at 500 °C for 30 minutes.[47] Oil yields are quoted from this.

It has been shown that the oil release rate and the oil yield from shale are both functions of the heating rate as shown in figures 9.3 and 9.4 [48]. If the heating rate of the decomposition of shale is increased to 100 °C/minute yields of 115% Fischer assay are achievable. Further, the higher the heating rate the less organic carbon remains in the spent shale.[49] Concentrated solar energy provides the possibility of very high heating rates and the associated increase in oil yield. The heat may be applied directly to the surface of a moving bed of shale, through a window. Alternatively, solar heating could be retro-fitted to an existing process such as the Tosco process [50]. In the Tosco process previously heated ceramic spheres are mixed with the shale, accomplish the decomposition of the kerogen, and are removed from the spent shale for reheating. These spheres could be heated by passing through the focus of a parabolic or trough-type concentrator before being mixed with the shale. Large scale feasibility of the Tosco process of 66,000 tons/day has been demonstrated with conventional heating of the spheres.
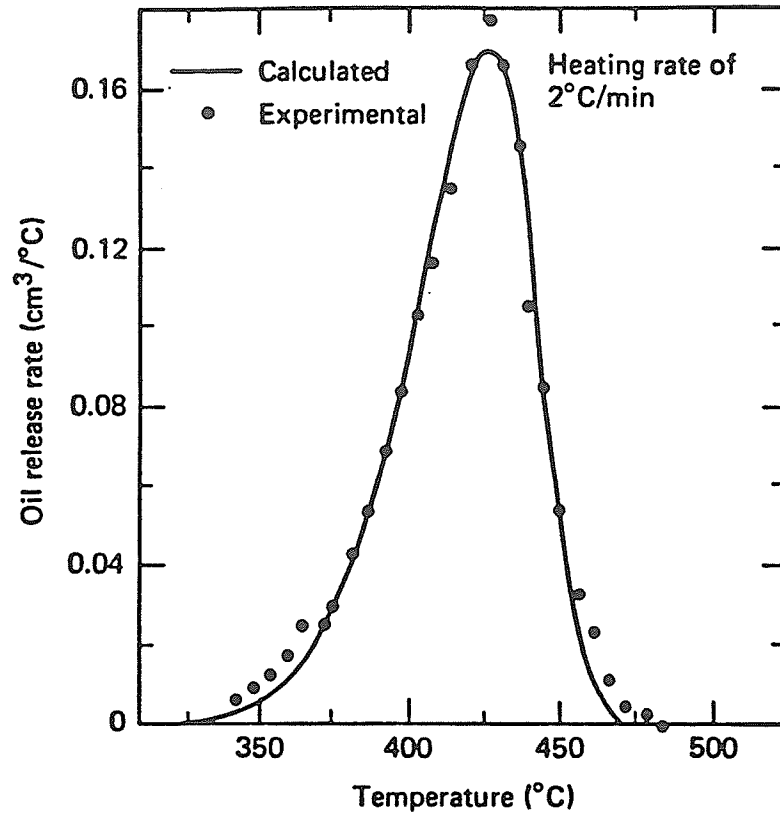
Figure 9.3 Oil release rate as a function of heating rate. [48]
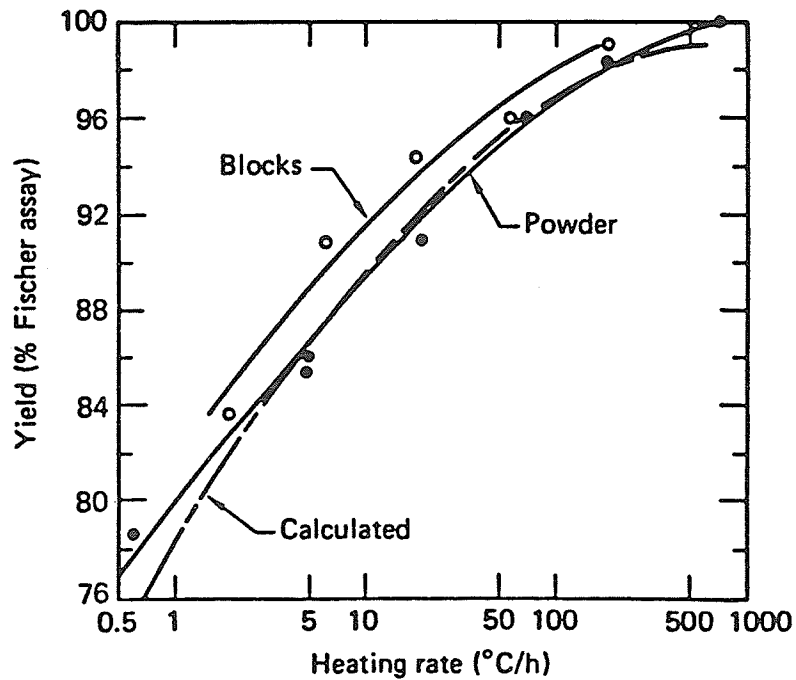
Figure 9.4 Oil yield as a functions of heating rate. [48] The high heating rates available with solar energy suggest its potential application to this process.

127

9.5 Radiatively Sustained Cesium Plasmas for Solar-Electric Conversion

This section describes a new type of solar energy converter, proposed at the University of Manitoba which converts solar energy directly to electricity. The spectral response of the collector is ideally matched to the spectral output from the sun.

In order to produce a high conversion efficiency one must generate high temperature working fluids, the upper limit of temperatures that may be generated will be limited by the temperature of the sun, i.e. approximately 5800 degrees Kelvin. For the working fluid to have a temperature close to this value, its nature will be that of a plasma. The energy contained within the plasma can be removed as electrical energy using a Magnetohydrodynamic (MHD) channel. The plasma must have an absorption spectrum well matched to the solar spectrum at the temperatures on interest (3000 - 5000 °K).

The work of Palmer and Dunning [51] has shown that cesium exhibits a large average photoionization cross section throughout the solar spectrum as shown in figure 9.5. Cesium also has important absorption bands in the red part of the solar spectrum as a result of cesium dimer transitions [52]. The dimer absorption cross-section extends from 600 nm to 1000 nm which is where the photoionization cross-section is beginning to fall off.

Palmer also developed a theoretical radiation energy balance model to investigate the limitations imposed by radiation losses, which form the major part of energy losses from the plasma. The results are shown in figure 9.6 from which it can be seen that to maintain a plasma temperature of
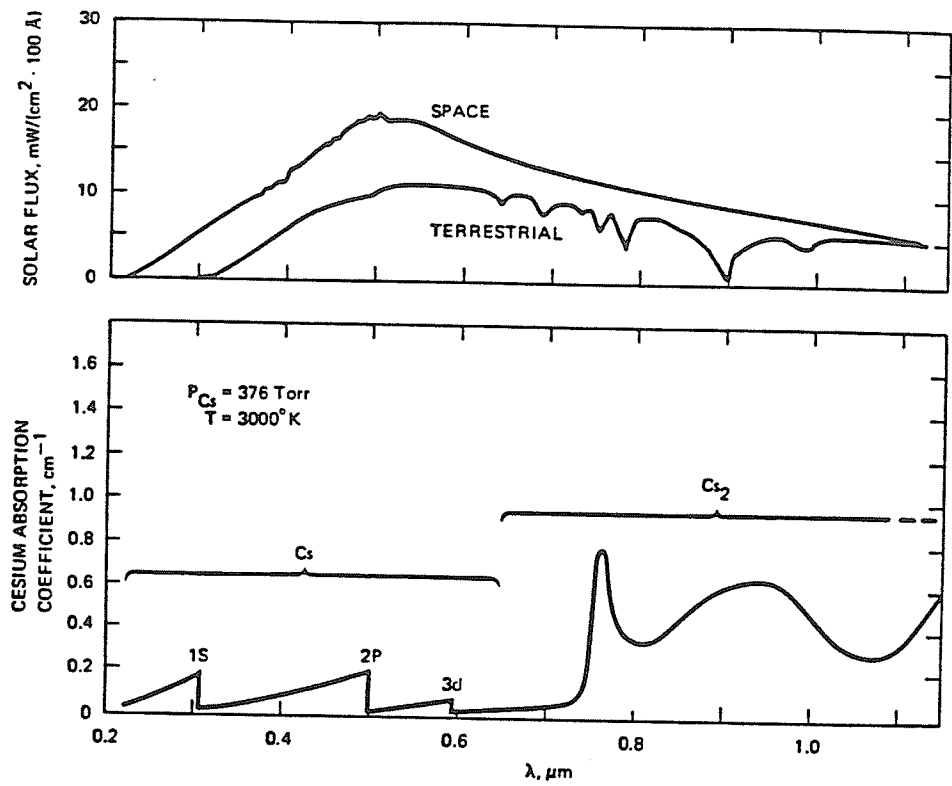
Figure 9.5 Spectral absorbtion bands of cesium vapour. [52] The absorbtion bands are well matched to the solar spectral distribution. The photoionization cross section begins to fall off at 600nm. The dimer absorbtion cross section then extends from 600 nm.
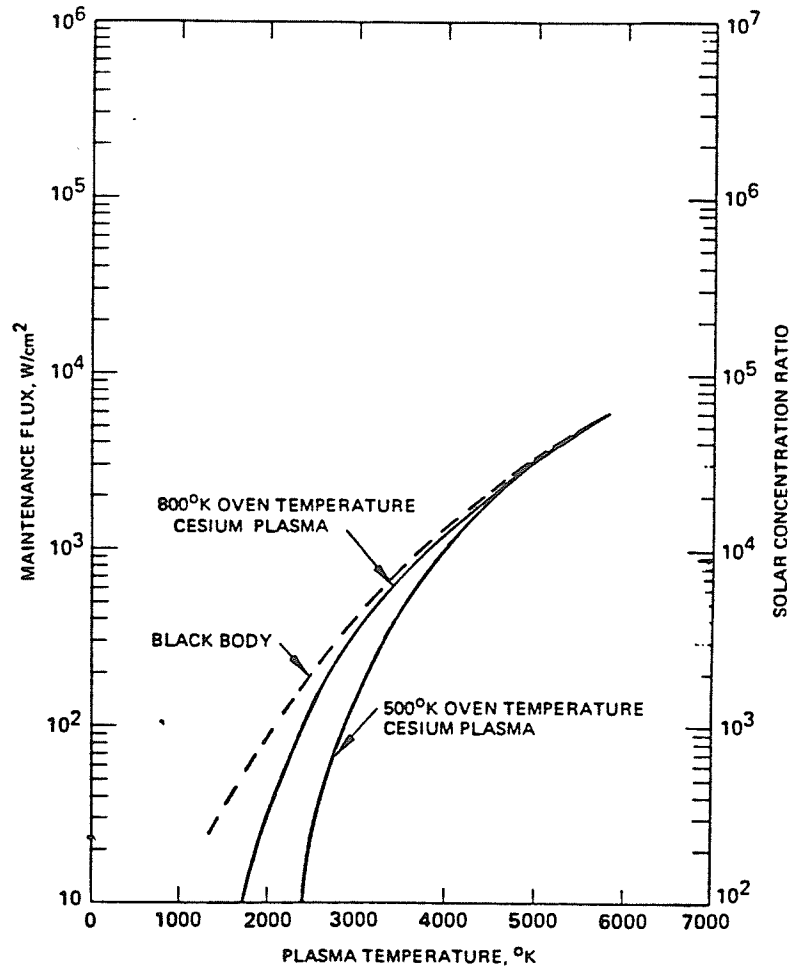
Figure 9.6 Radiation energy balance for cesium plasma. [51] To maintain a plasma temperature of 3000 °K requires a maintenance flux of the order of 100 W/cm². This flux level can easily be achieved with the concentrator system at the University of Manitoba.

3000 °K requires a maintenance flux of the order of 100 W/cm². This flux level can easily be achieved with the concentrator system at the University of Manitoba.

A type of solar electric converter using this technique is shown conceptually in figure 9.7. Cesium vapour is introduced into the focal volume of the concentrator. Within this volume the cesium vapour is heated to a temperature of approximately 3000 °K by absorption on dimer transitions and excited state photoionization transitions. At this temperature the plasma thermal energy is converted to translational energy by expansion of the plasma through a nozzle into a lower pressure region. The plasma flow energy is converted to electrical energy using a magnetohydrodynamic channel. The channel consists of a magnetic field of approximately 1 Tesla, arranged transversely to a pair of electrodes. The plasma flows through the channel, perpendicularly to the magnetic field and an electrical current is generated in the electrodes by the Faraday effect. Thus the plasma flow energy is converted to electrical energy via the $\vec{J}x\vec{B}$ forces on the plasma, where $\vec{B}$ is the magnetic field applied and $\vec{J}$ is the current density in the plasma. In this way energy can be removed from the plasma at a rate comparable to the loss of energy due to radiation. The plasma will remain conductive enough to extract electricity to a temperature of 1800 °K. After passing through the MHD channel the cesium vapour is recondensed at a temperature of 1000 °K and the molten cesium is returned to the focal region by a liquid metal pump. In this way the plasma serves as both the collector of solar radiation and the working fluid of the cycle.

Palmer and Dunning succeeded in generating a cesium plasma in a sealed enclosure with sapphire windows. The enclosure contained a small amount of cesium [53]. The theoretical model they developed to describe the

131
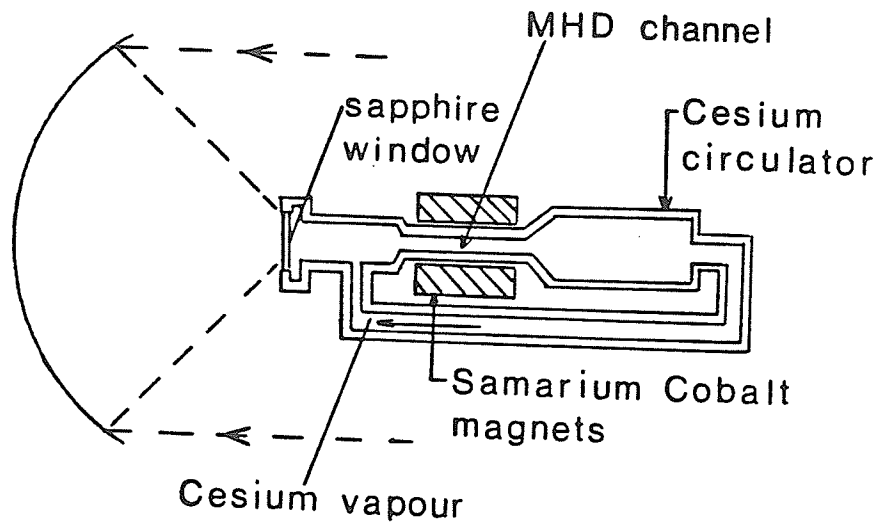
Figure 9.7 Conceptual solar electric converter using cesium plasma.

maintenance of a solar plasma predicts that a plasma temperature of 2800 °K can be reached by heating cesium vapour with sunlight concentrated to 300 W/cm². It is possible that such a measurement could be performed at the University of Manitoba.

The upper limit on the conversion efficiency of the above system would be determined by the Carnot efficiency to be approximately 60%. The efficiency of the MHD channel would reduce this. The efficiency of an MHD channel in this application is yet to be determined. Efficiencies of extraction of electricity of 48% have been reported with MHD systems involving an inert gas with a metallic seed such as lithium [54].

9.5.1   Liquid Metal MHD cycle

The condenser temperature of the proposed system is quite high (1000 °K) and it is most likely that the overall system efficiency can be increased by utilizing this heat also. Branover [55] has designed and built low temperature MHD solar-electric converters which are suitable for this purpose. In Branover's design, a room temperature liquid metal, for example mercury, or sodium-potassium alloy, is heated directly by solar radiation. A volatile liquid, for example Freon, is then injected into the hot metal, the two-phase flow so produced, flows through a magnetohydrodynamic channel and electrical currents are induced in the electrodes. The liquid metal provides the conductive medium and the expansion of the volatile substance provides the thrust through the MHD channel. After this process the two liquids are separated, the freon condensed and the process repeated. The efficiency claimed is 1.5 times that of a Rankine cycle engine operating between the same temperature limits. The overall electric energy output to solar energy input is

133

calculated to be 9%. The combination of the two MHD channels, one using a cesium plasma and the other a liquid metal, in a single energy conversion system, holds great promise in converting solar energy to electricity with high efficiency.

9.6   Summary

The investigation of the efficiency of extraction of electricity from a cesium plasma as it flows through a magnetohydrodynamic channel was proposed as the first phase of a project to be conducted at the University of Manitoba. The reviewing process was halted when the department of solar energy programs of NRC was closed.

The following chapter presents a discussion of the major conclusions of part I of this thesis.

Chapter 10

Major Conclusions and Summary of the Studies

The practicability of using highly efficient converters of solar energy as a viable alternate to more conventional resources is dependent on the availability and distribution of direct solar intensity across the surface of the earth. Accurate data which would yield these distributions is not currently available. Satellite based measuring systems will provide the spatial density of data required and these may be acquired over several years to yield representative values. Much work is required to produce algorithms which accurately correlate the direct intensity received at ground level with the reflected intensity received by the satellite.

By concentrating the incident direct intensity using a system of mirrors, high temperatures can be achieved which can be used in the design of high efficiency solar thermal converters. It has been shown that it is possible to receive less than 50% of the expected power at the focus of a concentrating mirror system due to surface distortions of the mirrors from ideal. This has been shown to be the case for a prototype converter testing arrangement that

may be regarded as being able to provide the power required for 1/10th scale energy conversion modules. In the system described in chapter 6, the concentrating mirror is 2.3 meters in diameter. Practical energy conversion systems are envisaged which would use much larger tracking parabolic mirrors of diameters in the range 6 to 10 meters, therefore the accuracy of figuring of the reflecting surface must be a prime factor in the concentrator design. Concentrating parabolic mirrors pressed from a single piece of stainless steel will not maintain their shape in high wind conditions. There are two possibilities to ensure that the concentrator remains accurately parabolic during its life. The first method as investigated by the General Electric Company involves constructing the mirror surface from 12 angular segments or "gores" [56]. Each segment is made from glass reinforced plastic and balsa sandwich panels which are injection moulded onto a parabolic contour. Rigidity is provided by ribs internal to the dish shape i.e ribs extend from the plane formed by the rim of the dish to the reflecting surface. In this way the stability of the figuring of the dish is ensured.

The second method involves a large frame of the diameter of the concentrator with several cross members to provide rigidity. Approximately one hundred independently adjustable small mirrors are attached to the frame. While illuminated by a heliostat each mirror is aligned so that the reflected beam strikes the focal area of the concentrator.

Of the two techniques the second will always yield the better figuring, however only the first method is practical in terms of mass production.

In each case the final figuring and its changes with ambient temperature and wind speed should be determined by optical ray tracing as described above.

The second design requirement in building the facility described above was

that the system should have a fixed focal region. For this reason a heliostat concentrator arrangement was adopted. Experience has shown that a single tracking parabolic concentrator would have been a better choice. The major problem which arose from using the heliostat was due to the obliquity effect which causes different amounts of the concentrator to be illuminated at different times during the day. This in turn would produce a varying total power at the focus during the day even when the incident direct sunlight intensity was essentially constant. A further problem encountered can be described be considering two points in time equally spaced from solar noon, for example two hours before and two hours after. Although the same area of the concentrator would have been illuminated, different regions of its surface would be involved. These regions would have different surface figuring accuracy which would in turn change the focal plane intensity profile in a way that could not be normalized.

By removing the heliostat completely the advantages gained would be illumination of the whole concentrator surface throughout the day, a longer time during the day when the concentrator could be used, and an increased concentration due to removal of the contribution of the heliostat figuring inaccuracies. These advantages will significantly outweigh the advantage of a stationary focal region.

A surprising conclusion from the laser scanning of the concentrating dish relates to the technique of coating concentrating mirrors with ECP91A reflective film. In an attempt to cover the whole dish with reflective film the wedge shaped pieces of film were overlapped along their edges. It was found that the light reflected from these edges did not reach the focal plane region and therefore represented lost power. The area covered by these overlapping strips represented 11% of the total area illuminated. In the process of apply-

ing the reflective surface to the concentrator it is therefore imperative that the edges of the reflective material do not overlap, as this can result in a decrease in the effective area of collection.

10.1   Summary of part1

A system has been constructed which will collect and concentrate solar intensity by a factor of 1500 times. The power delivered to the focal region is such that it may be used to test 1/10th scale prototypes of new forms of energy conversion devices which rely on highly focussed sunlight for their operation.

The system is currently the only one of its kind in Canada and the only one in North America which is situated outside the so called "sunbelt" states.

The parameters of the system have be accurately determined by measurement. A set of measurements has also been performed which characterizes the figuring accuracy of the reflecting surfaces. These parameters have been entered into a mathematical model which accurately predicts the power available and intensity distribution in the focal plane. The model may now be used to predict focal plane profiles during an experiment when an intensity distribution measurement cannot be performed. This is the first comparison of accurately measured focal plane intensity distributions with a theoretical model.

The intended next phase in the development of the solar energy facility was suspended due to lack of funding. It concerned the investigation of a new type of solar energy conversion device which consisted of a plasma of cesium sustained by solar radiation and a magnetohydrodynamic (MHD)

channel. The proposal was to investigate the generation of a cesium plasma using concentrated sunlight and to determine the efficiency with which energy could be extracted from the plasma as it flowed through an MHD channel.

Chapter 11

Introduction to part II

The ultimate structure of the nucleus may be determined by using intense beams of particles of very high energy as probes. The increase in energy of the particles used in these experiments has been accompanied by an increase is size of the machines which produce them.

Current projects will involve up to 10,000 magnets in their accelerator structure. The magnetic field produced by these magnets needs to be known more accurately than those used for earlier projects if the loss of beam due to collision with the walls of the vacuum vessel is to be minimized. The information needed to successfully operate these new machines can only be obtained if the magnetic field distribution of each magnet is known. This introduces a new logistical problem, if the measurement of each magnet takes of the order of one day and the measurements for all the magnets are required within a year, then 50 field mapping stations will be required.

The techniques used for magnetic field measurement have change little since the 1970's, however the major advances made in the fields of instrumentation, data acquisition and data logging using computers can be used together to meet the measurement requirements of these new machines.

There is therefore the need to develop a completely automatic, computer controlled magnetic field measurement and analysis system which at the same time must cost a fraction of current systems. Such a system has been designed and constructed in the Department of Physics at the University of Manitoba. The system controls the field mapping process, records and analyzes the data completely automatically. All functions of the system are controlled by a single IBM XT microcomputer. The system is described in detail in this part of the thesis.

In order to introduce the subject, chapter 12 traces the development of accelerating machines from the Cockroft Walton accelerator through to the present day machines. The concept of focussing, using quadrupole magnets is introduced in chapter 13. These magnets are fundamental to the operation of synchrotron accelerators and fixed energy beam transport lines.

The focussing properties of quadrupole magnets need to be accurately known in order that the behaviour of the accelerated beam may be predicted using beam transport computer codes. These codes require representative parameters of the field as input. An analysis of the quadrupole field is presented from which the representative parameters of effective length and harmonic content are identified.

To provide the parameters the beam transport codes require, measurements of the magnetic field must be performed. Chapter 14 describes those devices which measure magnetic fields and from which the required data may be derived.

Chapter 15 describes a computer controlled automatic field measurement and analysis system designed and built at the University of Manitoba. The system measures the representative parameters of the field produced by

quadrupole magnets. The mechanical, electrical, hardware interfacing, programming and automatic operation details of the system are described.

The analysis of the field data yields the requisite parameters which may be entered into beam transport codes. The field data and analysis for a quadrupole magnet used as an element in a proton microprobe arrangement is presented in chapter 16.

Chapter 12

Accelerator Development -Overview

12.1   Introduction

The ultimate structure of the nucleus may be determined by using intense beams of particles of very high energy as probes. The energy available from the earliest accelerating devices, which were of the electrostatic type (Cockroft -Walton and Van de Graaf) was limited by breakdown resistance of the accelerating tube materials to an upper energy of approximately 15 MeV. The energy of accelerated particles was increased beyond this using combinations of electric and magnetic fields. The Lawrence cyclotron [57] accelerated particles by constraining them, in a dipole magnetic field, to circular orbits of ever increasing radius as radio frequency accelerating power was applied between two D-shaped accelerating electrodes. The upper energy limit of the particles accelerated by this scheme was approximately 40 MeV. The energy limit was set by the relativistic mass increase of the particles so that they no longer received an accelerating pulse from the R.F. field at the largest radii of motion i.e. their increased mass had caused them to become out of phase with the accelerating voltage.

This difficulty was overcome by sweeping the frequency of the applied R.F. field from higher to lower frequencies as the particles increased in energy and mass, hence the name synchrocyclotron. This resulted in a pulsed beam output. Another solution was to vary azimuthally the magnetic field through which the particle passed, as a function of radius. This method resulted in a continuous beam output. By these methods the upper energy limit of the accelerated particles was increased to approximately 600 MeV [57]. This method was limited by the size and cost of the vacuum vessel and the magnet.

A further increase in the energy to which particles could be accelerated was provided by the alternating gradient synchrotron where the single large dipole magnet used in a cyclotron is replaced by many smaller magnets. These magnets surround an evacuated beam tube through which the particles pass. The beam tube is in the shape of a taurus of large circumference. Radio frequency cavities are interlaced with the magnets, these accelerate the particles on each revolution [58]. The magnets have poles shaped such that the magnetic field increases with radial distance. The magnets are arranged so that in successive sections of the accelerator the gradient is first towards the center of the taurus and then away from it. The field can thus be regarded as having an alternating gradient which results in strong focussing and defocusing of the accelerated beam of particles. The effect of this is to smooth out the deviations the particles make from the (ideal) circular path. The alternating gradient synchrotron is the basis of operation of the largest machines operating today.

As the intensity of beams in new accelerators increased by orders of magnitude, it became desirable to compensate for the defocusing force due to the space charge between particles, so as to reduce the beam "spill" i.e that part of the beam which strikes the walls of the vacuum vessel, to very low levels.

In 1952 while investigating the possibility of new types of accelerators, Courant and Livingston [58] proposed the use of a new type of magnetic lens containing four poles, to focus the beams of rapid ions in the alternating gradient synchrotron. For a given particle energy the quadrupole lenses have a stronger ability to converge the beam than do solenoidal lenses.

The action of the quadrupole in focussing particles so that they are transported through the accelerator structure without loss, (for example low energy beams between the injecting section and the main ring, or the high energy beams from the accelerator along beam lines to the target areas), becomes one of the most important aspects of the machine as a whole.

The focussing action of the quadrupole lens is described in the following chapter. A harmonic expansion of the field in the aperture of the magnet yields parameters which characterize the focussing. These parameters may be entered in beam optics codes to predict the behaviour of the beam in this accelerator.

Chapter 13

Focussing Properties of a Quadrupole Magnet

13.1 Introduction

The focussing action of a quadrupole magnet is of fundamental importance to the successful operation of synchrotron machines and fixed energy beam transport systems. This chapter describes the focussing action and presents an analysis of the quadrupole field. The analysis yields a series of harmonic coefficients which characterize the quality of the field. These coefficients may then be measured by a suitable field mapping system.

13.2 Focussing Action

Consider the situation shown in figure 13.1. [59] where a beam of particles passes through a single quadrupole magnet. The profile of the beam is arranged so that it is a narrow slit in the x direction. For the beam to be focussed at point F, a particle moving parallel to the axis at a

146
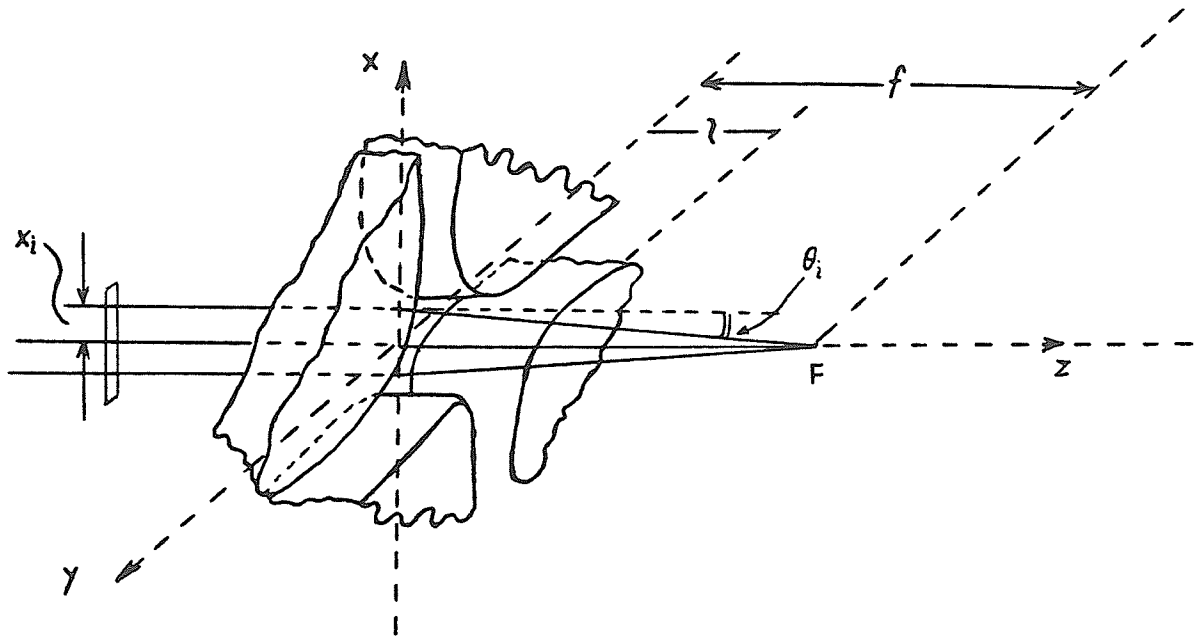
Figure 13.1 Quadupole focussing action. [59]

displacement x_i must be displaced through an angle θ_i which is proportional to the distance x_i. As first proposed by Courant and Livingston [60], this can be accomplished by arranging for the magnetic field in the aperture to have a constant gradient along the x and y axes, i.e $\vec{B} = k\vec{r}$ where $r^2 = x^2 + y^2$, this in turn leads to a Lorentz force on the charged particles proportional to x_i as required.

The action of the field on particles travelling at a small displacement in the y direction out of the Ozx plane is a defocusing action, another quadrupole lens following the first and rotated through 90 degrees around the beam axis will provide focussing in the Oy plane and defocusing in the Ox plane. The net action of the two lenses separated by a distance d is focussing in both planes as shown in figure 13.2 [60]. It will be shown next that the cross-sectional pole shape required for producing a magnetic field with a constant field gradient in the aperture is that of a hyperbola.

13.3 Quadrupole Magnetic Field

The representation of the field as a function of a complex variable $z = x + iy$ will lead to the representation of the magnetic field as a harmonic series. The coefficients of the series represent the multipole components of the field. The multipole coefficients can be independently measured with magnetic induction type measuring coils of the appropriate geometry.

Consider Maxwell's equation:

$$\nabla \cdot \vec{B} = 0 \qquad (13.1)$$

If one assumes no z dependence of the field (cylindrical symmetry) within

148
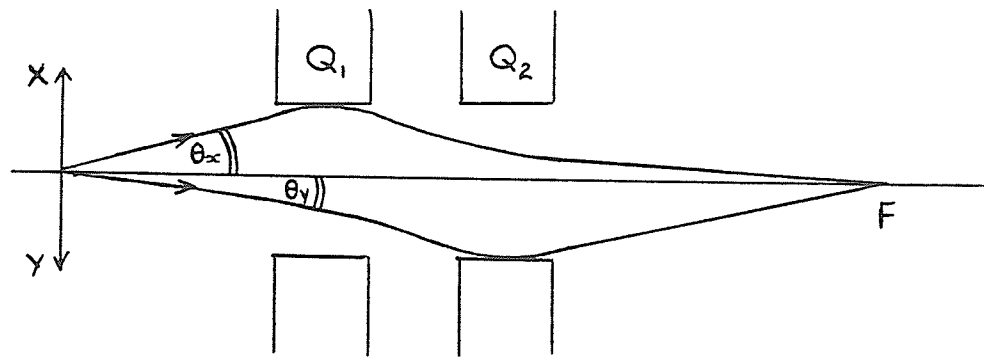
Figure 13.2 Net focussing action of a pair of quadrupoles. [66]

the aperture of the magnet, the above may be written in two dimensions as:

$$\frac{\partial}{\partial x}B_x + \frac{\partial}{\partial y}B_y = 0 \qquad (13.2)$$

This equation will be satisfied by either:

$$\vec{B} = \nabla x \vec{A} \qquad (13.3)$$

or

$$\vec{B} = \nabla U \qquad (13.4)$$

where $\vec{A}$ is the magnetic vector potential and U is the magnetostatic scalar potential. The components of $\vec{B}$ may be written as either:

$$B_x = \frac{\partial \vec{A}}{\partial y} = -\frac{\partial U}{\partial x} \qquad (13.5)$$

$$B_y = -\frac{\partial \vec{A}}{\partial x} = -\frac{\partial U}{\partial y} \qquad (13.6)$$

The relations between $\vec{A}$ and U are the same as the Cauchy-Reimann conditions for a complex function:

$$F(z) = \vec{A} + iU \qquad (13.7)$$

where $F(z)$ is the complex potential. If one defines a complex magnetic induction function [1] by:

---

[1]Note: * denotes complex conjugation.

$$B(z) = B_x + iB_y \qquad (13.8)$$

then

$$B^*(z) = \frac{\partial F}{\partial z} \qquad (13.9)$$

and

$$B_x = Im\left(-\frac{\partial F}{\partial z}\right) \qquad (13.10)$$

$$B_y = Re\left(-\frac{\partial F}{\partial z}\right) \qquad (13.11)$$

It is possible to expand $F(z)$ as a power series: [61]

$$F(z) = \sum_{n=1}^{\infty} \frac{1}{n}(a_n + ib_n)z^n \qquad (13.12)$$

The most general fields can be solved for by evaluating the coefficients a_n and b_n. When the field has certain symmetries, many of the coefficients become zero. Consider figure 13.3(e), both the x-z and y-z planes are planes of antisymmetry which place the following conditions on the potential function:

$$F(z) = F(-z) \qquad (13.13)$$

$$F^*(z) = F(-z^*) \qquad (13.14)$$

These equations require that all the coefficients b_n vanish and only those coefficients a_n, with n even, are non zero.
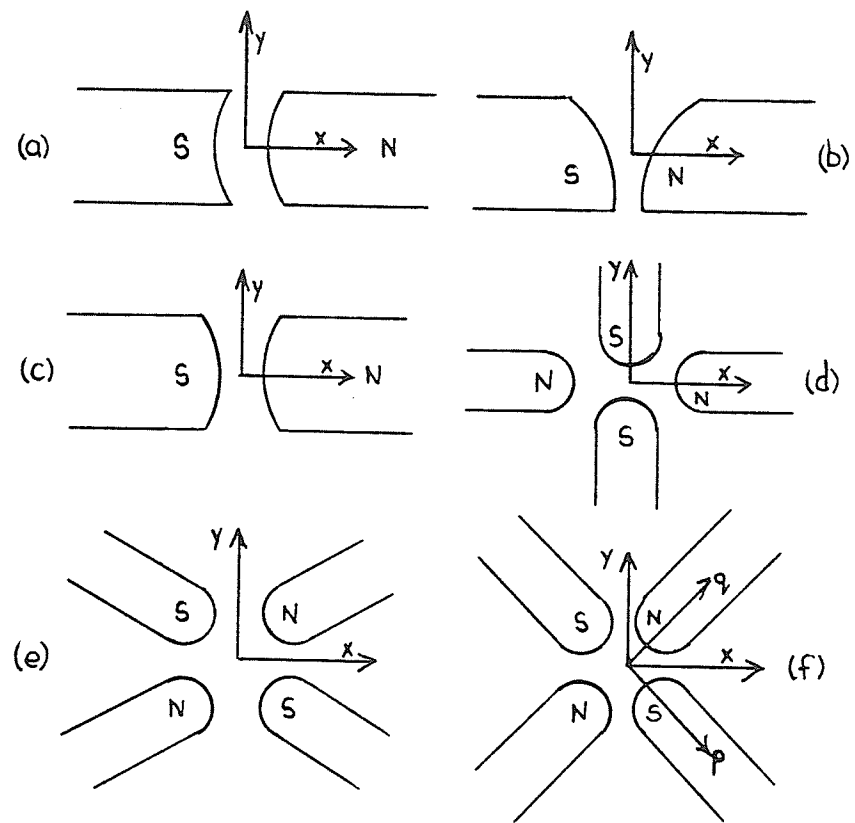
Figure 13.3 Symmetry planes. [61]

In addition, the planes p-z and q-z are planes of symmetry (figure 13.3(f)) which places the further condition on the potential:

$$F(z) = -F(iz) \tag{13.15}$$

and only the values of a_n for which $i^n = -1$ are non zero. The complex potential for the symmetrical quadrupole magnet therefore has the form:

$$F(z) = \frac{1}{2}a_2\,z^2 + \frac{1}{6}a_6\,z^6 + \frac{1}{10}a_{10}\,z^{10} + \cdots \tag{13.16}$$

Differentiating and using (13.10) and (13.11):

$$\frac{\partial F}{\partial z} = a_2\,z + a_6\,z^5 + a_{10}\,z^9 + \cdots \tag{13.17}$$

$$B_x = Im\left(-\frac{\partial F}{\partial z}\right) = -a_2 y - a_6\left[y\left(x^4 + y^4 - 6x^2 y^2\right) + 4x\left(xy\right)\left(x^2 - y^2\right)\right] + \ldots \tag{13.18}$$

$$B_y = Re\left(-\frac{\partial F}{\partial z}\right) = -a_2 x - a_6\left[x\left(x^4 + y^4 - 6x^2 y^2\right) - 4y\left(xy\right)\left(x^2 - y^2\right)\right] + \ldots \tag{13.19}$$

The required constant field gradient is met if the coefficients $a_6, a_{10}\ldots$ are all zero. In this case the expression for $F(z)$ becomes:-

$$F(z) = \frac{1}{2}a_2\,z^2 \tag{13.20}$$

The required pole shape will be given by considering the magnetic scalar potential $U(x,y)$:

153

$$U(x, y) = Im\,(F(z)) = a_2\,xy \qquad\qquad (13.21)$$

The required field will therefore be produced by equipotential hyperbolic pole pieces of infinite extent with the axes ox and oy as asymptotes. The ideal shape is impossible to realise in practice as the magnet poles will be of finite length, further, space has to be made for the magnet electrical coils. As a result of this departure from the ideal case the higher order coefficients in (13.16) exist.

13.4 Origin of Multipole Components

Consider the practical quadrupole shown in figure 13.4. The pole tips have the hyperbolic shape required. Assume the construction is mechanically perfect i.e. A = B = 2R and a = b = c = d and that the poles are symmetrical about their center lines. The hyperbolic shape is truncated to allow space for the coils. Consider the pole in the first quadrant. At the point of truncation the field of the pole is slightly reduced due to leakage flux beyond the point and due to saturation of the pole at the point. This can be represented as a virtual South pole superimposed on the North pole field. The result of this is that each physical pole can be thought of as three effective poles, the result for the magnet as a whole is the introduction of a duodecapole or 12-pole component.

If the pole shape is made using a circular cross section other higher multipoles will be present in the magnet. Each multipole will have an odd number of poles in each quadrant, i.e multipoles $4(2m + 1)$ m=0,1,2 ... will be introduced. The higher order multipoles that may therefore be introduced
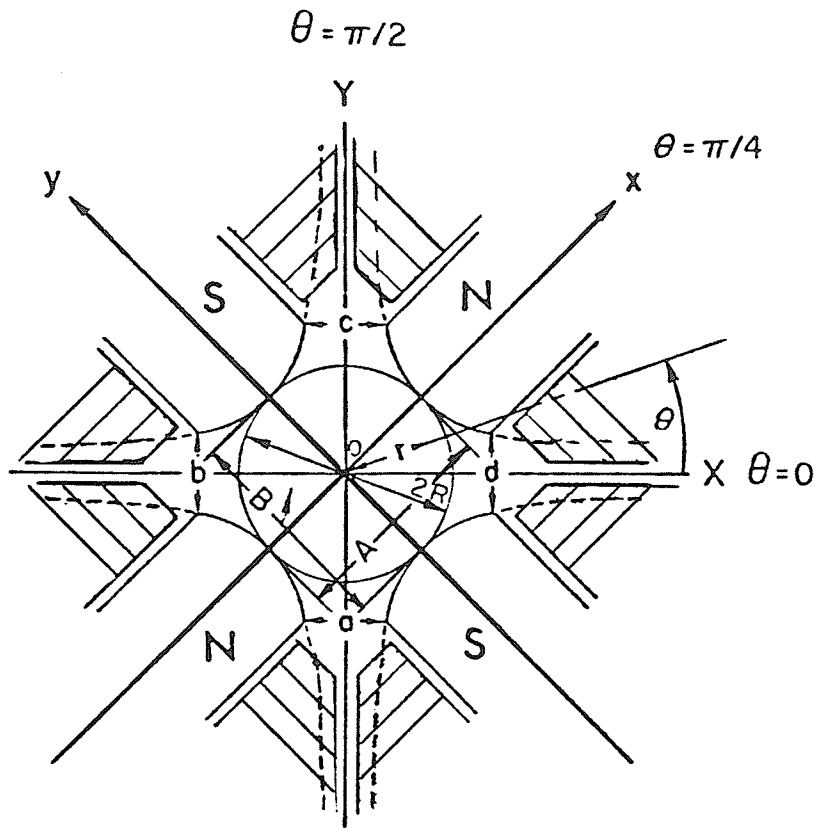
Figure 13.4 Practical Quadrupole.
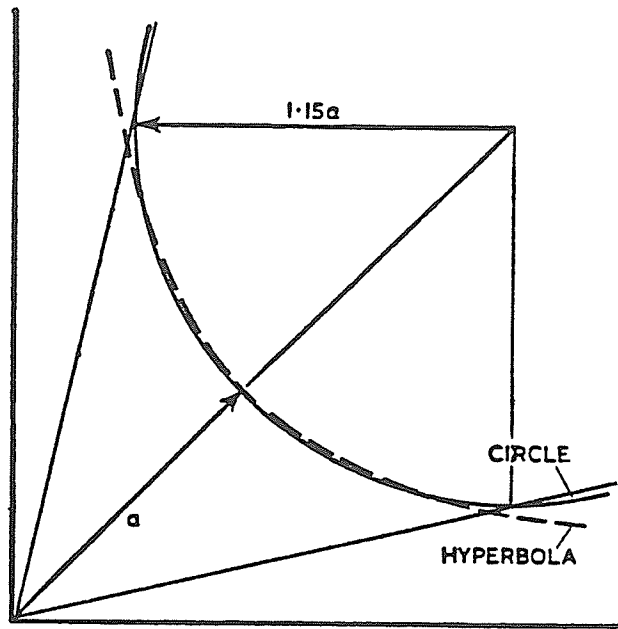
Theoretical hyperbolic pole and the optimum radius cylindrical approximation.

Figure 13.5 "Banford" pole face shape. [62]

when the mechanical construction is perfect are 12 pole, 20 pole, 28 pole etc.

In practice hyperbolic poles are difficult to produce and the pole contours are machined in cross section as arcs of circles. By choosing the ratio $\frac{R}{A}$ =1.15, [62] where R is the radius of the circle which represents the pole shape and A is the radius of the aperture of the magnet, (see figure 13.5) the 12 pole component can be cancelled completely. The amount of cancellation at a particular radius will also be a function of the width of the pole [63]. If mechanical symmetry is not maintained then other terms enter into the field which do not have the quadrupole symmetry. For example in the case of radial displacement of two opposite poles so that a = b = c = d but A $\neq$ B the orders introduced are octupole, 16 pole, or in general n = (4t) t = 1,2,3 etc [64]. The octupole perturbation may also be produced by an asymmetry such that A = B, a = d, and b = c but a $\neq$ b.

In the case of misalignments of the pole pieces which have no symmetry, for example the azimuthal displacement of a single pole piece, then the set of multipoles corresponding to dipole, sextupole, 14 pole, 18 pole etc are introduced. i.e n = (4t $\pm$ 1) for t = 1,2,3 etc

The harmonic components of the field characterize the quality of the focussing action, a perfect quadrupole would have a fundamental component only. In practice the harmonic content of the field may only be determined by direct measurement. The following chapter describes the current techniques used in measuring magnetic fields.

Chapter 14

Magnetic Field Measurement Techniques

14.1   Introduction

For high energy spectrometer work an analysis of trajectories of charged particles requires a detailed point by point magnetic field map throughout the volume of interest. However for beam line transportation elements like quadrupole and sextupole magnets, useful information is provided by making measurements which integrate along the length of the element and describe its field characteristics in terms of a harmonic expansion. Integrating measurements also define the useful aperture of the magnet. In this chapter the basic types of devices for measuring magnetic fields and their theory of operation will be described, this will be followed by a description of the application of the fluxmeter type of device to the measurement of the magnetic field of a quadrupole magnet.

14.2   Nuclear Magnetic Resonance

If a charged particle with angular momentum $\vec{p}$ is placed in a constant magnetic field $\vec{B}_o$ the magnetic moment vector $\vec{\mu}$ of the particle becomes oriented with respect to $\vec{B}_o$ The vectors $\vec{\mu}$ and $\vec{p}$ are proportional through $\vec{\mu} = \gamma\, \vec{p}$ where γ is the gyromagnetic ratio of the particle.

This orientation can only be such that the component of $\vec{p}$ along $\vec{B}_o$ is $\frac{mh}{2\pi}$ where m is an integer given by m $= \pm$(I-K) where I is the spin of the particle and K is any integer smaller than or equal to I.

To each orientation there corresponds a different energy level. For protons, I $= 1/2$ and therefore there are two possible energy levels whose difference is given by:

$$\Delta E = \frac{B_0 \gamma h}{2\pi} \qquad (14.1)$$

If a sample containing protons is energized at energy ΔE, this energy can be absorbed by the particles in the sample. The principle is to determine the frequency corresponding to resonance which will be directly proportional to the field $\vec{B}_o$ The proportionality constant is equal to 4.2577 Mhz/kGauss for protons, and 0.6359 Mhz/kGauss for deuterons.

This forms the basis of an absolute method of measuring magnetic fields that can be made with an accuracy of 1 part in 10^6

The technique was first introduced in 1946. A sample containing many protons (for example distilled water, H_2O or heavy water D_2O) has a radio frequency coil wrapped around it as shown in figure 14.1, the axis of the coil is arranged perpendicularly to the magnetic field to be measured. The frequency of RF power in this coil is adjusted so that the protons are excited
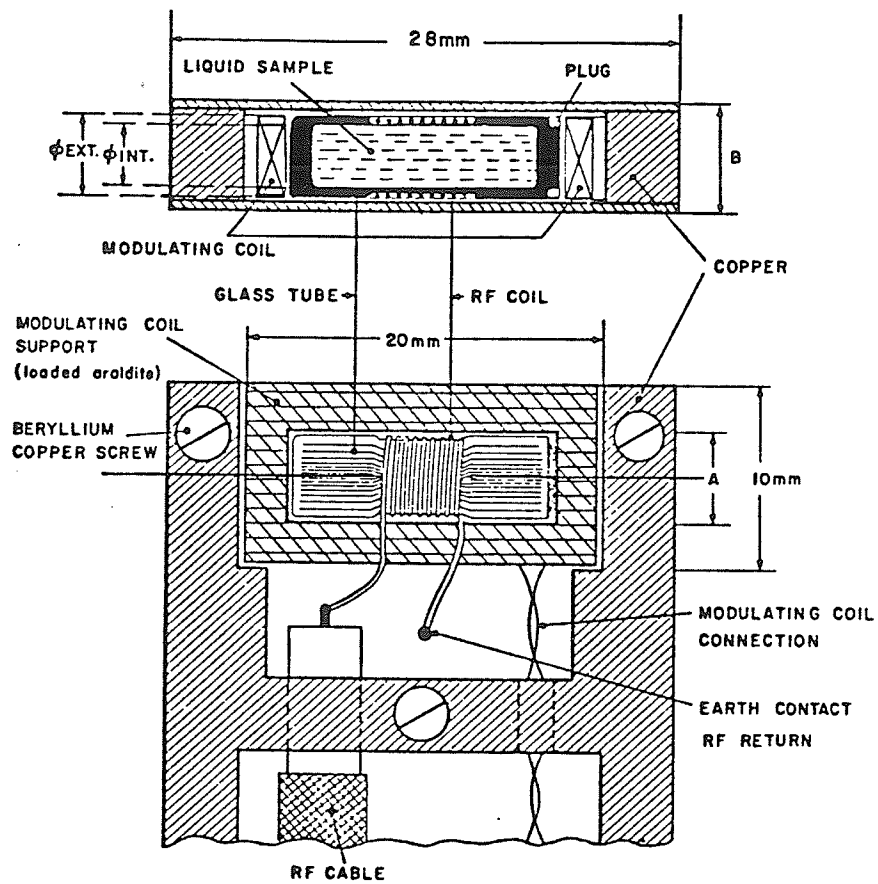
Figure 14.1 Nuclear Magnetic Resonance Probe Head. [65]

to an increase in energy ΔE. A second coil at right angles to the first, (to reduce the effects of inductive coupling between them), detects signals as the particles return to their equilibrium condition.

For observing the resonance signal, the resonance conditions are crossed by varying the electromagnetic wave frequency, or by varying the local magnetic field intensity using a small a.c coil surrounding the volume of the sample.

The range of the technique is from 10^{-2} Tesla to the highest fields that can be generated, the lower limit being set by loss of the NMR signal in electronic noise.

To accurately determine the NMR resonant frequency, the magnetic field must be constant over the volume of the sample, fields with a gradient over the volume of the detector head result in widening of the resonance peak and a reduction in its amplitude. Hence the technique is not applicable to regions containing strong field gradients.

14.3   Hall Effect

Consider a strip of material carrying current in the direction Ox as shown in figure 14.2. If a magnetic field is placed along the direction Oz, then a potential difference will appear between electrodes attached to the material in the direction Oy. This effect was discovered in 1879 by Hall and its origin is as follows, the charge carriers flowing in the strip feel a Lorentz force which forces them to build up on the electrodes on the sides of the strip perpendicular to Oy generating an electric field in the direction Oy. At equilibrium there is no net charge carrier flow in the Oy direction due to the balancing of the Lorentz force by the force due to the Hall field.
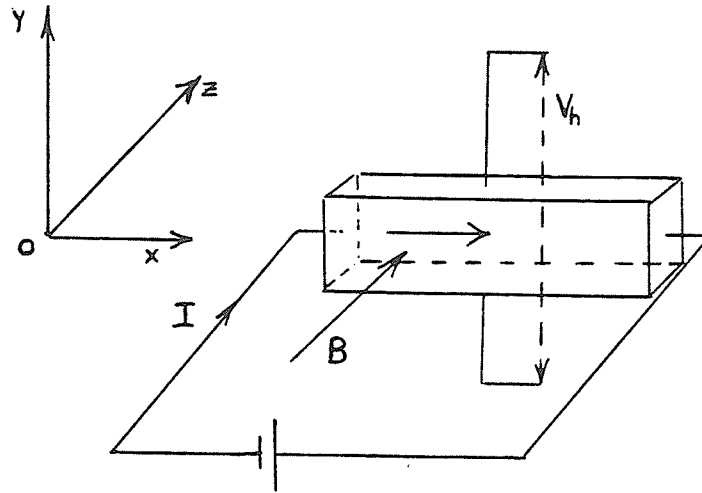
Figure 14.2 Hall Effect.
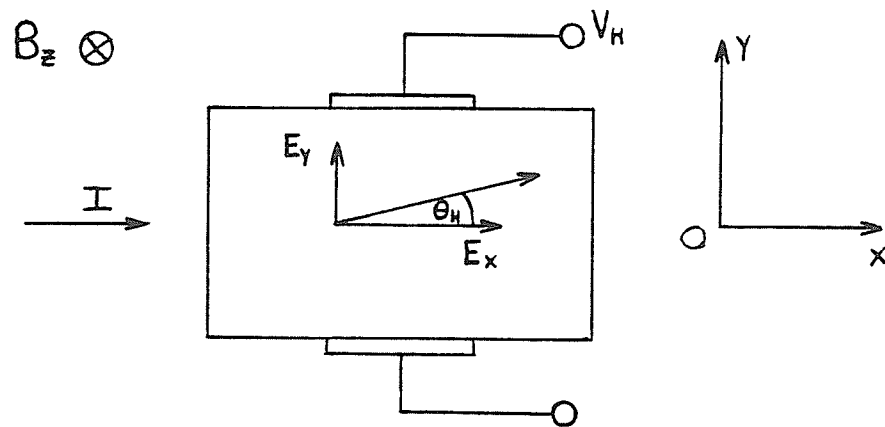
Figure 14.3 Hall Angle θ_H

The Hall voltage is given by:

$$V_H = k_1 B_z I \tag{14.2}$$

$$= \frac{R_H}{\rho} V B \frac{l_y}{l_x} \tag{14.3}$$

Where R_H is the Hall coefficient, V is the applied voltage along the strip, B is the applied magnetic field, ρ is the resistivity of the material of the strip and l_x, l_y, and l_z are the dimensions of the strip.

In a steady B_z field, the electric fields E_x (the applied field causing the current flow) and E_y (the field due to the Hall voltage) produce a net field at an angle θ_H to the x direction, this is known as the Hall angle as shown in figure 14.3.

For a given magnetic field and applied voltage, the Hall voltage is proportional to R_H/ρ. It is therefore important to use a material with a large value of R_H/ρ . This ratio has the value 0.003 for copper which is characteristic of the very small values for the Hall voltage for ordinary metals.

The method has been used widely since 1953 when suitable semiconductor materials were developed. For example for InAs, R_H/ρ =2.0 [65]

In n-type extrinsic semiconductors the Hall coefficient is related to the majority charge carrier density (e_n) by: [66]

$$R_H = \frac{3\pi}{8} \frac{1}{e_n} \tag{14.4}$$

since the density of charge carriers is related to the temperature of the semiconductor, the Hall coefficient is also temperature dependent. The resistivity of the semiconductor is dependent on the magnetic field due to the magnetoresistive effect. In general therefore the Hall voltage will be dependent on

temperature and magnetic field intensity.

14.3.1 Planar Hall Effect

In regions of a magnetic field where there is a component of the field in the plane of the Hall plate, for example in the fringing field of magnets, an extra term appears in the expression for the Hall voltage:

$$V_H = k_1 B_z I + k_2 B_\parallel^2 \sin(2\psi) I \qquad (14.5)$$

Where $B_\parallel$ is the component of the field in the plane of the Hall plate. The component makes an angle ψ with the current direction as shown in figure 14.4. This effect is known as the planar Hall effect, and can lead to errors in the measurement of inhomogeneous fields. The effect has a maximum value for $\psi = \pi/4$, $3\pi/4$ ... and disappears for $\psi = 0$, $\pi/2$, π, ... [67]

14.3.2 Practical Hall probes

The response of a Hall plate to a magnetic field consists of the transverse and planar Hall effects, the magnetoresistance effect, and the variation in these effects with temperature. The dependance on temperature of the Hall coefficient can be reduced by doping the semiconductor so that the majority carriers present in the device are due to the presence of the dopant (extrinsic conduction) in this case the temperature dependance of the density of charge carriers is less than that for intrinsic semiconductors. The magnetoresistive effects can be overcome by using a constant current source to provide the current through the device.

The sensitivity to $B_\parallel$ can be reduced by increasing the ratio of the length of

the Hall probe to its width i.e. the ratio (a/b) as shown in figure 14.4, and by decreasing the ratio of the electrode length to the length of the Hall plate i.e the ratio (s/a). This results in a "cross" type Hall probe [68].

With a knowledge of these effects, the magnetic field value may be determined from the Hall probe output alone, the output from a thermistor, fixed to the Hall probe may be used to record the temperature for correction of temperature dependent effects. The measurement accuracy can be of the order of 1 part in 10^3.

In practice Hall plates are usually calibrated in homogeneous fields where the field value is simultaneously measured using a NMR probe at various magnetic field intensities. A curve is fitted between the discrete data points using a spline fitting function for example. In this way a Hall probe assembly can be calibrated to an accuracy of 1 part in 10^4.

14.4   Induction Law

The electromotive force induced in a coil when the magnetic flux that links it varies is given by the Faraday induction law:

$$e = -\frac{\mathrm{d}\phi}{\mathrm{d}t} \tag{14.6}$$

This forms the basis of a variety of methods for measuring magnetic fields which have the advantage that there is practically no limit to the field that can be measured. Devices based on this law are known as fluxmeters.

To make point measurements small rotating coils can be used. A small coil of wire rotates at an angular velocity ω with its axis of rotation perpendicular to the direction of the field. The coil output is read from a slip ring arrangement.
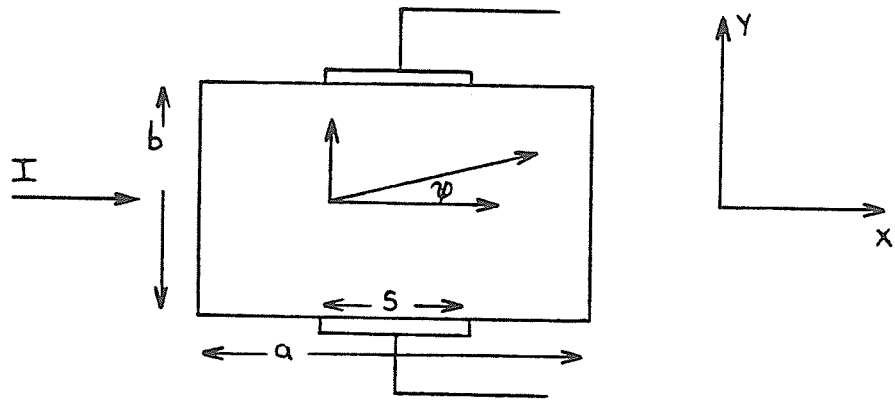
Figure 14.4 Planar Hall Effect.

It is an alternating signal of amplitude V_o given by:

$$V_o = NS\omega B_n \tag{14.7}$$

where NS is the product of the number of turns and the area of each coil and B_n is the component of the field perpendicular to the axis of rotation.

The accuracy of measurements made with this technique is less than that available by the NMR technique but may exceed that of Hall probes. The field integral $\int B_n dl$ where B_n is the component of the field normal to the plane containing the line along which the integral is required, can be measured by a single long coil passing through the magnet. Two of these long coils placed side by side and wired so that their outputs oppose each other can be used to determine the field gradient in the magnet aperture. The harmonic components of the field may be determined from the signal induced in a rotating coil wound on the surface of an insulating cylinder. The signal may then be Fourier analyzed and the amplitudes of the peaks in the frequency spectrum related to the multipole components. The harmonic content of the field then indicates the quality of the focusing magnets. This measurement technique, and signal analysis are described in the following chapters.

14.5   Comparison of the techniques

The techniques described above form the basis of modern magnetic field mapping technology, having displaced older techniques such as peaking strips, ballistic galvanometers, and floating wires [59]. The range of measurement and accuracy of each technique is summarized in figure 14.5.[69].

Hall probes may also be used to investigate harmonic components and
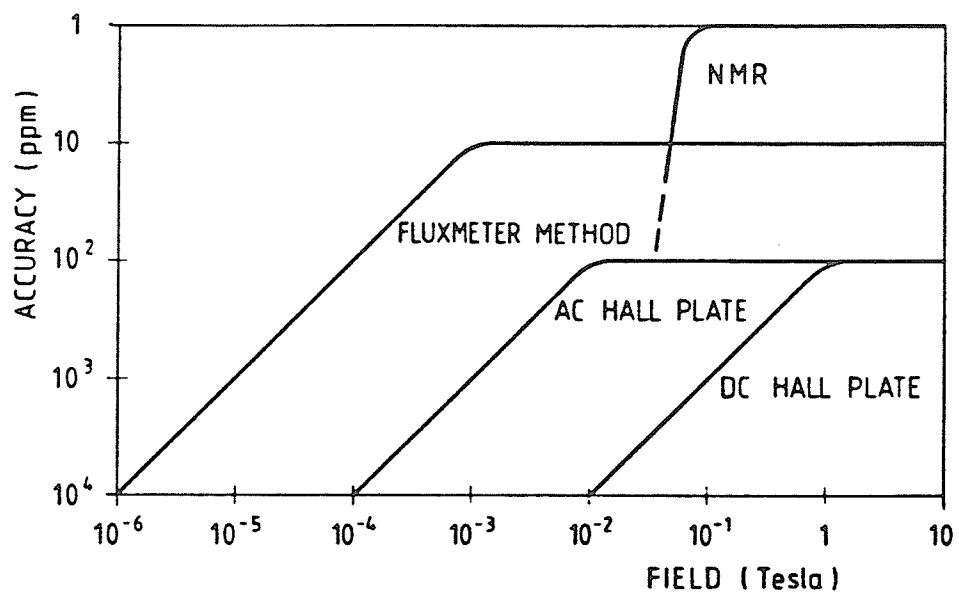
Figure 14.5 Accuracy and range of field measurement techniques [69]

differential field components on a point by point basis within magnet apertures.

In the case of differential field measurement two Hall probes are placed a set distance apart and moved through the magnet aperture. The signal from each probe is read out through a switching box and the difference calculated [70]. The disadvantage of this technique is that for low gradient fields the combined error in the two field readings may be comparable to the field difference itself. The effective field length of a magnet, described in chapter 16, may be determined by the integration of point by point measurements, however, the combination of errors may again be significant. With the long coil technique, there is direct measurement of the difference between the two fields, integrated over the length of the magnet.

The harmonic component of multipole magnets may be evaluated on a point by point basis using Hall probe techniques. A Hall probe is mounted on a cylinder so that its surface normal is always tangential to the cylinder surface, as shown in figure 14.6. As the cylinder rotates, measurements are taken of the Hall voltage. The recorded voltage output is later expanded as a Fourier series whose coefficients can be related to the harmonic components. It has been shown that in the fringe field of a magnet, where a significant B_z component is present, [1] or if the axis around which the Hall plate rotates does not coincide with the magnetic axis of the magnet, then false harmonics can be generated [71]. At the 1983 International Magnet Measurement Workshop it was decided that a "standard quadrupole" magnet would be circulated around the laboratories in order to compare the results of harmonic measurement techniques. Rotating coil fluxmeter equipment gave close agreement in measuring integrated harmonics, whereas Hall

---

[1]The z direction is the axial (beam) direction of the magnet.
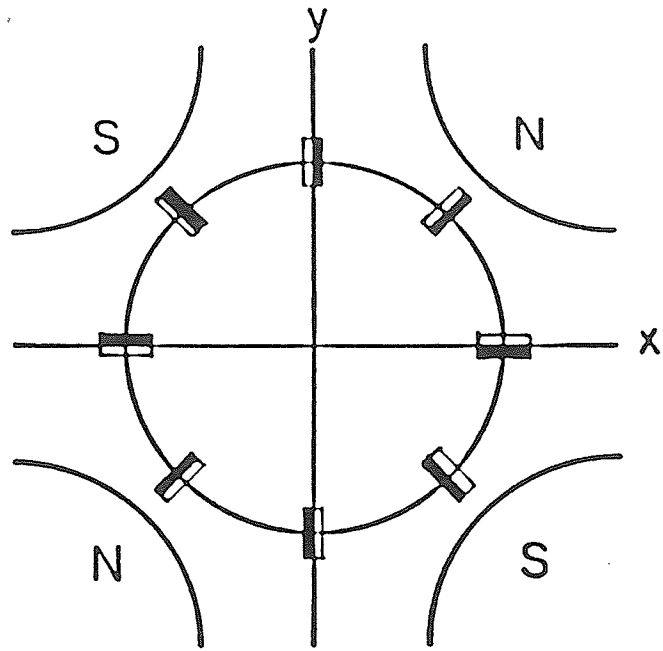
Figure 14.6 Hall probe arrangement to measure harmonic coefficients. [71]

probe equipment gave discrepancies of almost an order of magnitude in the determination of some harmonic components [72].

14.6 Conclusions

The types of devices currently used to measure magnetic fields have changed little sine the 1970's. However major advances have been made in the areas of computers,data acquisition and data logging. As the number of magnets involved in new machines grows and the required accuracy of measured field data for these magnets becomes more critical, new systems must be developed to accommodate these changes. A system which measures the field data for quadrupole magnets is described in the following chapter.

Chapter 15

A Computer Controlled Field
Mapping System

15.1 Introduction

This chapter describes a computer controlled field measuring system designed
to measure the key parameters of quadrupole magnets, i.e useful aperture,
effective length and harmonic content. A description will be given of each
component of the system, and how they work together to map out the mag-
netic field.

15.2 Field Measuring Probes

The field measuring probes constructed are of the fluxmeter type described
above, i.e they work on the principle of Faraday Induction. Beam optics
calculation programs such as "Transport"[73] require the effective length and
harmonic content of the magnet as input data to model the effect of beam
line elements on the accelerated beam, these parameters represent integrated

172

values through the length of the element. It is therefore convenient to use probes which measure these parameters directly and quickly.

The theory of operation of the probes will will be found in the data analysis chapter. A description of the geometry of the probes follows.

15.2.1   Differential Field Probe

The purpose of this probe is to measure the uniformity of field gradient $\partial B_y/\partial x$ on the x axis and $\partial B_x/\partial y$ on the y axis of the quadrupole aperture. The probe consists of a pair of long coils, wound on formers as mechanically symmetrical as possible. The coils are shown schematically in figure 15.1. The coils are longer than the axial length of the magnet to be measured so that they also sample the fringing magnetic field. In this way the field gradient measurements are integrated over the effective length of the magnet. The height and width of the coils are made as small as possible so that an approximation is made to a line integral through the magnet. In practice the formers must accommodate enough windings to give a signal output which is larger than any electronic noise.

The coils are placed together side by side and a jig fits on the end of the formers to hold the coils rigidly together. The windings of the coils are connected together in opposition so that their net output is proportional to the field gradient at the position of the coils (see chapter 16). In practice the coils are stationary and the flux linking them changes as the current in the magnet coils is ramped. The changing output voltage is recorded by the system.

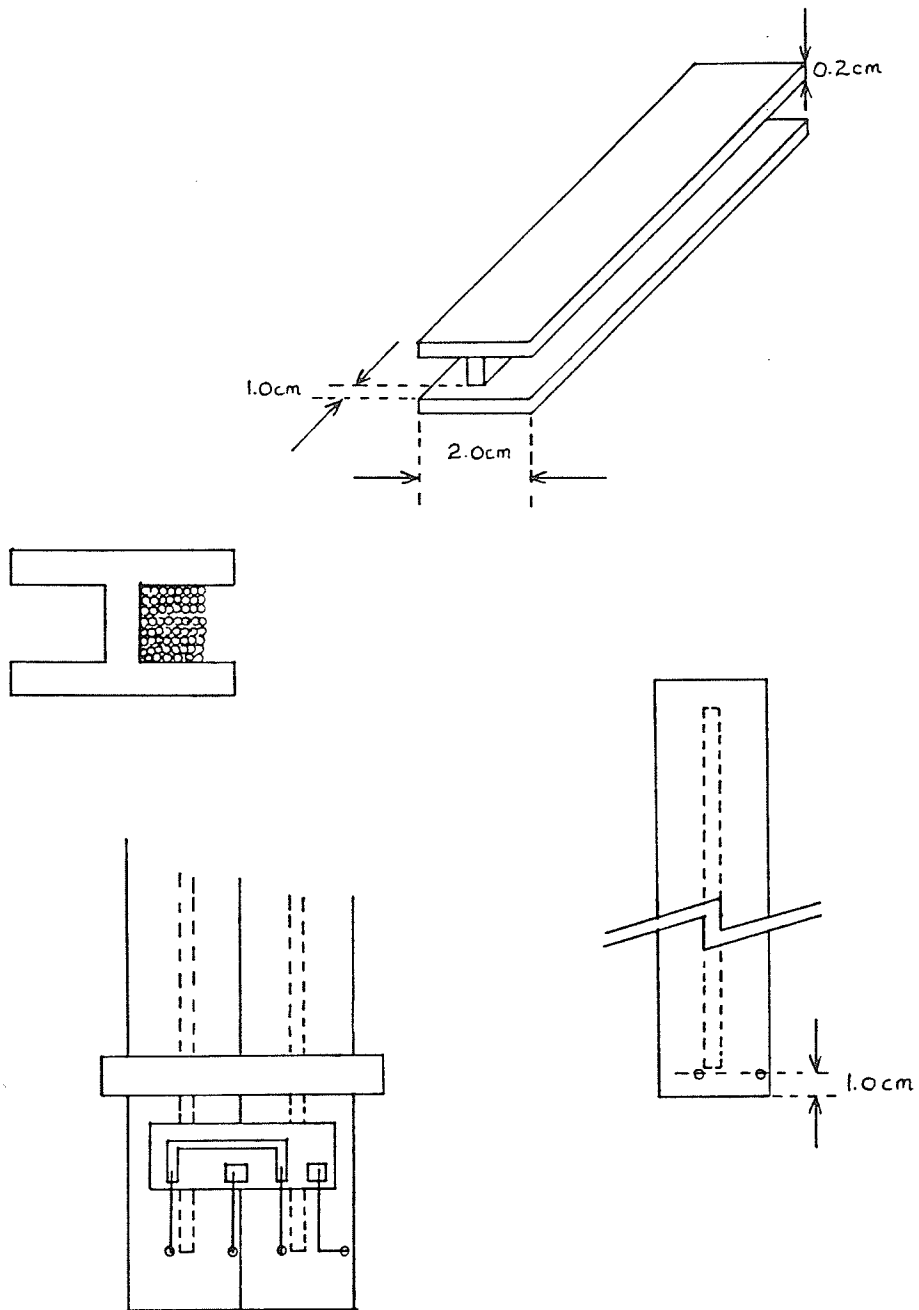Figure 15.2 shows the field gradient probe.

Figure 15.1 Differential field probe schematic.
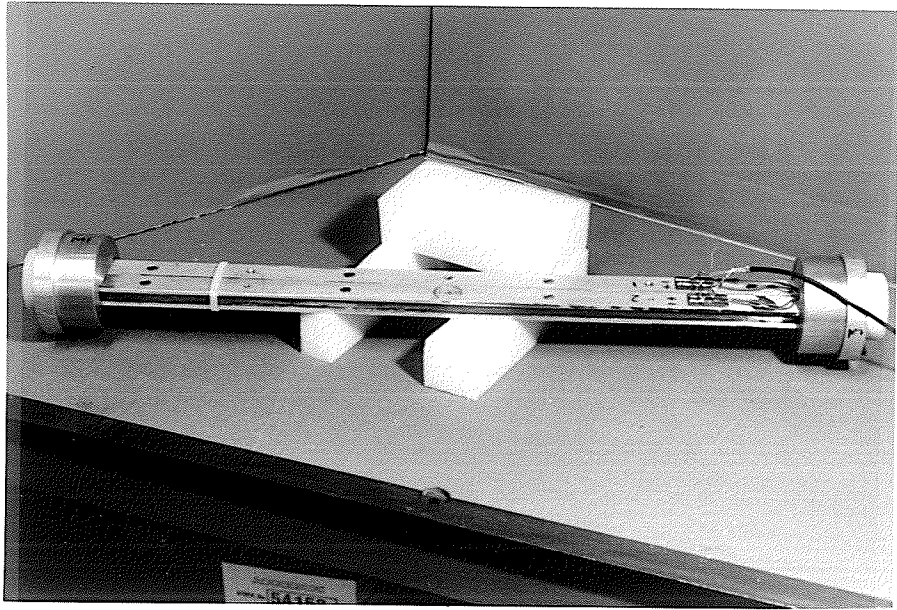
Figure 15.2 Differential field probe.

15.2.2 Harmonic Measurement Probe

The probe consists of an insulating cylinder of plexiglass, which is machined so that its outer surface is accurately symmetrical. The radius of the probe is chosen to be the same as the dimension of the aperture of the magnet. Shallow grooves are milled along the length of the cylinder at angular separations of 45 degrees. Single wires are placed in the grooves in such a way that the winding has the same symmetry as the multipole component being measured, figure 15.3 shows the probe in schematic form.

Three separate windings corresponding to dipole, quadrupole and octupole are wound onto the cylinder. These windings are cemented into place in the grooves and the winding terminations connected to a printed circuit board at the end of the cylinder. The theory of the signal output from the probe is described in chapter 16. The probe rotates in a static magnetic field and the alternating voltages produced are recorded by the system. To measure the output voltages from the rotating probe a 6 conductor ribbon cable is attached to the printed circuit board and wrapped several times around the end of the probe.

In operation the coil rotates quite slowly in the field, approximately once every 6 seconds, the required data is obtained in a few revolutions, and the direction of rotation is reversed simply to rewind the ribbon cable. In this way electrical noise problems associated with rotating contacts are eliminated.

Figure 15.3 Multipole field probe schematic.

15.3 Mechanical Details

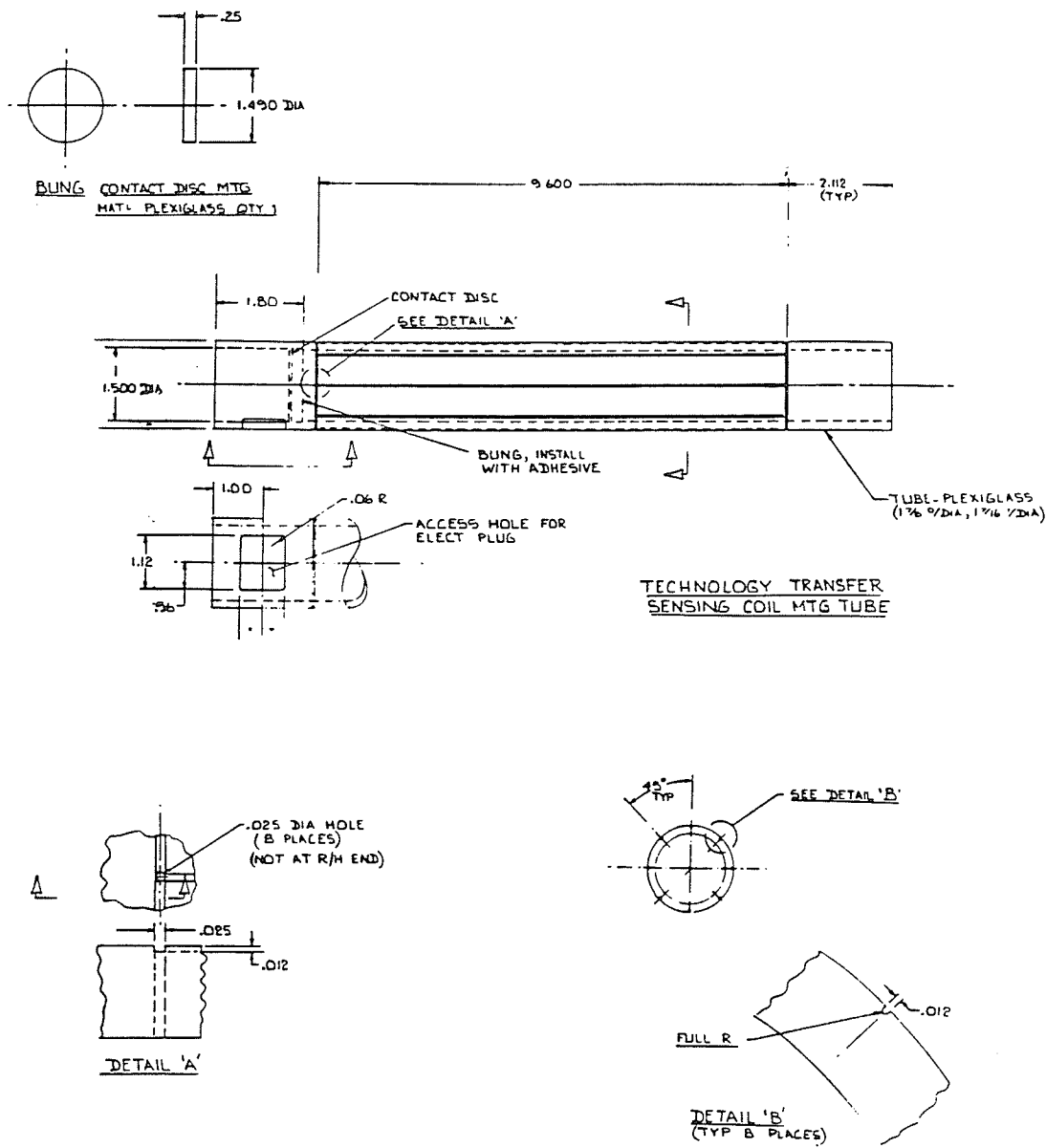The field mapping station is shown in figure 15.4. It consists of two linear translating tables mounted one on each side of the magnet to be measured. The tables move on linear bearings parallel to each other along two ground steel rods set perpendicular to the longitudinal axis of the magnet. In this way the vertical travel of the tables is reduced to the order of 1/1000th of an inch along the entire length of the rods.

The base of each translating table consists of a block of aluminum tapped to accommodate a 3/4 inch diameter threaded rod. The rod is fixed to the base frame of the station at one end via bearings, the other end is connected through an antibacklash gear to a stepping motor which drives the table to the required position. The stepper motor receives 200 pulses for one rotation of its shaft and this results in a table movement of 0.1 inches (2.5mm)

A single pulse from the motor controller therefore results in a linear displacement of 0.0005 inches (0.01mm)

It was decided not to count pulses to the motor to infer the position of each table, but to measure the position absolutely using a commercially available optical graduation type scale. In this type of scale relative movement between a photosensor and an accurately graduated glass rod creates a series of pulses the number of which is proportional to the distance moved.

A scale of this type was attached to each of the translating tables so that the position could be read at any time with an accuracy of 0.0002 inches (0.005mm).

Limit switches were placed at the ends of travel of the translating tables, to turn the driving motors off in the event of a hardware/software error.
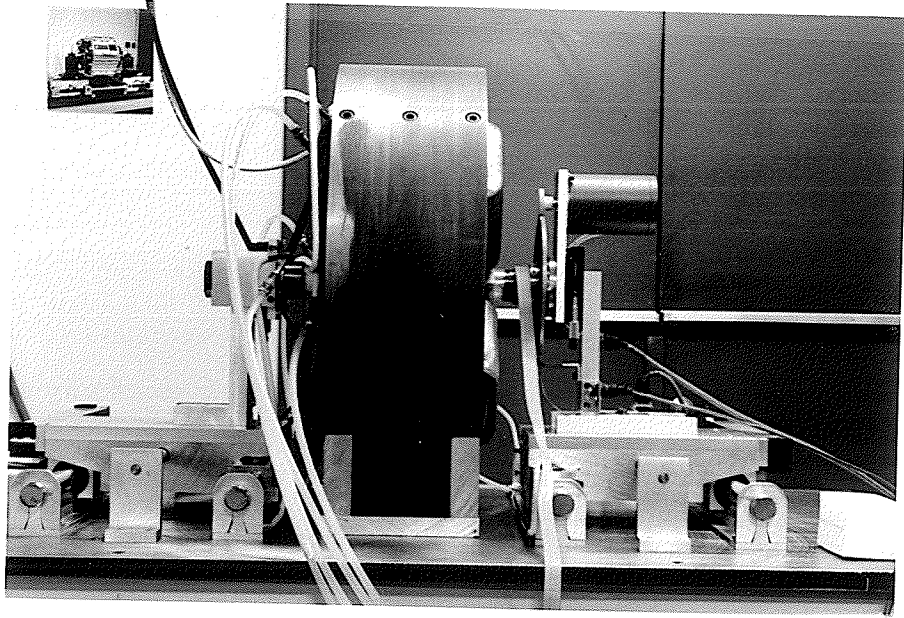
Figure 15.4 Field mapping station.

For positioning the field mapping probes in the Y and Z directions microm-
eter adjustable translation tables of the type found on optical benches were
used.

Arrays of threaded holes were tapped into the X direction translation tables
to provide approximate positioning of the smaller micrometer adjustable ta-
bles.

Field mapping probes were then supported from holders attached to the
smaller translators and the micrometers adjusted to align the probe within
the magnet aperture.

The base frame of the field mapping station consists of a ground stainless
steel one inch plate to which the translating tables and magnet support cradle
are fixed. The cradle is designed specifically for a particular set of magnets
to be measured, so that it matches the contours of the magnet to ensure
the median plane is parallel to the surface of the table and further to ensure
that the longitudinal axis of the magnet is perpendicular to the direction
of travel of the translating table. If a single magnet is to be measured the
ground base of the mapping table may be used as a reference surface for a
dial indicator, etc. and final adjustments of the probes are made with a set
of gauge blocks.

15.4   Instrumentation

15.4.1   Current Supply

Current is supplied to the magnet from a Bruker Corporation BMN-02 cur-
rent supply. The unit can supply up to 100 Amperes at 50 volts via an

impedance-matching transformer. The unit is stable to 1 part in 10^6 over a period of 1 hour. An IEEE-488 interface is provided for computer control of the current supply.

15.4.2 Voltmeter

The voltmeter has a maximum resolution of 6-1/2 digits. In this application the A/D converter samples at a rate of 50 samples per sec which allows 5-1/2 digit resolution and an accuracy of the voltage recorded of 0.02%. The voltmeter is remotely controlled via an IEEE-488 interface. In practice, it will make a number of readings after receiving a trigger from the measurement probe. It will then transfer these readings to the controlling computer over the bus.

In the case of field gradient measurement static probes are positioned in time-varying magnetic fields and in the case of multipole measurements rotating probes are positioned in static magnetic fields. In either case a time varying voltage is produced by the probe which is sampled by the above mentioned Hewlett Packard 3457A digital voltmeter.

15.4.3 Position Readout

The position of the motorized X direction translating tables is read out via a Mitutoyo GR15 optical graduation type position encoder. The encoder allows the position, relative to some origin, of the tables to be read with an accuracy of 0.005 mm. The position of each table information is sent on demand to the controlling computer via an RS-232C serial interface.

15.4.4 Motor Controller

Stepper motor control is accomplished using an in-house designed motor controller. The unit can supply the series of pulses required to drive up to three Stepper motors, two of these are used to drive the X direction translating tables, the third is used during a rotating coil survey to drive the harmonic probe.

The unit is computer controlled via an 8 bit parallel digital interface.

15.4.5 Controlling Computer

A single computer is used for instrumentation control, data acquisition and analysis. It consists of an IBM-PC/XT containing IEEE-488, + RS232C interface cards and a Data Translation DT-2801 card which provides 8 bit digital output. A 25MB hard disk is used for storage. Graphics display resolution is 640 (horizontal) by 350 (vertical).

15.5 Interfacing

The standalone instruments i.e the linear translation table position readout, the digital voltmeter and the the magnet current supply, transfer information to the computer over digital to digital interfaces. The computer and the devices assert "handshaking" signals to control the flow of information between them. The interfaces are of two types, a serial interface in which information is transferred one bit at a time, and a parallel interface which transfers information over 16 parallel lines simultaneously, i.e one byte at a time. The devices have the advantage that data taken by the standalone instrument

may be kept in a small memory buffer within the instrument until requested by the computer, as the number of devices and interfaces connected to the computer increases, this feature is particularly useful. Information is transmitted over these interfaces in the via a set of American Standard Code for Information Interchange (ASCII) characters. The stepping motor controller is computer controlled but contains no information buffer, it is controlled over an 8 bit parallel digital interface.

15.5.1 RS232 Serial Interface

RS232 is a serial communications standard that was originally developed as an interface between data terminal equipment and data communications equipment. It has since become one of the most widely used standards for data communication between two devices that can transmit and receive binary and serial data. To allow the IBM PC computer to communicate with another device using this standard a circuit board must be installed inside the computer to process the signals from the interface and pass them to the internal data bus of the computer. The circuit board contains a set of outputs which are connected to the external device via a 25 pin plug. Most RS232 interfacing can be accomplished through the use of 6 of these outputs alone. These are:

Pin	Circuit Name	Signal Direction
2	Transmitted Data	Out from PC
3	Received Data	In to PC
5	Clear to send	In to PC
6	Data Set Ready (DSR)	In to PC
7	Signal Ground	
20	Data Terminal Ready (DTR)	Out from PC

The exchange of data between the computer and the external device takes place along lines 2 and 3, the other lines assert signals to control the handshaking between the two devices.

In the case of the PC receiving data from the external device, the software controlling the board will assert pin 20 of the connector on the PC, this line will be connected directly to pin 5 (clear to send) and 6 (Data set ready) of the external device, instructing it to transmit data over line number 3.

For transmission of data from the PC to the external device, the software controlling the board waits until the external device asserts its DTR line which is connected to pin 6 (Data set ready) on the PC. When this occurs serial data is sent to the external device along line 2.

A disadvantage of the serial interface is that a separate interface card is required for each instrument that is to connected to the computer.

The linear translating table readout sends data to the computer using the RS232 interface, many devices use only a subset of the control lines available on the interface and the readout is such a device. In practice the device uses only pin 2, transmitted data. When a separate circuit on the output of the position encoder is closed, a position reading is taken of each of the encoders

(one per translating table) and the information is sent on the interface to the RS232 port on the PC. In practice it was possible to arrange for the PC to assert Data Terminal Ready and to process this signal with a separate circuit so that the reading request circuit of the position readout was closed.

15.5.2   IEEE-488 Interface

The IEEE-488 Interface is a general purpose interface standard for sending byte serial commands and data between instruments. The handshaking protocol was initially developed and patented by Hewlett Packard, it was adopted in 1975 by the Institute for Electrical and Electronic Engineers (IEEE) as an interface standard.[74] Its main advantage is that is has a bus structure i.e several devices can be placed along the same set of parallel lines and may communicate with each other using the IEEE-488 protocol. Devices on the bus may perform three kinds of function, they may be "talkers", that is they may transmit data to other devices on the bus, there can only be one active talker at a time. Alternately a device may be a "listener" i.e it may receive data or instructions from another device. There may be more than one active listener on the bus at a time. The third function a device may perform is to act as a controller, i.e a coordinator of which device may talk and which devices may listen. The interface supports two modes of operation "command" mode and "data" mode. The controller, which in the case of the mapping system is always the computer, may in command mode instruct the digital voltmeter to perform a series of voltage readings on the 3 volt D.C scale, in this mode the controller is the talker device and the voltmeter is the listener device. Just as the controller (or an external source) triggers the voltmeter, the controller switches to listener function and the voltmeter becomes the talker, the mode of operation becomes data

185

mode and the voltage readings are transmitted over the interface in ASCII format to the computer serial port. Alternately the readings may be stored in a memory buffer within the voltmeter until requested by the controller, in this way as the voltmeter is performing the readings, the controller may be performing some other function, for example instructing another device to vary parameters which will in turn affect the voltage being recorded (such as varying the current in the coils of an electromagnet).

The interface, originally known as the GPIB or general purpose interface bus, consists of 24 lines, 8 of which are ground lines, giving the interface high immunity against electrical noise. The other 16 lines are divided into 3 groups, there are 8 data lines, 3 data-byte control lines and 5 interface management lines. The 3 data-byte control lines are the information hand-shaking lines, they are known as Not Ready For Data (NRFD) Data Valid (DAV) and Not Data Accepted (NDAC) lines. When information is to be transferred over the bus, all the designated listeners must be ready to receive the data. If one of them is not it asserts the NRFD line by setting the line low (low represents logic 1 or "true" in this standard). When all listeners are ready to accept data the talker asserts the DAV line low which in turn sets the NRFD line low while the listeners pick up the first data byte, when all listeners have received the data byte they assert the NDAC line which resets the DAV line which in turn reset the NRFD line. This sequence is repeated for each Byte of transmission.

The bus management lines are known as EOI (end or identify) ATN (attention) SDC (selected device clear) GET (group enable trigger) and GTL (go to local). EOI is used to inform devices when a talker has finished sending a series of bytes, if the controller is asserting EOI, it may also be used to "poll" the devices on the bus to check for problems in response to a service

186

request (SRQ) from a device. ATN when asserted by the controller is used to designate devices on the bus as talkers, listeners or standby devices. Go to local releases a device from remote control and selected device clear resets the device to its default setting. Group enable trigger initiates simultaneous data acquisition from those selected devices.

Devices on the bus are assigned a 5 bit address, when the controller is talking to a particular device in command mode it first asserts ATN and then release the address of the device(s) on the data bus.

15.5.3   8 Bit Parallel Interface

The stepping motor controller is an in house design for providing power for up to three stepping motors. It is remotely controlled by an eight bit parallel interface using TTL logic levels. The eight lines of input are divided so that each motor may be given single pulses to produce single steps, or a line may be set that drives the motor continuously. Another line on the interface determines the direction of rotation of the shaft of the motor. The use of eight bits allows three motors to be driven simultaneously in any of the modes described. The motor controller sends no signals to the computer. In the event of a hardware/software error, limit switches mounted on the mapping table are activated.

To interface the motor controller to the IBM PC bus, a Data Translation DT2801 board was installed in the PC. The board contains an eight bit parallel output which can be programmed to control the stepping motor power supply.

The programming of the system of devices and interfaces was reduced considerably by the use of a commercial software package with language type

facilities which could call interface control subroutines written in assembler language for the IBM PC. This is described in the next section.

15.6   Software

The data acquisition and instrument commands functions are controlled by software based on a commercial software package called ASYST. ASYST's syntax is similar to that of FORTH and APL. Its main advantages are (1) that it includes commands such that programs can be easily written to control the interface cards mounted in the computer; (2) it has built in analysis functions which can perform, for example, Fourier transforms on the acquired data; and (3) it has a set of graphics routines which can be used to quickly display the results of operations on acquired data. Asyst is based on the concepts of a stack and routines known as "words". After entering the software system, a word may be defined at the lowest level as a series of machine code instructions.

The system may then be "saved" on disk as a new system to which the added word is "known". Higher order words may be defined as a series of lower level words, which in turn call lower level words until machine language is reached at the lowest level. Words are thus interpreted as they are entered and the more complex system is saved. In practice a word entered at the terminal, for example READ.X.POSITION will perform a series of functions previously known to this system. In this example the system first raises DTR on the serial port to request the multiplexer of the linear table position readout to take a position measurement, the ASCII data are transferred over the serial link and stored in a string array also previously defined within the software system. A word previously defined which translates ASCII data to

188

numerical data is executed and the results are displayed on the computer terminal or stored in another previously defined array for readout at the end of a series of measurements.

In this way complex sequences of instrument control and data acquisition and manipulation can take place through relatively simple programs.

It was realized that use of the Asyst software package would considerably reduce the time required for programming the mapping system, an early version of the package was used and some errors were found which were fixed by the supplier. Since that time Asyst has become an industry standard package where instrument command and data acquisition is controlled by an IBM personal computer.

15.7   Field Mapping Process

15.7.1   Introduction

This section describes in detail the sequence of events which result in a map of the field gradient and harmonic content of the magnet.

15.7.2   Field Gradient Mapping Process

alignment

The field gradient measurement probe is aligned in the magnet aperture so that its center line coincides with the mechanical axis of the magnet, and such that it is equidistant from the pole tips of the magnet. The vertical alignment is set using micrometer adjustments attached to the jig which

holds the probe. The horizontal translating tables are driven separately until the axis of the probe is in the required location. At this point the probe movement is confined to the Ox plane. The translating tables are next moved in unison to the extreme -x position that the field gradient is to be measured at. In the case of a magnet with a 100mm aperture for example, the probe is driven to an initial position of -50.0mm, the system is then configured to take 100 readings at 1mm intervals. Limit switches, which can slide along the ground metal rods along which the translating tables move, are pressed against the outer edge of the table and fixed into place. The tables are moved to the extreme positive x position and another set of limit switches fixed in position. In this way hardware or software errors which might cause the probes to "overshoot" are eliminated.

The translating tables are returned in unison to the starting negative x position. While travelling the clearance between the surfaces of the probe and the pole tips are checked with gauge blocks to ensure they are the same at both extremes in x, to ensure that the probe is moving on the median plane of the magnet. At this point the field measurement can begin as a result of a single command word typed into the computer.

15.7.3   Single Measurement

The command word MOV+1MM sends a series of 80 pulses spaced by 50 ms along two lines of the 8 bit parallel output port of the computer, which is connected to the stepping motor controller. These pulses are processed so that they represent logic levels 1 and 0. The other 6 lines of the parallel output are arranged high or low so that the desired result occurs, the driving of the two translating tables simultaneously through + 1mm.

The stepping motors drive threaded rods which pass through tapped aluminum blocks to drive the translating tables. The pitch of these two rods is not exactly equal and therefore a series of 80 pulses will not produce exactly 1mm displacement for each rod. Before sending the pulses to the motors, the program adds an increment of 1mm to a scalar variable stored in computer memory. Initially this scalar is set to zero. The program then executes the word READPOS. As mentioned above, this has the effect of raising the DTR line on the RS232 port to request the position encoder multiplexer to take a measurement of X1 and X2 positions and send the data over the serial link. The ASCII data sent is converted to a numerical value and each position is compared to the value of the scalar stored in memory.

The word COMPENSATE evaluates the difference between the position reading and that required, pulses are sent to each of the stepping motors, the positions are read again and the process is continued until the position of the translating tables agree with the required position to within 0.005mm (0.0002 inches). The probe position is then stored as the first element in a 100 element array.

The words above are called by the word MAKEMEAS whose function is to perform a single reading. After READPOS and COMPENSATE have been executed, further commands and acquisition take place on the GPIB bus. The computer is set to talker and the digital voltmeter and current supply are set to listener function. A string-array buffer in computer memory is reset and the multimeter is instructed to perform 256 readings and to begin taking readings after receiving a trigger from an external source.

The 256 multimeter readings are made with 5-1/2 digit resolution after receiving the external trigger. The current supply is instructed to supply 50 amperes to the magnet coils on receipt of the command SETI250A. The

command SETI250A first sets the computer to listener and the multimeter to talker. As the current in the coils begins to ramp from 0 to 50 amperes, a rapidly increasing voltage is developed across the magnet coils, this voltage is applied through a resistor to the emitting diode of an optocoupler device, the phototransistor on the output side of the device turns on and provides the external trigger to the digital voltmeter, this process takes place before the signal from the field probe has risen above the level of the pickup noise.

The digital multimeter begins a series of 256 readings which it makes over an interval of 6.0 seconds. After this time the current supplied to the coils, and the resultant magnetic field are both constant and the output from the differential field probe has reduced to zero. The readings from the digital voltmeter are in ASCII form and are sent to the string array in computer memory as they are taken. The standard technique for performing such measurements involves storing the readings in the voltmeters' internal buffer and reading them out after the measurement. However, the number of readings and the accuracy to which they were made required a larger buffer than available within the instrument. Fortunately, it was possible to transfer the readings directly as they were taken with sufficient speed that the transient output from the probe could be recorded.

The ASCII data in computer memory are converted to numerical form. It will be shown in Chapter 16 that the differential field is proportional to the difference of the individual voltages V_i read from the probe. This number is evaluated and stored in an array in computer memory where the index of the array is the same as that for the position measurement.

Field Gradient Output

The above section describes the process for incrementing the probe position and taking a measurement of the differential field at the probe location. This process is repeated 100 times which results in two arrays, one contains the positions of the probe and the second, a voltage proportional to the values of differential field at those positions. After performing the measurements the program plots the differential field vs. position data on the computer console.

The individual coils within the probe were machined and wound to be as symmetrical as possible, in practice accurate symmetry is difficult to achieve. To cancel the effect of the asymmetries of the two coils, the process described above is repeated with the coils rotated through 180 degrees. The average of the values corresponding to differential field (at each position X_i) for each orientation of the probe is calculated and displayed versus position to show the uniformity of differential field in the aperture of the magnet (see chapter 16). A flow chart of the differential measuring process is shown in figure 15.5.

In practice the magnet is then rotated through 90 degrees and the measurement process repeated on the Oy axis.

15.8   Harmonic Content Measuring Process

The harmonic measuring probe is aligned so that its axis coincides with the mechanical axis of the magnet. This is accomplished by an approximate positioning of the probe with a dial indicator followed by a series of small adjustments of the vernier for vertical alignment, and adjustments of the
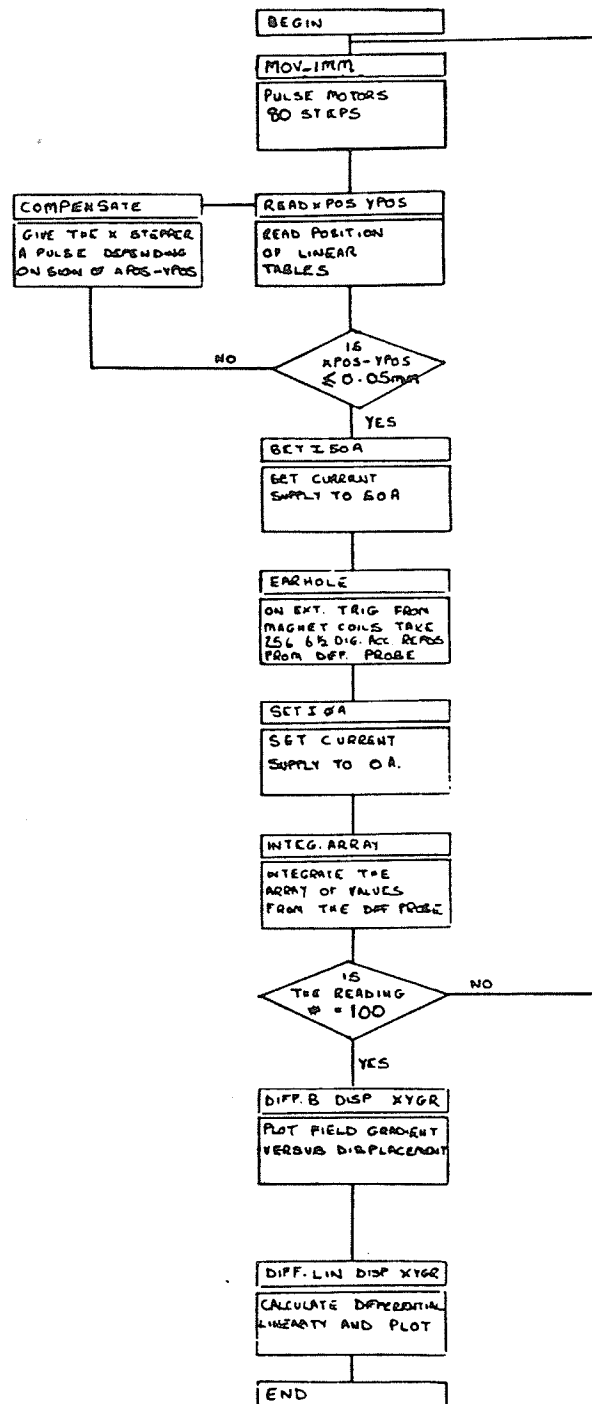
Figure 15.5 Differential field measuring flow chart.

194

translating tables for horizontal alignment. The final adjustment is checked by a series of gauge blocks. When the distance between the outer surface of the cylinder and each of the pole tips is the same, on each end of the magnet, the probe is aligned. The translating tables are fixed in place at this location by sliding the limit switches against the sides of the blocks holding the translating tables. In this way the translating tables will remain fixed in the event of a hardware error.

The rotating motion of the probe is controlled by the computer and a "programmable limit switch", i.e. a limit switch which can halt the rotation of the probe, if desired, by the application of a voltage output from the DT2801 Interface board to a logic chip.

The Asyst word MPOLE calls a series of lower words to perform the multipole measurement. As the probe rotates in a static magnetic field, an alternating signal is produced from each of the windings.

Consider the situation shown in figure 15.6, where the harmonic probe is shown in cross section and positioned in the aperture of the magnet. The windings of the probe are at their closest position to the pole tips in this location and for convenience, let this represent the starting angle ($\theta = 0°$) of the measurements. The number of readings taken by the voltmeter is arranged so that just as the voltmeter has taken 305 readings, the probe has rotated through 360 degrees. After a single rotation of the probe the direction of rotation is reversed to rewind the ribbon cable. The measurement process is repeated 5 times over a period of a few minutes. If one assumes that the magnetic field has remained stable over this period (the current supply is stable to 1 part in 10^6 over periods of 1 hour) then, if the voltmeter trigger pulse occurred at a well defined angular position, the 5 output waveforms will be identical apart from random electronic noise. Further, if the

195

average of these 5 signals is taken at each angular position, then the signal to noise ratio will be reduced. Finally, if one takes the Fourier transform of the measured waveform, the harmonic content of the magnetic field may be determined. This measurement is performed by the system as described below. The harmonic probe is driven by a stepping motor through a set of gears which reduce the speed of revolution of the probe to one revolution every 4.175 seconds. A tab protrudes from the large gear and passes through the gap of an optocoupler consisting of an infrared diode and infrared photodarlington transistor separated by a small distance (see figure 15.6). The Asyst word REWINDO reverses the direction of the motor, rewinding the ribbon cable in the process. The probe is rewound to an angular position of -10 degrees. Looking at the end of the probe -10 degrees represents 10 degrees anticlockwise from the desired starting point. At this position the tab protruding from the large gear is located between the infrared diode and the photodarlington. The output from the photodarlington is connected to a logic OR gate as shown in figure 15.7, the second input to the OR gate is a logic level supplied by the DT2801 board. The output from the OR gate is connected to the limit switch circuitry of the driving motor in such a way that a logic 0 output stops the motor and a logic 1 does not. When the probe has stopped at angular position -10 degrees a logic 0 is presented at both inputs to the OR gate, which results in a logic 0 output, which in turn stops the motor. The Asyst word ROT1 rotates the probe through an angle of 370 degrees. It can be seen that the limit switch must be disabled for a complete revolution of the probe, therefore after setting the probe in motion the program instructs the DT2801 board to provide a logic 1 to the OR gate, disabling the limit switch. For the signal averaging technique to work the voltmeter must be triggered at precisely the same angular position

196
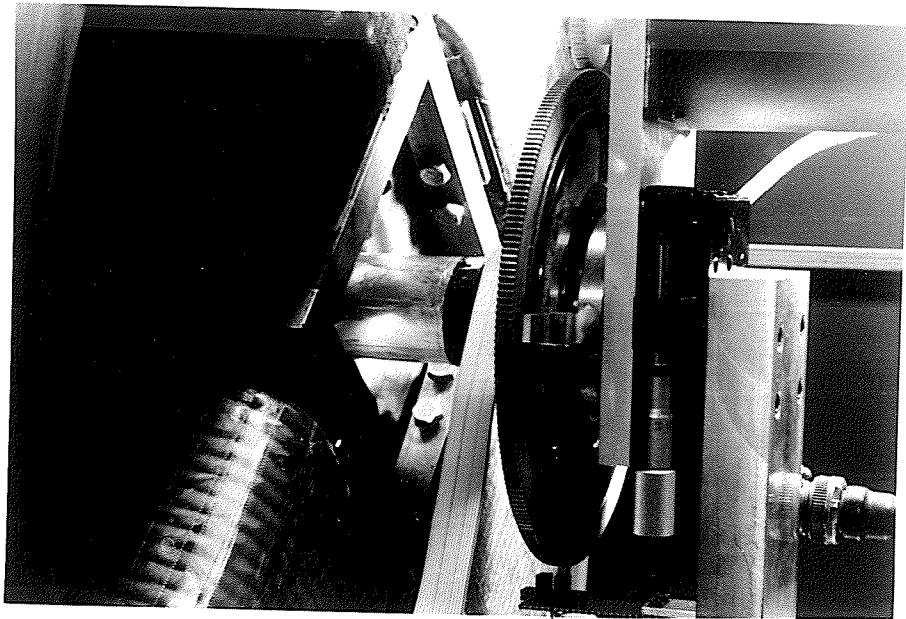
optocoupler
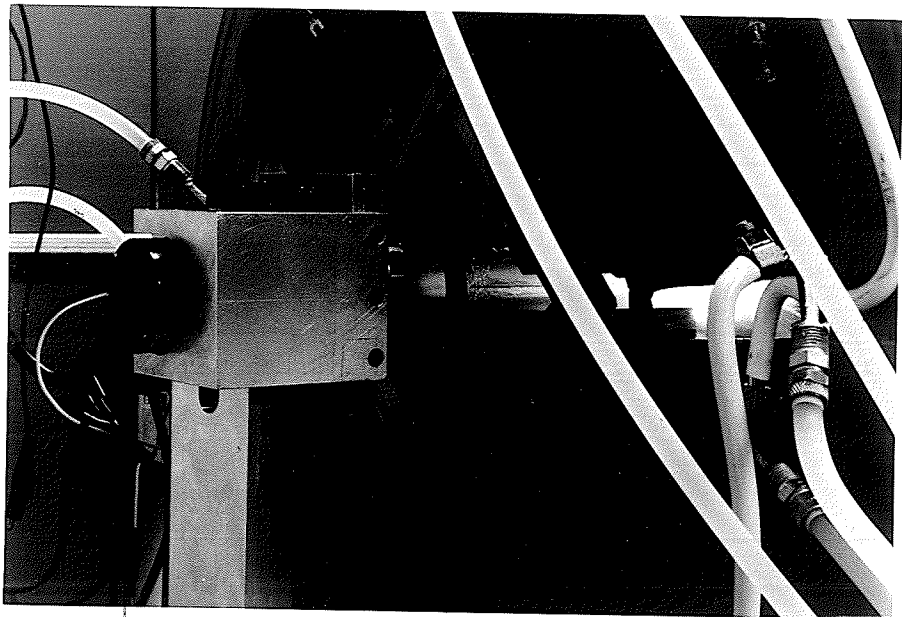
Litton angular encoder

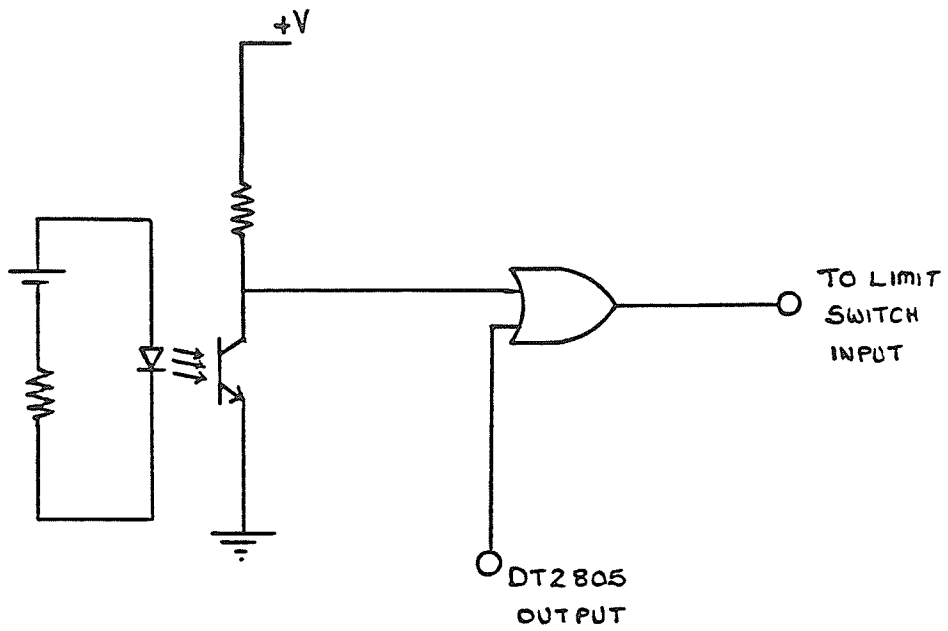Figure 15.6 Multipole field probe inside magnet aperture.

Figure 15.7 Limit switch wiring.

for each measurement. To accomplish this a Litton angular encoder was mounted on the opposite end of the harmonic probe shaft. The encoder is based on a similar technique to the optocoupler described below, and provides a pulse output as the probe passes through 0 degrees. This pulse is fixed with respect to the angular position of the shaft and has a width corresponding to 0.001 degrees. The pulse is fed to the external trigger of the voltmeter.

As the Asyst word ROT1 executes, the pulse triggers the voltmeter which samples the output signal from the probe over a single rotation. As each reading is taken the ASCII data is sent directly to a string array in the memory of the computer over the GPIB bus. The data is converted into numerical form and stored in another array. Data from successive revolutions of the probe are added to the numerical array and the average value calculated. After the data have been acquired the Asyst word FOURIER performs a fast Fourier transform (FFT) on average values stored in the array. For the quadrupole winding for example, the stored signal represents two oscillations of a cosine waveform with some perturbation due to higher order multipoles.

The Fourier transform of such a waveform will yield a frequency spectrum whose peak amplitudes, if used to reconstruct the signal would give a waveform whose amplitude was zero for $\theta < 0$ radians, $A_o \cos 2\theta$ for $0 < \theta < 2\pi$ radians and zero for $\theta > 2\pi$ radians. A series of "phantom" components would be introduced in to the Fourier spectrum to account for the discontinuity in amplitude at $\theta = 0$ and $\theta = 2\pi$ radians. The result of this would be a broadening of the peaks which represent the components of the true signal.

The Asyst word FOURIER calls the word CATENATE which catenates the contents of the array in memory to itself and places the result in another

array. The Fourier transform of this array is determined and the magnitude of the Fourier components are plotted versus frequency. The heights of the first 20 peaks are read by the program. From these data the harmonic component of the magnetic field may be determined as shown in the following chapter. A flow chart of the multipole measuring process is shown in figure 15.8.

The following chapter describes the analysis of the data from the field measuring probes.
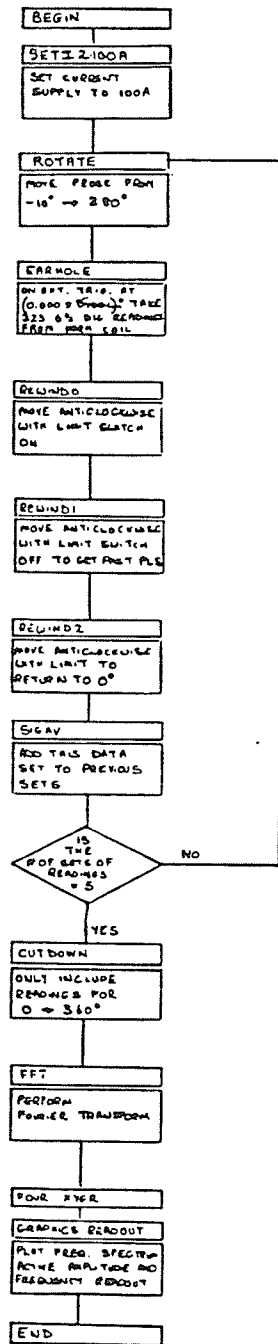
Figure 15.8 Multipole measurement process flow chart.

Chapter 16

Analysis of Field Measuring Probe Data

16.1 Introduction

This chapter describes the analysis of the outputs from the field measurement probes to yield useful magnetic field parameters, for the focussing elements under test.

16.2 Differential Coil

As the current in the magnet coils is ramped the emf generated in each coil is given by:

$$e(t) = -\frac{\partial \phi}{\partial t}, \qquad (16.1)$$

where ϕ is the magnetic flux linking the coil. It follows that:

$$\phi = - \int e(\text{t})\text{dt} \qquad (16.2)$$

If the sampling rate of the voltmeter is high enough this expression may be replaced by the expression for the discrete samples:

$$\phi = \sum_{i=1}^{n} e_i(\text{t})\Delta\text{t} \qquad (16.3)$$

If the two coils are connected so that their signals oppose each other the difference in the flux linking the two coils may be found:

$$\phi_1 - \phi_2 = \sum_{i=1}^{n} (e_1 - e_2)_i(t)\Delta\text{t} \qquad (16.4)$$

Due to asymmetries in the probe construction the measurement of the differential flux is performed twice in each plane (Ozx and Ozy). After the first measurement, the probe is rotated through 180 degrees and the measurement repeated. The individual output from each of the two measurements is shown in figure 16.1. The probes are aligned so that they move along the mechanical median plane of the magnet. The magnetic median plane will coincide with the mechanical if the construction of the magnet is perfect. In practice neither the construction of the magnet or the measuring probe is perfect, and so the effective center of the measuring probe may move out of the magnetic median plane of the magnet as the mapping takes place. The result, as shown in the figure is that the plot slopes. When the probe is rotated through 180 degrees, the orientation of the effective center of the probe with respect to the magnetic median plane is opposite to the case for zero degrees and the plot slopes in the opposite direction. If the readings can be taken in accurately reproduced positions for zero degrees and 180 degrees
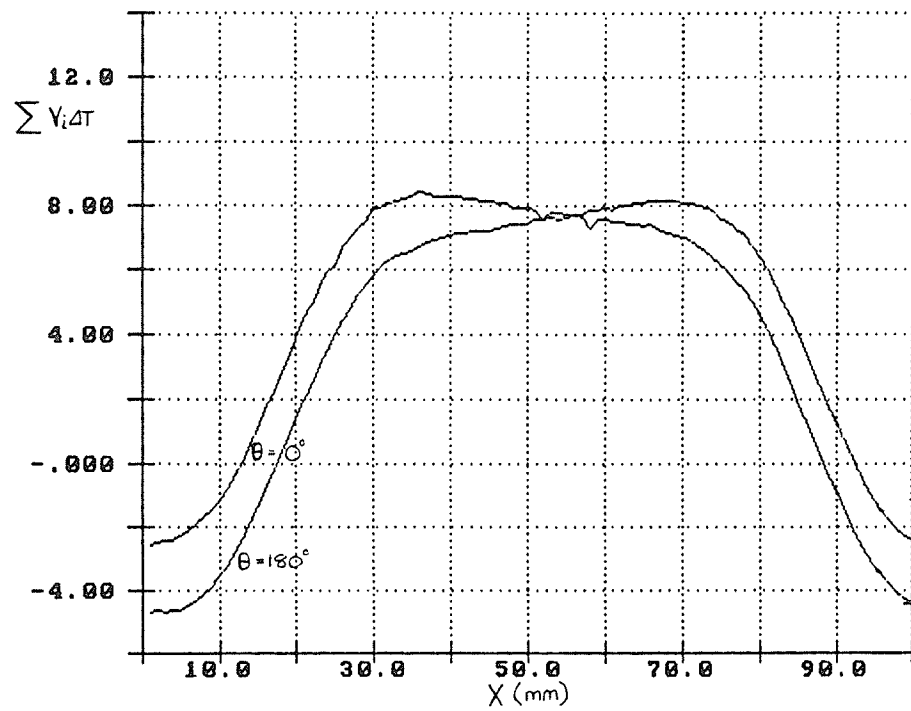
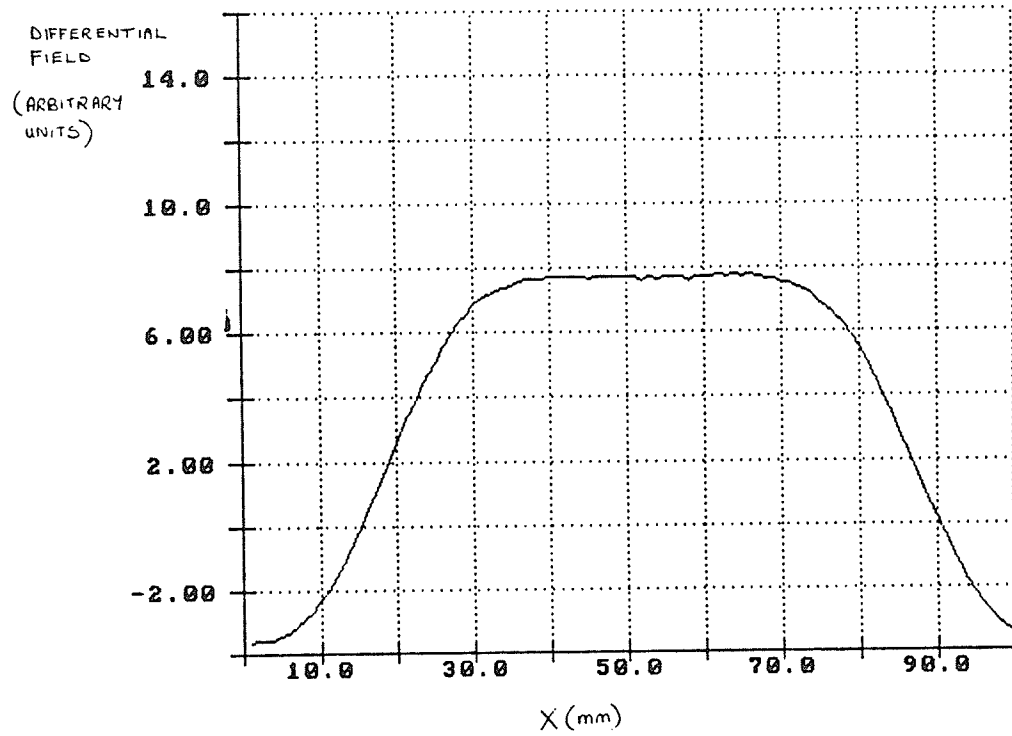Figure 16.1 Individual output for each pass of the differential field probe.

Figure 16.2 Uniformity of differential field in the aperture of a quadrupole
magnet used in a microprobe arrangement.

orientations, and the signals averaged, the effect of the misalignment can be removed as shown in figure 16.2.

The value calculated is the differential flux linking the two coils. This value can be converted to the field gradient if the distance between the effective centers of the coils, and the effective area of each coil is known. In practice the separation of centers is determined by observing the individual output from each coil as it passes the axis of a "calibration" quadrupole i.e one whose axial position is well known [60]. The current in the quadrupole coils is ramped and the measuring coil oriented so that zero output is observed. This position is recorded and the process repeated for the second coil. The distance between the two positions for zero output corresponds to the effective separation of the centers of the two coils.

To determine the effective area each coil is placed concentrically within a large coil whose dimensions are accurately known [60]. The two coils are placed in a calibration dipole magnet whose field distribution has been accurately determined using the Nuclear Magnetic Resonance technique. As the current in the dipole windings is ramped the ratio of the outputs of the two coils is equal to the ratio of their area if the number of turns in each coil is equal.

16.2.1 Useful Aperture

In chapter 13 it was shown that a perfect quadrupole will have a field that varies linearly with radius, i.e $\partial B_r / \partial r = $ constant. The useful aperture of a magnet may therefore be considered as that area over which the field gradient is essentially constant, or that area over which the effective length of the magnet is constant. Let the useful aperture be an area whose radius

represents the point at which the field gradient has fallen to 90 % of its central value. Since the field gradient is directly proportional to the differential flux this information may be obtained from a plot such as that in figure 16.2. In the case of a quadrupole used as one of the focussing elements of a proton microprobe arrangement (figure 13.2.) this distance is $\pm$ 20 mm from the center of the aperture.

16.2.2 Effective Length

The part of a quadrupole aperture over which the effective length of the magnet is constant is an important parameter in beam optics.

The effective length may be determined by analyzing the signal from a single coil of the differential probe. The effective length of a magnet is given by:

$$L = \frac{1}{B_n(0)} \int B_n(z)dz \tag{16.5}$$

Where B_n is the component of the field perpendicular to the plane of the measurement. The integral value above may be determined from the sampled data output if the coil dimensions are accurately known. The value of $B_n(0)$ is the component of B perpendicular to the plane of measurement in the center of the magnet and may be determined using a small search coil of accurately known dimensions, cemented to the center of the long coil. Alternately a Hall probe may be used. It is the variation of effective length versus displacement from the axis which is of use, since the flux linking the coil is directly proportional to $\int B_n dz$. This data also gives the effective length of the magnet. No data was acquired for the effective length of the quadrupole magnet described above.

16.3 Harmonic Probe Theory

16.3.1 Introduction

The representation of the magnetic field was expressed in chapter 13 as a function of the complex variable z: (11.8)

$$B(z) = B_x + iB_y$$

where:

$$z = x + iy = re^{i\theta}$$

The field may similarly be described in cylindrical polar coordinates :

$$B = B_r + iB_\theta \tag{16.6}$$

It is possible to expand the field as a power series of the form [75] :

$$B = \sum_{n=1}^{\infty} iC_n r^{n-1} e^{-i(n\theta + \psi_n)} \tag{16.7}$$

It can be seen that the magnitude of B is constant on the circle of radius r and that the sign of B changes n times as θ increases from 0 to 2π radians. The term $C_n r^{n-1}$ is therefore the 2n component of the field and as such has units Tesla.

A normalized set of harmonic coefficients is defined by :

$$c_n = \frac{C_n r^{n-1}}{C_N r^{N-1}} = \frac{C_n r^{n-N}}{C_N} \tag{16.8}$$

where N identifies the dominant harmonic. In the case of a quadrupole, N=2. If all the harmonics are evaluated at the same radius then $c_n = C_n/C_N$.

16.3.2 Application to a rotating coil wire loop

Consider a single wire mounted parallel to the axis of the multipole magnet, and on the surface of a cylinder of radius r and length l, concentric with the magnet. A loop of wire is constructed by two radial elements labelled r_1 in figure 16.3 and another wire along the magnet axis. The cylinder is placed in the aperture of a magnet as shown in figure 16.3. As the cylinder rotates, the emf produced is given by the Faraday induction law:

$$e(t) = -\frac{d\phi}{dt} = -\sum_{n=1}^{\infty} \frac{d}{dt} \int \vec{B} \cdot \vec{n} \, da \qquad (16.9)$$

where ϕ is the flux passing through an area da of the rotating loop, and da = Ldr. Substituting the expression for B from (16.6) above:

$$\phi = \int \vec{B} \cdot \vec{n} \, da = Im \left(\int \left[\sum_{n=1}^{\infty} iC_n r^{n-1} \exp^{-i(n\theta + \psi_n)} \right] Ldr \right) \qquad (16.10)$$

$$= Im \left(\sum_{n=1}^{\infty} iC_n \frac{Lr^n}{n} \exp^{-i(n\theta + \psi_n)} \right) \qquad (16.11)$$

The emf generated is therefore given by:

$$e = -\frac{d\phi}{dt} = -C_n Lr^n \cos(n\theta + \psi_n) \frac{d\theta}{dt} \qquad (16.12)$$

where ψ_n is a phase angle for the harmonic n.

The amplitude of the voltage signal from such a rotating loop will be mostly due to that of the fundamental component (N). The major contribution to the amplitude of the signal from a single wire loop will be:

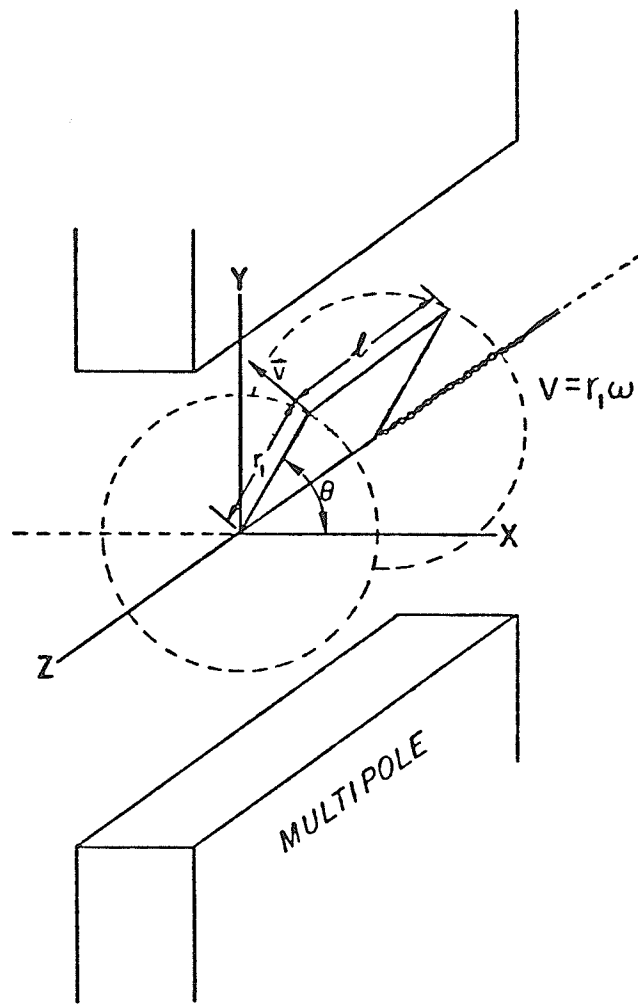$$V_l = C_N r^{N-1} Lr\omega \qquad (16.13)$$

Figure 16.3 A single wire loop in the aperture of a magnet.

where ω is the frequency of rotation of the cylinder. The above equation has been written so that the term $C_N r^{N-1}$ appears and is the value in Tesla of the fundamental component of the field.

16.3.3 Output Signal from a single wire loop

Consider the measurement of harmonic coefficients of a quadrupole magnet using the single loop design above. Let the radius of the cylinder be made as close as possible to the radius of the aperture of the magnet. Let the quadrupole and measuring coil have the following parameters:

- pole tip field: 0.8 T

- aperture radius: 3.0 cm

- cylinder length: 25.0 cm

- rotation rate: 1 revolution every 4.0 s

The amplitude of the voltage signal corresponding to the fundamental component will be:

$$V_l = 0.8 \times 0.25 \times 3.0 \times 10^{-2} \times \frac{2\pi}{4} = 9.424\text{mV}$$

In a well designed magnet, it is desirable that the higher order harmonics have coefficients 10^4 times less than the fundamental. To verify this by measurement would require measurement of the signal from the coil with an accuracy of 9.424mV/10,000 = 1 μV. The current generation of analogue to digital to converters cannot sample an alternating signal at the required sampling rate with this accuracy, therefore some way must be found to increase the sensitivity to the higher order harmonics.

Various methods exist for increasing the response of single loop rotating coils. These include: (i)Increasing the number of turns in the loop. (ii)Rotating the coil at a higher rotation rate and reading the coil output via a set of slip rings through a narrow band pass filter [76]. (iii) A second coil is placed concentrically with the first at a smaller radius, the second coil is less sensitive to the higher order harmonics and its output is amplified, inverted and added to the to the signal from the main coil so that the fundamental signal is "bucked out" [77].

16.3.4 Morgan Coil Design

A more elegant method for measuring higher order components of a magnetic field consists of winding a coil on the surface of a cylinder in such a way that the coil has the same symmetry as the magnetic multipole component to be measured. This coil design is known as the Morgan coil after its inventor [78] and is shown schematically in figure 16.4. The Morgan coil achieves its suppression of unwanted multipoles by symmetry in angle. Consider figure 16.5(a), four wires are wound on the surface of a cylinder and are separated azimuthally by $2\pi/4$ radians. The wires form a probe for the measurement of 4pole, 12 pole, ... 2n(2m+1) pole (m=0,1,2 ...) harmonic components. In this case for n=2 (quadrupole winding), the signal from all other multipoles is suppressed as will be shown below.

The wires are wound on the surface of the cylinder so that the signals from adjacent wires oppose. Consider again figure 16.5(a) in which the coil is located in the aperture of a quadrupole magnet. As the coil rotates, the signal from winding 1 has the opposite sign from that from winding 2. However, the two windings are connected in opposition so that the net effect is that
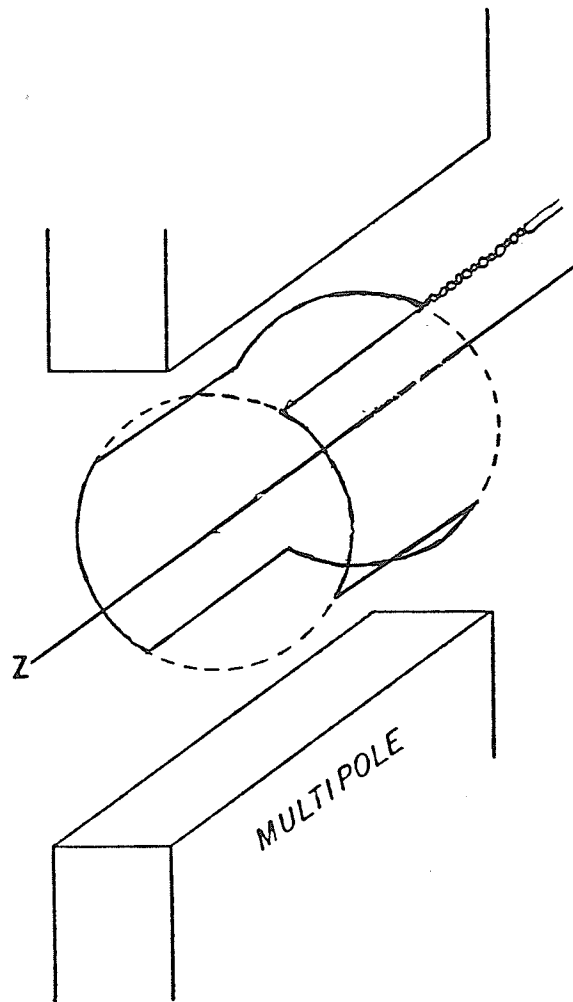
Figure 16.4 Morgan harmonic coil.

the signals from windings 1,2,3 and 4 all add.

Now consider the quadrupole measuring coil in the aperture of sextupole and octupole magnets as shown in figures 16.5(b) and 16.5(c). In figure 16.5(b) the signals from windings 1 and 3 add, as do those from 2 and 4. Because these two sets are connected in opposition, the net signal output is zero. The same is true for the sextupole case.

In this way, the Morgan coil produces an output for those multipole components which have the same symmetry as the measuring coil and suppresses many other multipole signals.

A Morgan coil wound with symmetry 2m is essentially equivalent to 2m single loops wired so that their output signals add. The voltage from such a coil will be:

$$V_{ml} = -(2m)C_n r^{n-1} Lr\omega \qquad (16.14)$$

and the coil responds to (odd multiples of 2m) field harmonics.

In practice, windings for quadrupole, sextupole and octupole symmetries are wound on the surface of a single cylinder. These additional windings allow measurement of higher order multipole contamination, which are suppressed, in the manner shown above, by the quadrupole sensitive Morgan coil. A dipole winding is also included for locating the magnetic center of the aperture.
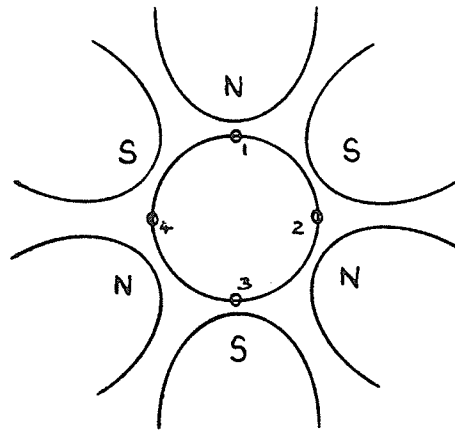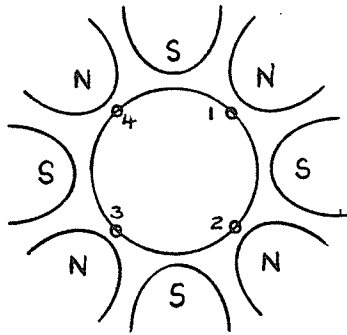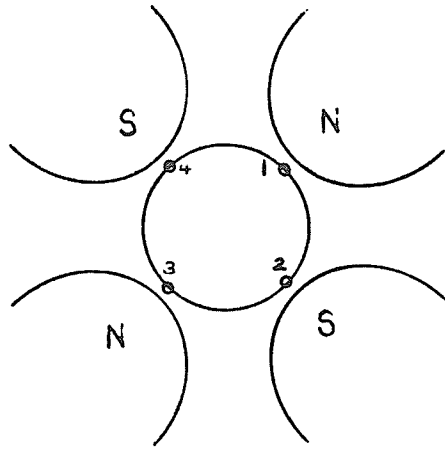
Figure 16.5 Suppression of unwanted multipoles by a Morgan coil.

215

16.4 Harmonic Probe data

The harmonic probe shown in figure 15.3 was constructed in order to measure the multipole components of one of four quadrupole magnets which formed a proton microprobe system. A winding to measure the quadrupole component and its higher orders as described above (i.e 4(2m+1) m=0,1,2...) was wound on the probe. Separate windings for octupole (8(2m+1) poles) and dipole (2(2m+1) poles) harmonics were also wound on the same cylinder. The output from each winding configuration was recorded by the field mapping system and signal averaged in software to remove the major part of the noise that was not synchronous with the output signal. The results along with a discussion of the measurements are described below.

16.4.1 Quadrupole winding

The signal output from the quadrupole winding is shown in figure 16.6. The signal amplitude recorded by the digital voltmeter is plotted against the sample number. In this case 305 readings of the probe voltage were recorded in the 4.175 seconds taken for exactly one revolution of the probe. Since the field in the aperture of the magnet is constant, further rotation of the probe through one more revolution, would produce an output signal which would be identical to that for the first. In practice, the acquired data is copied to a second array and the two arrays are catenated in software. The final array, corresponding to the quadrupole signal has four oscillations and 710 data points. The reason for doing this is that the Fast Fourier Transform routine used in the data analysis requires an even number of data points. Further the Fourier transform is performed such that the fundamental coefficient of the expansion is the coefficient of the frequency component which performs
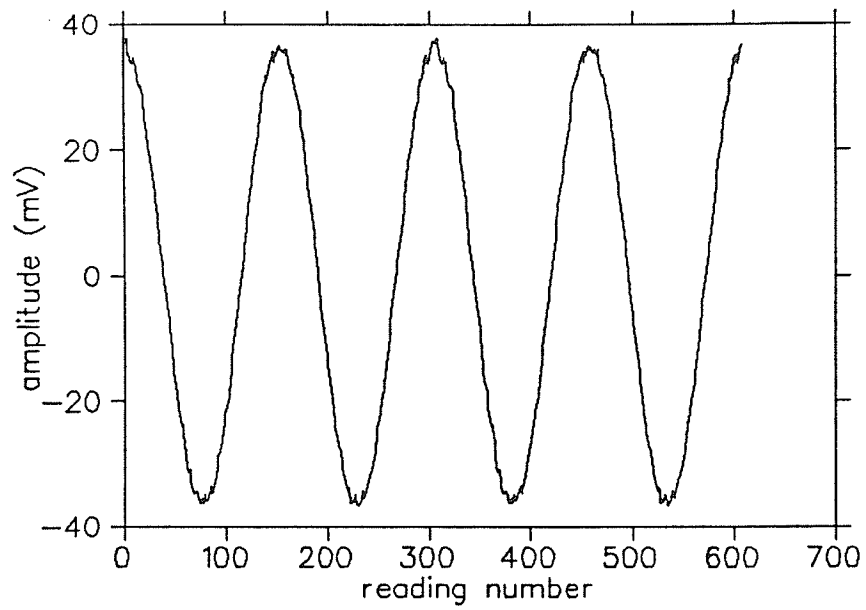
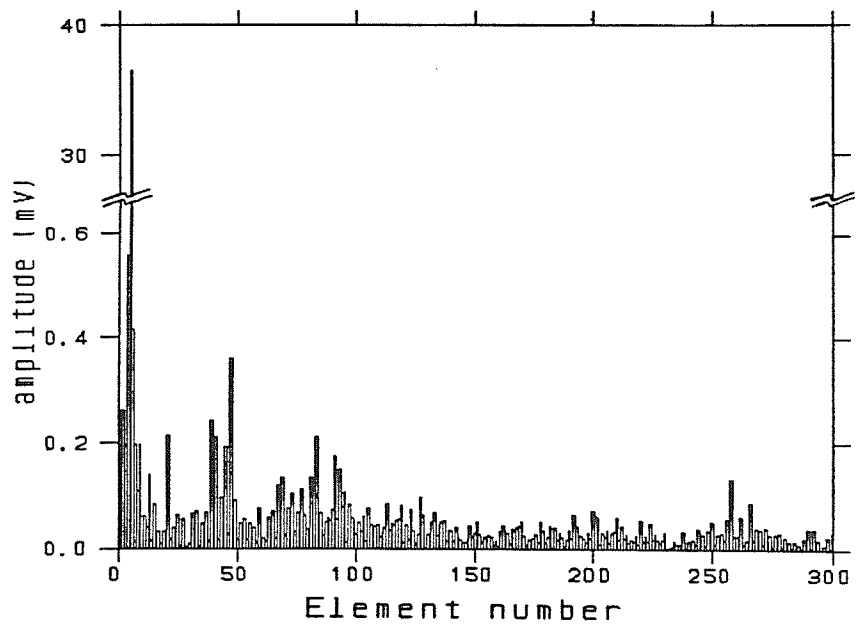Figure 16.6 Signal output from quadrupole winding.

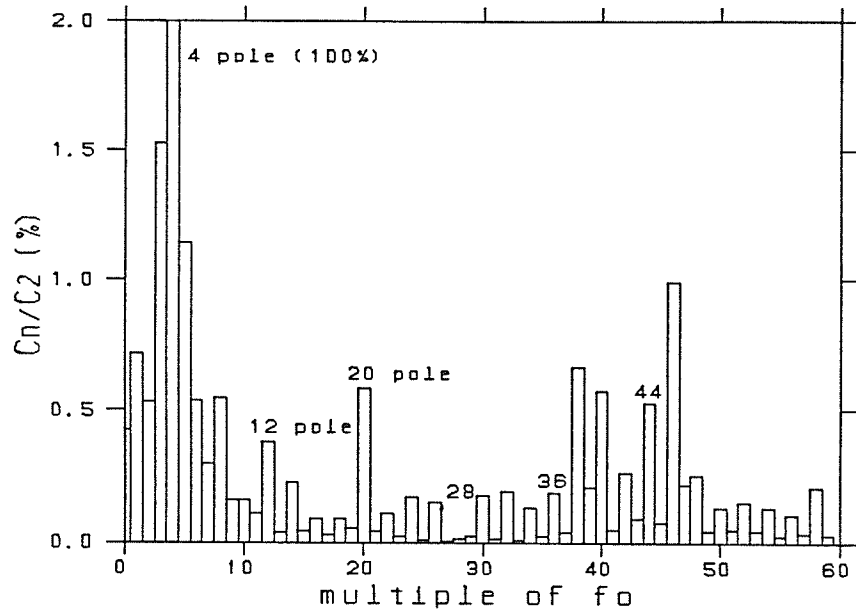Figure 16.7 Fourier transform spectrum of quadrupole winding.

217

Figure 16.8 Ratio of harmonic coefficient to quadrupole coefficient Cn/C2 for quadrupole winding.

one oscillation in the total sampled time, therefore the quadrupole (4 pole signal) of figure 16.6, which performs 4 oscillations in the sampled time, represents the fourth harmonic of the fundamental, the 12 pole harmonic represents the 12th harmonic, etc. By plotting the amplitude of coefficients of the transformed array versus the multiple of the fundamental frequency, the coefficients due to 4 pole, 12 pole, 28 pole etc. may be easily read off from the Fourier spectrum.

The Fourier transform spectrum of the signal from the quadrupole winding is shown in figure 16.7. Only the first 300 points of the transformed array are shown for clarity. The ordinate is split at 0.7 volts to show the range of the coefficients. The quadrupole harmonic appears as the fourth harmonic of the fundamental and is given by the 5th element of the transformed array. The 12 pole coefficient is given by the 13th element and so on. The abscissa may be replaced by the multiple of f_o by simply reducing the element number by 1. Usually, the harmonic coefficients are expressed as percentages of the amplitude of the fundamental component *of the magnetic field* i.e the quadrupole component. The ratios of Cn/C2 are plotted in figure 16.8 where for clarity, only contributions up to 60 pole are shown.

16.4.2 Dipole

The harmonic probe was aligned with the mechanical center of the magnet using gauge blocks to an accuracy of 0.005 inch (0.130 mm). The finite dipole signal shown in figure 16.9 shows that the magnetic and mechanical axes of the magnet do not coincide, since the output signal from the dipole winding would be zero in that case. The amplitude of the dipole signal is a measure of the separation of mechanical and magnetic centers of the magnet. It is
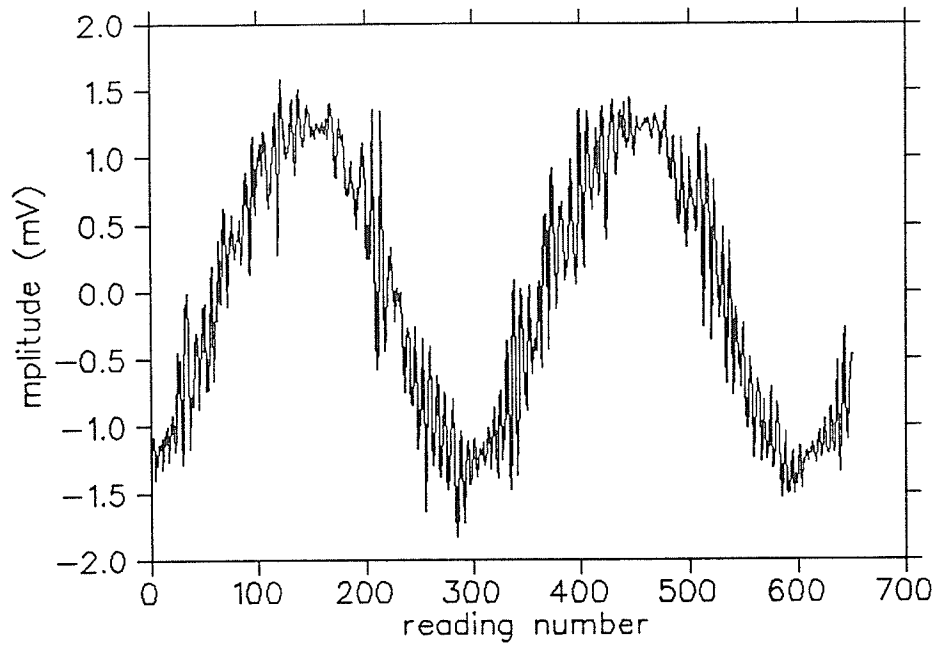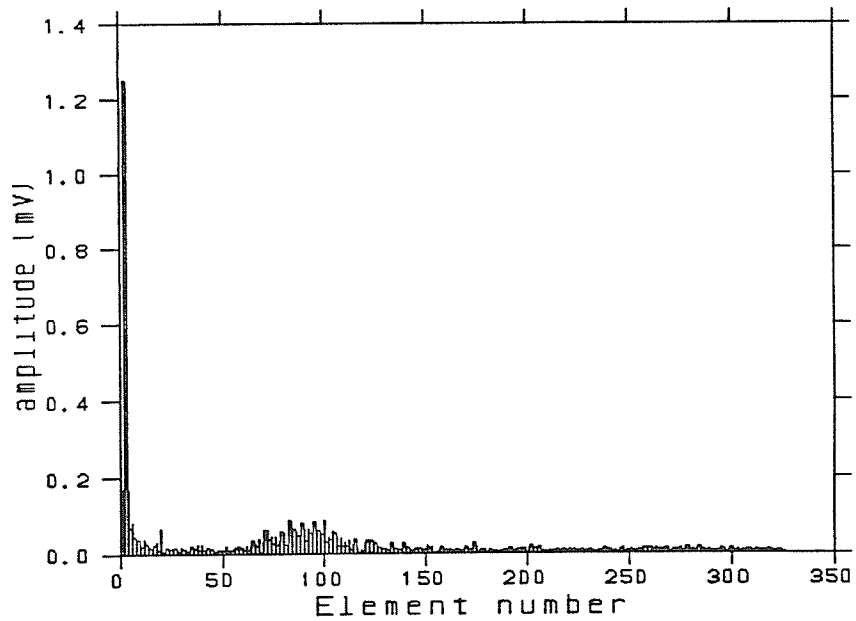
Figure 16.9 Signal output from dipole winding.

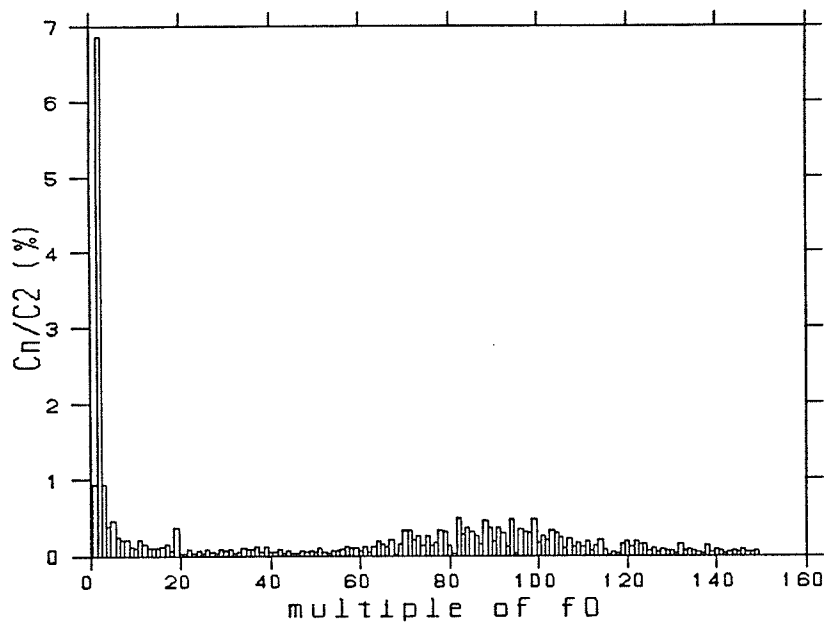Figure 16.10 Fourier transform spectrum of winding.

220

Figure 16.11 Ratio of harmonic coefficient to quadrupole coefficient Cn/C2
for dipole winding.

221

shown in appendix A that displacement of the probe from the magnetic axis does not affect the spectrum of multipoles as measured by the Morgan coil.

The signal amplitude from the dipole winding is more than an order of magnitude less than that from the quadrupole signal. The Fourier transform spectrum for this winding is shown in figure 16.10. The cluster of apparent multipoles around element number 100 will be discussed below in the section on errors.

Figure 16.11 shows the harmonic components measured by the dipole coil expressed as a function of the quadrupole harmonic C2. The dipole harmonic is approximately 7% of the quadrupole. As will be discussed below the evaluation of the higher order harmonics that the dipole winding is sensitive to is difficult since these signals are of the same order as the noise background. However, it can be seen that they all have an amplitude less than 0.5 % of the quadrupole.

16.4.3   Octupole Winding

The signal from the octupole coil is shown in figure 16.12. It can be seen that the signal has a large perturbation due to some other multipole. Fourier analysis in figure 16.13 shows the extra component to be due to $4f_o$ i.e a quadrupole harmonic, however a perfectly constructed octupole winding will have no response to a quadrupole field and therefore the winding must have a serious flaw.

If one assumes that the error in the octupole winding does not affect the 8 pole and higher coefficients then the ratio of these coefficients with respect to the quadrupole harmonic (measured by the quadrupole winding) is shown in figure 16.14.
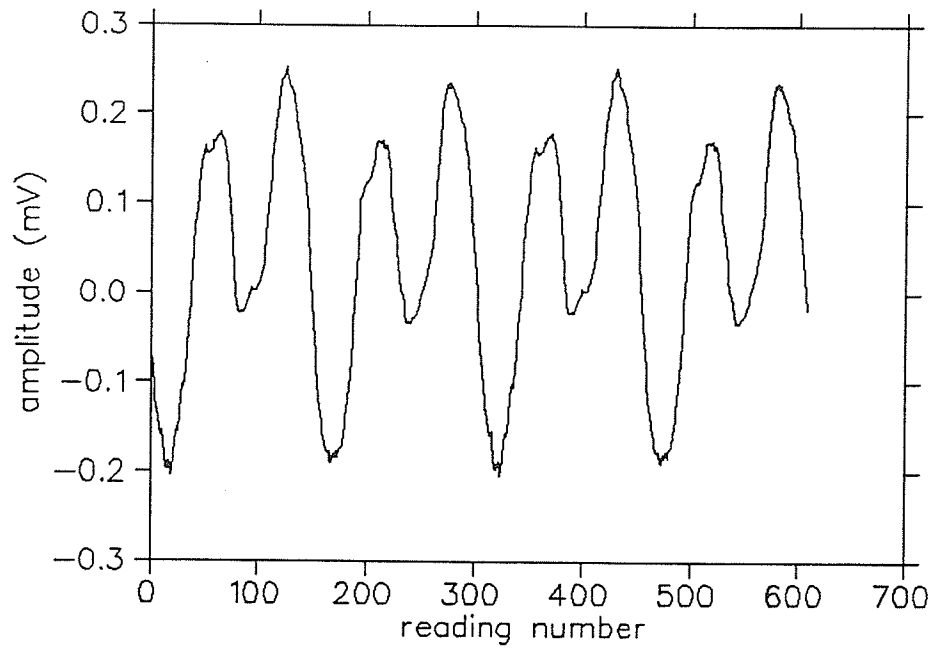
Figure 16.12 Signal output from octupole winding.
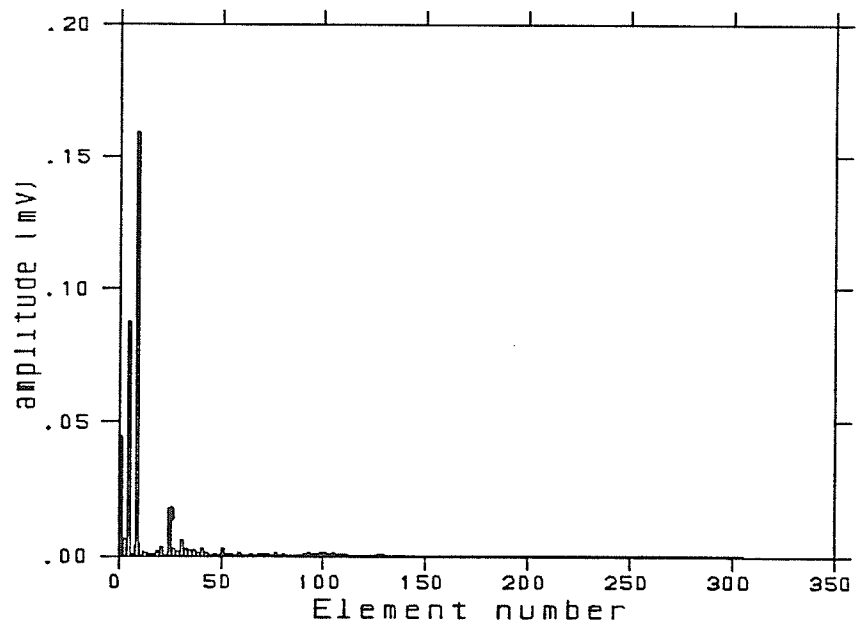
Figure 16.13 Fourier transform spectrum of winding.

223
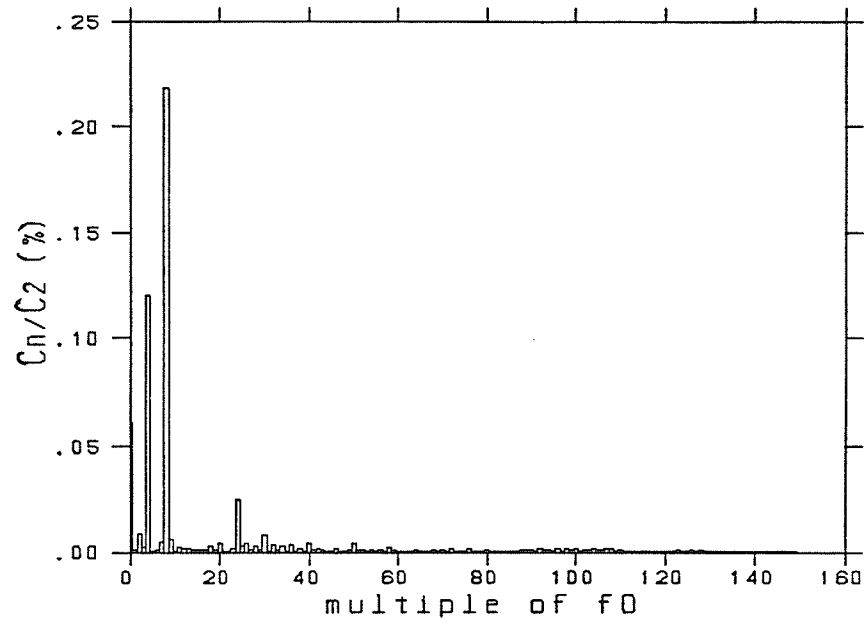
Figure 16.14 Ratio of harmonic coefficient to quadrupole coefficient Cn/C2

for octupole winding.

16.4.4 Summary

The multipoles that are of interest in determining the quality of the magnet, expressed as fractions of the quadrupole harmonic are shown in table 16.1. Where the noise has masked the actual value of the coefficient an estimate is given based on the maximum noise coefficient at that position.

n	Cn/C2 (%)
2	6.85
6	0.25
8	0.22
10	0.11
12	0.38
14	< 0.1
18	< 0.1
20	0.58
22	< 0.1
24	0.24
26	< 0.1
28	< 0.25
30	< 0.1
34	< 0.1
36	< 0.25
38	< 0.1
40	< 0.01

Table 16.1 measured multipole components of a quadrupole.

16.5 Discussion of Errors

16.5.1 Errors due to the construction of the probe

During winding of the coil it is possible to displace a wire by δr radially and $\delta\theta$ azimuthally. The result of which will be equivalent to a perfect coil plus an error loop of area:

$$\delta a = L \left(\delta r^2 + (r\delta\theta)^2 \right)^{1/2} \tag{16.15}$$

It has been shown that, if one assumes only an error in azimuth, the displacement of a conductor winding by $\delta\theta$ results in a voltage relative error given by [78]:

$$\frac{\delta\epsilon}{\epsilon} = \delta\theta \frac{C_n}{2C_N} \tag{16.16}$$

where ϵ is the signal from the coil. The angular positioning of the wires therefore limits the accuracy of the probe. In the case of the probe discussed in chapter 15, the wires are laid in a milled slot which is 0.012 inches wide (0.0030cm). If one assumes that the maximum displacement of the conductor is half the slot width the value of $\delta\theta$ is given by:

$$\delta\theta = \frac{0.012}{1.875} = 3.2 \times 10^{-3}\,\text{radian} \tag{16.17}$$

where the radius of the cylinder is 1.875 inches (4.7625 cm).

The geometry of the coil therefore limits the accuracy of the measurements of harmonic components to 1.6×10^{-3} or 0.16 % of the reading.

226

16.5.2 Errors due to method of rotation

To rotate the harmonic probe in the magnet aperture a stepping motor was used. The shaft of the motor performed one revolution for every 200 pulses received from the motor controller. The output speed from the motor was reduced 5:1 using a large gear attached to the harmonic probe. During rotation of the probe, the net action of the two brass gears caused the driving mechanism to resonate at its characteristic frequency. In an attempt to reduce this effect, the small brass gear was replaced with a nylon gear and the large brass gear damped acoustically by cementing rubber sheets to its surface. Unfortunately, this introduced a further problem: the nylon gear would tend to slip on the shaft of the stepper motor. The combination of the variation in rotation speed and the vibration of the rotating mechanism is the major cause of noise in the output signal from the Morgan coil and Fourier spectrum. The frequency distribution of the noise can be seen as the large spread out peak in figure 16.15, which is the output signal from the dipole coil with the abscissa labelled in terms of the frequency.

16.6 Conclusions

The harmonic measurement system is in need of improvement. Fortunately the technique is sound and the changes that need to be made will be easy to accomplish. A new harmonic probe should be constructed with a higher conductor placement accuracy, the basic inaccuracy stemmed from the use of milled slots along the length of the probe in which the conductors were laid. It was difficult to position the conductors along the center of the milled slot and the resulting displacement resulted in the error terms described above.
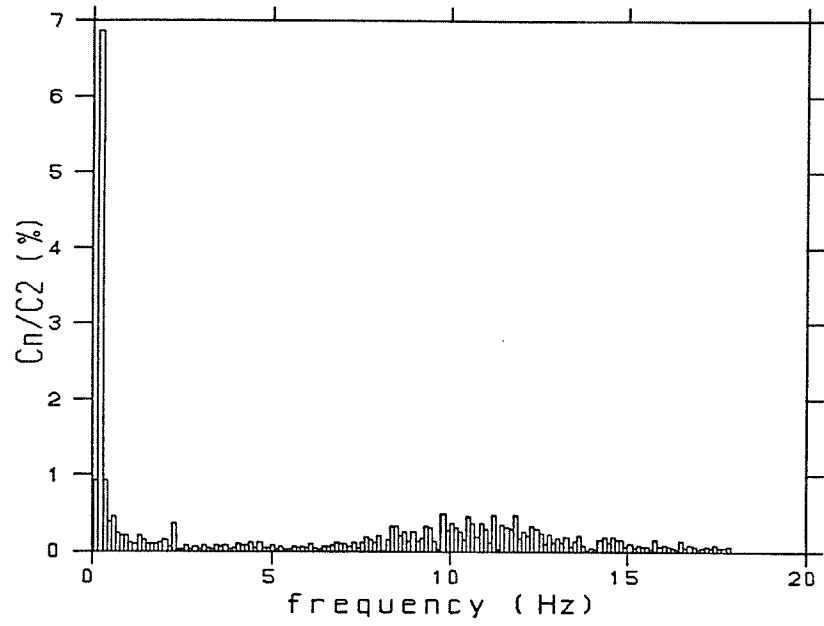
Figure 16.15 Noise spectrum due to vibration of rotation mechanism.

In the second generation design wires may be stretched along the surface of the tube with their angular location checked with some external system. When in the appropriate location they can be simply glued into place and left under tension until the adhesive has set.

The mechanism for rotating the probe in the aperture of a magnet should be re-designed. The vibration of the driving gear combined with the stepper motor drive was the major source of noise in the measurement system. By using a synchronous motor and air filled dampers to drive and support the probe, a reduction in the noise level present in the signal of at least a factor of ten can be expected. This will the allow the measurement of harmonic components which represent 1 part in 10^4 of the fundamental.

Chapter 17

Conclusions and Final Summary

A field measurement and analysis system has been designed and constructed in the Department of Physics, University of Manitoba. The system can be used to measure the representative parameters of quadrupole focussing magnets, it does so completely automatically once the magnet has been aligned in the system bed.

The unit was constructed for a fraction of the price of currently avaliable systems, while performing the same measurements with the same accuracy. This feature will make the system attractive when many magnets need to rapidly measured with high accuracy in a relatively short period of time.

The system was constructed as part of a "Technology Transfer Program" between the University and K&S Tool and Die Ltd, recently renamed "Can-Mag" a local Winnipeg Company. and is presently installed on site at the company. The system has been used to measure a series of 20 quadrupole magnets built by the company for the 50MeV proton transfer beamline of the recently commissioned HERA accelerator in Hamburg West Germany.

Chapter 18

Appendix: Effect of a misalignment of the rotating probe

In chapter 16, B was expressed in the form of a power series:

$$B = \sum_{n=1}^{\infty} iC_n r^{n-1} e^{-i(n\theta + \psi_n)} \tag{16.7}$$

$$= \sum_{n=1}^{\infty} iC_n Z^{n-1} \tag{18.1}$$

where :

$$Z = x + iy = re^{i\theta}$$

Consider a new coordinate system (x,'y') whose origin is displaced by R from the original x-y axis origin.

in the complex plane:

$$Z = Z' + R \tag{18.2}$$

where :

$$Z' = r'e^{i\theta'} \tag{18.3}$$

one may write:

$$Z^{n-1} = (Z' + R)^{n-1} = \sum_{m=0}^{n-1} \binom{n-1}{m} (Z')^{n-1-m} R^m \tag{18.4}$$

where:

$$\binom{n-1}{m} = \frac{(n-1)!}{m!(n-1-m)!} \tag{18.5}$$

substitution into (16.1) gives:

$$B = \sum_{n=1}^{\infty} iC_n \sum_{m=0}^{n-1} \binom{n-1}{m} (Z')^{n-1-m} R^m \tag{18.6}$$

The flux ϕ is calculated from:

$$\phi = \int \vec{B} \cdot \vec{n} da = Im \left(\int \sum_{n=1}^{\infty} iC_n \sum_{m=0}^{n-1} \binom{n-1}{m} (r')^{n-1-m} e^{i\theta(n-1-m)} R^m \right) Ldr' \tag{18.7}$$

and, the voltage e is given by:

$$e = -\frac{d\phi}{dt} = -\sum_{n=1}^{\infty} C_n \sum_{m=0}^{n-1} \binom{n-1}{m} r^{n-m} e^{i\theta(n-1-m)} R^m L \frac{d\theta}{dt} \tag{18.8}$$

The harmonics present in the field will be unaffected by the misalignment. For every harmonic present a second series of harmonics will be be produced.

The second series will appear an order lower than the magnetic field harmonic which produced them, e.g a quadrupole harmonic will generate a dipole term. In general these additional harmonics will be very small compared to the "real" harmonics due to the R^m term.

Bibliography

[1] R. H. Goddard. Vaporizer for use with solar energy. U.S Patent #1700675. Filed May27 1927, Patented January 29 1929.

[2] A. J. Hunt. Development of a direct absorption high temperature gas receiver. In *Proceedings of the Annual Meeting of the Solar Thermal Test Facilities Users Association.*, Houston, 1982.

[3] E. R. Hagemann. R. H. Goddard and solar power. *Solar Energy*, 6:47, 1962.

[4] T. J. Harder. *Fundamentals of Energy Production.* North-Holland Publishing Company, 1976.

[5] Nuclear power in the wake of three mile island. *IEEE Spectrum Magazine*, page 45, April 1984.

[6] G. Brown. U. S. Department of Energy support of solar research. In *Proceedings of the Annual Meeting of the Solar Thermal Test Facilities Users' Association.*, Houston, 1982.

[7] J.T. Holmes. The central receiver test facility. In *Proceedings of the Flux Measurement Workshop of the Solar Thermal Test Facilities Users' Association*, Albuquerque, 1981.

[8] J. Kleinwachter. Modular light weight solar power station. In *Solar Technology in the Eighties*, volume 4, page 3027, Brighton, 1981. International Solar Energy Society Congress.

[9] L. O. Herwig. Overview of technical and commercial solar energy developments in the united states in 1981. In *Solar Technology in the Eighties*, volume 4, page 3325, Brighton, 1981. International Solar Energy Society Congress.

[10] P.Chimelewski. General electric advanced energy programs dept. Private Communication.

[11] M. P. Thekaekara. Solar radiation measurement, techniques and instrumentation. *Solar Energy*, 18:309, 1976.

[12] M. P. Thekaekara. *Ap. Optics*, 8:1713, 1969.

[13] S. Wieder. *An Introduction to Solar Energy for Scientists and Engineers*. J. Wiley and Sons, 1982.

[14] B. Y. H. Liu and R. C. Jordan. The interrelationship and characteristic distribution of direct diffuse and total solar radiation. *Solar Energy*, 4:47, 1960.

[15] The Relation of Diffuse to total Radiation in Canada. D. W. Ruth and R. E. Chant. *Solar Energy*, 18:153, 1976.

[16] H. C. Hottel. A simple model for estimating the transmittance of direct solar radiation through clear atmospheres. *Solar Energy*, 18:129, 1976.

[17] M. Iqbal. Correlation of average diffuse and beam radiation with hours of bright sunshine. *Solar Energy*, 23:169, 1979.

[18] T. K. Van Heuklon. Estimating atmospheric ozone for solar radiation models. *Solar Energy*, 22:63, 1979.

[19] F. C. Hooper A. P. Brunger. A model for the angular distribution of sky radiance. In *Proceedings of the 18th National Heat Transfer Conference*, San Diego, 1979.

[20] H. W. Greer A. J. Drummond and J. J. Roche. The measurement of the components of solar short wave and terrestrial long wave radiation. *Solar Energy*, 9:127, 1965.

[21] T. H. Jeys and L. L. Vant-Hull. The contribution of the solar aureole to the measurements of pyrheliometers. *Solar Energy*, 18:343, 1976.

[22] R. Bahm. Satellites and forecasting of solar radiation. 1981.

[23] J. M. Kendall Sr. *Primary Absolute Cavity Radiometer*. Jet Propulsion Laboratory, 1969.

[24] E. M. Sparrow and V. K. Johnson. Experimental determination of the stefan boltzmann constant. *J. Opt. Soc. Amer.*, 53:816, 1963.

[25] C. Frolich. The third international comparison of pyrheliometers and a comparison of radiometric scales. *Solar Energy*, 14:157, 1973.

[26] I. Bennett. Monthly maps of mean daily insolation for the united states. In *Proceedings of the Solar Energy Society Conference.*, Phoenix, 1965.

[27] E. C. Boes, I. J. Halland R. R. Prairie, R. P. Stromberg, and H. E. Anderson. Distribution of direct and total solar radiation available in the u.s.a. In *Proceedings of the Joint Conference of the American Section of the International Solar Energy Society and the Solar Energy Society of Canada.*, Winnipeg, 1976.

[28] H. J. Hovel. Solar cells for terrestrial applications. *Solar Energy*, 19:605, 1977.

[29] K. Bammert. Large parabolic dish collectors with small steam or gas turbine or stirling power conversion systems. In *Solar Technology in the Eighties*, volume 4, page 2950, Brighton, 1981. International Solar Energy Society Congress.

[30] M. Hussein, P. O'Callaghan, and S. Probert. Solar activated power generator utilizing a multi vane expander as a prime mover in an organic rankine cycle. In *Solar Technology in the Eighties*, volume 4, page 3006, Brighton, 1981. International Solar Energy Society Congress.

[31] J. Zimmerman. *Sun-Pointing Programs and Their Accuracy*. Sandia Laboratories, 1981.

[32] Second generation heliostat testing and comparison. Sandia National Laboratories Internal Report, Albuquerque N.M, 1981.

[33] ECP 91A solar energy collection film. 3M technical release., St. Paul Minnesota, 1981.

[34] J. M. Kendall Sr. *Radiometer for Accurate Measurements of Solar Irradiances Equal to 10,000 Solar Constants*. Jet Propulsion Laboratory, 1981.

[35] J. M. Kendall Sr. The effective blackness of cavities. *Applied Optics*, 9:1082, 1970.

[36] M. H. Cobble. Theoretical concentrations for solar furnaces. *Solar Energy*, 5:61, 1961.

[37] O. Kamada. Theoretical concentration and attainable temperature in solar furnaces. *Solar Energy*, 9:39, 1965.

[38] R.B. Pettit. Characterization of the reflected beam profile of solar mirror materials. *Solar Energy.*, 19, 1977.

[39] B. L. Butler and R.B. Pettit. Optical evaluation techniques for reflecting solar concentrators. In *SPIE Optics Applied to Solar Energy Conversion*, volume 114, 1977.

[40] F. Biggs and C. N. Vittitoe. *Mathematical Modeling of Solar Concentrators*. Sandia National Laboratories, 1976.

[41] J. Harris and W. S. Duff. Focal plane flux distribution produced by solar concentrating reflectors. *Solar Energy*, 27:403, 1980.

[42] C. Benson. Department of Physics, University of Manitoba Summer Student Report, 1985.

[43] C. Benson. Department of Physics, University of Manitoba Summer Student Report, 1985.

[44] C. D. West. *Principles and Applications of Stirling Engines*. Van Nostrand Reinhold Company, 1986.

[45] A. H. Campbell and H. L. Teague. Advanced solar receivers - high temperature steam loop experiments. In *Solar Technology in the Eighties*, volume 4, page 2967, Brighton, 1981. International Solar Energy Society Congress.

[46] W. Last. Private communication. Dept. of Geology University of Manitoba.

[47] L. Goodfellow and T. Atwood. *Col. Sch. Mines Quart.*, 69:205, 1974.

[48] J. H. Campbell. Oil shale retorting effects of particle size and heating rate on oil evolution and interparticle oil degradation. *In Situ*, 2:1, 1978.

[49] G. P. Hinds. Effect of heating rate on the retorting of oil shale. Annual Meting of the AICHE, November 1978.

[50] H. C. Carpenter. Potential shale oil production processes. In *Proceedings of the Symposium of Oil Sand and Oil Shale Chemistry*, Montreal, 1977.

[51] A. J. Palmer and G. J. Dunning. *Study of Radiatively Sustained Cesium Plasmas for Solar Electric Conversion*. Hughes Research Laboratories, 1311 Malibu Canyon Road Malibu California, July 1980. Prepared for Ames Research Center, National Aeronautics and Space Administration.

[52] A. J. Palmer. Radiatively sustained cesium plasmas for solar electric conversion. In K. W. Billman, editor, *Progress in Astronautics and Aeronautics*, volume 61, page 201. 1980.

[53] A. J. Palmer and G. J. Dunning. Towards a high temperature solar electric converter. *J. Appl. Phys.*, 52:7086, 1981.

[54] W. Jackson. Performance of solar thermal systems with liquid metal mhd conversion. In *23rd Symposium on the Engineering Aspects of Magnetohydrodynamics*, page 587, Pittsburgh, 1985.

[55] H. Branover and Stig Claesson. Magnetohydrodynamic systems for converting solar energy into electricity. *Chemica Scripta*, 19:209, 1982.

[56] H. S. Shaw. Point focus solar concentrator. General Electric Technical Note, October 1984.

[57] J. R. Richardson. *Cyclotrons and Their Applications*. Birkhauser Verlag, 1975.

[58] E. D. Courant, M. S. Livingston, and H. S. Snyder. The strong focussing synchrotron - a new high energy accelerator. *Phys. Rev.*, 88:1190, 1952.

[59] I. S. Grant and W. R. Phillips. *Electromagnetism*. Wiley, London, 1976.

[60] E. D. Courant, M. S. Livingston, and H. S. Snyder. The strong focussing synchrotron - a new high energy accelerator. *Phys. Rev.*, 88:1190, 1952.

[61] W. C. Elmore and M. W. Garrett. Measurement of two dimensional fields - part 1 theory. *Rev. Sci. Instrum.*, 25:480, 1954.

[62] A. P. Banford. *The Transport of Charged Particle Beams*. E & F. N. Spon, 1966.

[63] H. Wiedemann. *Desy Report H5/71-4*. DESY, 1971.

[64] J. K. Cobb and J. J. Murray. Magnetic field measurement and spectroscopy in multipole fields. In *Proceedings of the first National Particle Accelerator Conference*, Washington, 1965.

[65] C. Germain. Bibliographical review of the methods of measuring magnetic fields. *Nuclear Instruments and Methods*, 21:17, 1963.

[66] A. Septier. *Focussing of Charged Particles*. Academic Press, New York, 1967.

[67] H.Weiss. *Principles and Applications of Galvanomagnetic Devices*. Pergamon Press, London, 1969.

[68] B. Turck. Measurements in an inhomogeneous field with a rectangular hall plate: Errors introduced by size effects on the perpendicular component. *Nuclear Instruments and Methods*, 95:205, 1971.

[69] J. Billan, K. N. Henrichsen, and L. Walckiers. Recent developments in magnet measuring techniques. *Atomkernenergie Kerntechnik*, 46, 1985.

[70] E. F. Bell Laboratories. *Gaussmeter Differential Probes*, 1987.

[71] P. A. Reeve. Quadrupole magnet field measuring equipment at TRI-UMF. *Nuclear Instruments and Methods*, 135:459, 1976.

[72] T. Gathright, P. A. Reeve, E. DeVita, and D. Evans. Test results on international standard quadrupole. University of Victoria Internal Report, 1986.

[73] K. L. Brown, F. Rothacker, D. C. Carey, and C. Iselin. Transport: A computer program for designing charged particle beam systems. SLAC Report SLAC-91 Rev 2 JC-28.

[74] T. R. Clune. Interfacing for data acquisition. *Byte Magazine*, Feb 1985.

[75] B. C. Brown. Fundamentals of magnetic measurements with illustrations from fermilab experience. In *Proceedings of the International Committee for Future Accelerators Workshop on Superconducting Magnets and Cryogenics*, Upton, New York, 1986.

[76] W. Lamb and R. J. Lari. Search coil measurements of the harmonic content of beam transport magnets. In *Proceedings of the first International Symposium on Magnet Technology*, Stanford, 1965.

[77] B. C. Brown et al. *Report on the Production Magnet Measurement System for the Fermilab Energy Saver Superconducting Dipoles and Quadrupoles.* Fermi National Accelerator Laboratory., 1983.

[78] G. H. Morgan. Stationary coil for measuring the harmonics in pulsed transport magnets. In *Proceedings of the Fourth International Conference on Magnet Technology*, Brookhaven, 1972.